POLITECNICO DI TORINO

Master degree course in Aerospace Engineering
Master of Science degree thesis

Two-phases turbulent channel flows

In collaboration with *Kungliga Tekniska Högskolan*

Supervisors
Prof. Michele Iovieno
Prof. Luca Brandt
Dott. Marco Edoardo Rosti

Candidate
Enrico Nicola

December 2019

En vandring på tusen mil
börjar alltid med ett steg

Acknowledgements

I am greatly indebted to my supervisor, Professor Michele Iovieno, for providing me with definite direction, professional guidance, constant encouragement from the beginning of the work and for ensuring me with moral support in many ways during the study period. I would also like to extend my deepest gratitude to Professor Luca Brandt of *Kungliga Tekniska Högskolan*, my supervisor in the host University, for his valuable suggestion and direction to accomplish my study.

Furthermore I would like to express my sincere thanks to Dr. Marco Edoardo Rosti, Post Doc Fellows at of the *KTH Mechanical Engineering Faculty*, for providing invaluable contribution and for enlightening me during the whole study period and even longer, from halfway around the world. The guidance and relentless work of his has been highly appreciable.

I am grateful to all the boys of the department for having welcomed me and having made me feel part of a big team. They are Stefano, Francesco V., Marco M., Niccoló, Dongig, Pedro, Daulet, Francesco D., Giandomenico, Luca G., Simon and many others that I can not mention for the sake of brevity. I hope they will forgive me. I would also like to acknowledge the patience of the ladies of the *KTH Exchange office* for having endured my pressing demands for so long a time. They are, in alphabetical order, Ms. Caroline Andreassen, Ms. Elisabeth Persson and Ms. Elin Wiljegård Pith.

I would like to express my sincere thanks to my colleagues at *Polytechnic of Turin* for having shared with me all the difficulties and joys that these years have brought to us. Now that I am on the top of the mountain I can look back to all those moments with a glance of pride and fulfilment, and maybe with a bit of melancholy.

At the very end, my success would not have been possible without the support of my parents. I would like to express them my sincere them my gratitude for having supported me, both pragmatically and psychologically, and for having given me the opportunity to pursue my ambitions.

Last but not least, a special thanks to all those who left, some for the better and some for the worse!

Abstract

The present document has been written throughout a period of six months that I have spent at *Kungliga Tekniska Högskolan* in Stockholm, for the Master of Science degree in Aerospace Engineering at *Politecnico di Torino*, address Aerogasdynamics.

The Scope of this work is analysing the behaviour of multiphase emulsion flows in turbulent regime within a channel. Previous studies have been carried out at the Linné Flow Centre in order evaluate the behaviour of non-brownian suspensions, deformable particles suspensions and, lately, of emulsion flows.

These results suggested that granular flows undergo three different flow regimes in the presence of a particulate phase with smooth transitions between them, commencing from a laminarlike regime, dominated by viscous forces, going through a turbulentlike regime, characterized by increased wall friction due to the turbulent transport of momentum, and ending in a third state for flows with a sufficiently high second phase percentage. In this third regime a significant increase in the wall friction is observed, due to the interaction between floating particles. This peculiar regime is called *inertial shear-thickening regime*.

In Chapter 1 and 2 the phenomena of turbulence in multiphase flows will be introduced and the analytical theory for modelling the interaction between the two phases will be exposed.
Along this study we consider emulsions of a second phase in channel flow and investigate the relation between the bubbles dynamics and the mean bulk behaviour of the mixture for Reynolds numbers $700 \leq Re \leq 2800$ and second phase volume fraction $0\% \leq \Phi \leq 25\%$, via fully resolved numerical simulations. We expect to detect a behaviour that is similar to the one observed in granular flows. The two phases have the same density, they are separated only by surface tension and the bubbles are free to merge whenever they collide. In Chapter 3 we will present the outcomes of the simulations. As forecast by previous studies for the particle suspension case, the analysis of the momentum balance reveals the existence of three different regimes: *laminar*, *turbulent* and *inertial shear-thickening* depending on which mechanism between viscosity, velocity fluctuations or bubble interaction, is the major responsible for the momentum transfer across the channel. In Chapter 4 we show that flows dominated by both Reynolds and bubble stresses tend to fall into the inertial shear-thickening regime, furthermore we describe the bulk behaviour of the mean flow at steady point. As discussed in the following, a turbulent flow is characterized by larger second fluid dispersion and a more uniform bubble distribution, whereas the bubble-dominated flows is associated with a significant bubble migration towards a circular area around the centreline. Interestingly, the mixing kernel shows similar values in the different regimes, although the relative bubble velocity and clustering clearly vary with inertia and second phase concentration.

Specific codes written in Fortran 95 have been used to compute the simulations of the multiphase flows, and the simulations have been submitted to the Scandinavian computational cluster *Beskow*.

Key words: turbulence, multi-phase flows, direct numerical simulation (DNS), bubble, droplet, surface tension, immersed boundary, interface-capturing method, emulsion flows, heat advection.

Contents

Notation

The following scheme for diagrams will be used throughout the remaining part of this document.

Colours

———	$\Phi = 5\%$
———	$\Phi = 10\%$
———	$\Phi = 15\%$
———	$\Phi = 20\%$
———	$\Phi = 25\%$

Symbols

$*$	$Re = 2800$
$\bigcirc$	$Re = 2100$
$\square$	$Re = 1400$
$\Diamond$	$Re = 700$

This pattern of colours and symbols will be used consistently in every diagram, unless indicated otherwise.

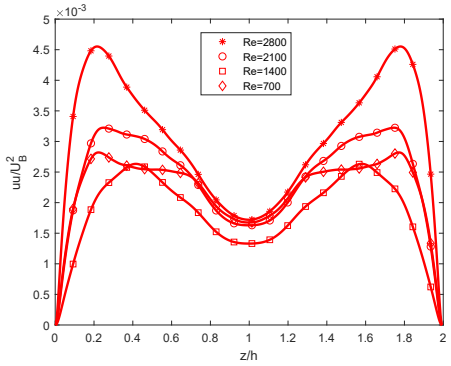

(a) $\frac{u'u'}{U_B^2}$ *in function of* $\frac{z}{h}$ *at* $\Phi = 5\%$

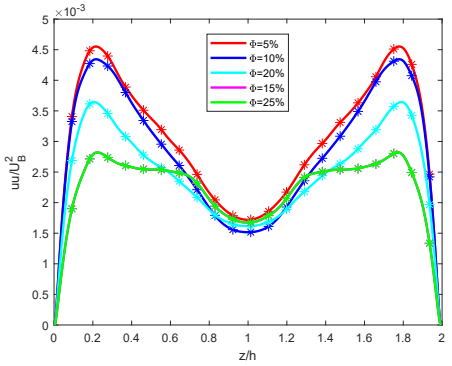

(b) $\frac{u'u'}{U_B^2}$ *in function of* $\frac{z}{h}$ *at* $Re = 2800$

For the sake of clarity an example is reported here. In the above diagrams one can observe the variation of the dimensionless profile of $u'u'$ along with the variation of Reynolds number on the left, and along with the variation of the Φ on the right. In both cases the plots report the spacial pattern of the physical quantities along the width of the channel.

Symbols

x	Span-wise coordinate
y	Stream-wise coordinate
z	Wall-normal coordinate
$\mathbf{V}$	Velocity
u	Velocity along x direction
v	Velocity along y direction
w	Velocity along z direction
u'	Turbulent velocity fluctuations along x direction
v'	Turbulent velocity fluctuations along y direction
w'	Turbulent velocity fluctuations along z direction
$\mathbf{a}$	Acceleration
t	Time
p	Pressure
e	Internal energy
E	Total energy
$\dot{\mathbf{q}}$	Heat flux
ξ	Heat production/destruction
R	Ideal gas constant
M^*	Ideal gas specific constant
M	Molar mass
μ	Dynamic viscosity
ν	Kinematic viscosity
c_p	Specific heat capacity at constant pressure
c_v	Specific heat capacity at constant volume
κ	Thermal conductivity
α	Thermal diffusivity
Γ	Diffusivity
σ	Surface tension
f_i	Surface tension force
u_τ	Shear velocity
τ_w	Wall shear stress
Φ	Second phase volume fraction
k	Curvature
σ_{ij}	Cauchy's stress tensor component

σ	Cauchy's stress tensor
R_{ij}	Reynolds stress tensor component
$\mathbf{R_{ij}}$	Reynolds stress tensor
λ	Bulk viscosity
Re	Reynolds number
Re_τ	Friction Reynolds number
Kn	Knudsen number
We	Weber number
Ca	Capillarity number
Fr	Froude number
Eo	Eos number
Mo	Morton number
Ga	Galilei number
Oh	Ohnesorge number

Note: the quantities written in bold characters represent vectorial quantities, while the ones written in normal characters represent scalar quantities.

Acronyms

RANS Reynolds Averaged Navier-Stokes Equations

LES Large Eddy Simulations

DNS Direct Numerical Simulations

TSPF Turbulent Single-Phase Flows

TDMF Turbulent Double-Phase Flows

VOF Volume Of Fluid

MTHINC Multi-dimensional Tangent of Hyperbola for INterface Capturing

FSPM Fractional Step Projection Method

ENO Essentially Non Oscillatory method

List of Figures

List of Tables

Chapter 1

Introduction

A multiphase flow can be characterized as:

> *a fluid flow consisting of more than one phase or component, ... excluded those circumstances in which the components are well mixed above the molecular level.*

according to the definition given by Christopher E. Brennen of California, professor emeritus at Institute of Technology [Chr05]. This designation still leaves space for a huge spectrum of different multiphase flows, present in many biological, geophysical and industrial environments.

Multiphase flows can be classified according to the state of the different phases, in *gas/solids* flows, or *liquid/solids* flows or *gas/particle* flows or *bubbly* flows. However only *liquid/liquid* flows with equal density of the two phases have been taken into account along the development of this study.
Biphasic liquid-liquid systems are called *emulsions*. In these flows phases are separated by a deformable interface subject to surface tension. Examples of such flows can be found in a variety of applications, ranging from advanced materials processing, waste treatment, enhanced oil recovery, food processing to pharmaceutical manufacturing. In addition to this the combination of two different phases is present in every heat exchanger, in which the heat flux causes part of the fluid to evaporate thus forming vapour bubbles dispersed in the main phase. An approach to the comprehension of turbulent multiphase flows will be presented in the last part of this work, even though this field of study is very pioneering and is yet to be fully understood.
Clearly, the ability to predict the behaviour of multiphase flows is of vital importance for optimizing those industrial processes and, despite the large number of applications in which they are involved, it is still difficult to estimate flow characteristics and the internal mechanism governing the mean bulk behaviour is still matter of discussion between scientist.

We have considered a channel in which a multiphase medium, composed by two different liquid phases with equal density, streams. Thus the separation between the two phases, which creates the bubbles dispersed along the main phase, is provided only by the surface tension. Along the superior and inferior walls *Dirichlet type* boundary conditions are imposed, see Appendix A, that guarantee that bubbles do not adhere to the wall.

Periodical boundary conditions are imposed on the streamwise outlines. However, second phase bubbles are free to merge whenever they collide. It has been observed that bubbles tend to migrate towards the centre of the channel and the three different regimes can be predicted for the flow basing on the momentum analysis: laminar, turbulent and inertial-stress regime. The transition between those regimes is appreciable with the variation of the volume fraction Φ and Reynolds number Re.
As mentioned above, in the second part of this study effects of heat conduction between channel walls and the fluid is treated.

1.1 Purposes

The purpose of this study is developing a valid theoretical model for the prediction of transition from laminarlike regime to turbulentlike regime in multiphase flow and, in addition to this, the creation of a field map in which are taken into account the three possible regimes for multiphase flows. For every couple of parameters $\Phi - Re$ shear stresses will be calculated in order to evaluate which one of the possible regimes the flow is undergoing.
Final scope of the work is to draw some detailed 3D maps in which it is clear the transition between one regime to another. In order to accomplish these results, the outcomes of the Author are compared with the existing results that can be found in the scientific literature that relates on this topic.

In the last section of the document some future developments for this field of study, in which heat conduction effects are taken into account collectively, will be shown.

At the very end of the present document some appendices are attached. In these sections some peculiar matters that deserve comprehensiveness are described with plenty of details.

1.2 Previous studies

The field of study of turbulent multiphase flows is a relatively young and unknown area, in which the presence of a second phase has to be taken into account along with the effects of turbulence, that are well described by many theoretical models for single-phase flows, even if they are not fully understood to the essence of their microstructure.

Turbulence is defined in the Enciclopædia Britannica [Enc] as a

> *state of the flow in which the fluid undergoes irregular fluctuations, or mixing, in contrast to laminar flow, in which the fluid moves in smooth paths or layers. In turbulent flow the speed of the fluid at a point is continuously undergoing changes in both magnitude and direction.*

Statistically the majority of the flows that we experiment throughout our life are turbulent: the smoke arising from a cigarette rapidly turns into a turbulent flow after a brief laminar

development, the flows across our car while we are driving along an highway is turbulent and finally most of the terrestrial atmospheric circulation can be assumed as turbulent. Hence is straightforward that the case of a flow that is both turbulent and multiphase includes a huge variety of existent flows.
Turbulence has been known and studied since the second half of nineteenth century, mainly studying natural single-phase flows at first. In fact Osborne Reynolds, while experimenting transition in channel flow, calculated already in 1883 an dimensionless parameter that could account for the balance of inertial and viscous forces, the renowned parameter known as *Reynolds number*, $Re = \frac{\rho V L}{\mu}$. For every experimental situations it is proven to exist a critical value for this number, beyond which the flow grows turbulent.

The phenomena of turbulence arises when the inertial forces in the flow grow stronger than the viscous ones that "contains" that into a well organized path of laminar streamlines, thus producing the disruption of the laminar flow into a chaotic state in which every point of the flow domain undergoes instantaneous fluctuations of velocity, in both magnitude and direction, and of the other thermodynamics characteristics, in magnitude. Nowadays there are many robust statistical theories for tackling turbulence problems, but no analytical solutions exist due to the vast amount of properties that changes simultaneously. In fact many pictoresque definitions have been given to turbulence by a number of frustrated scientist throughout the years, from Lamb's (1916) scholarly "chief outstanding difficulty of our subject" to Bradshaw's (1994) inspired "invention of the Devil on the seventh day of creation."

Turbulence in single-phase flows For what concerns single-phase flows, it is well known that transition from laminar to turbulent regime occurs when a fluid, at first flowing in parallel layers with no disruption between them, starts to present chaotic and unpredictable changes in pressure and velocity. This sudden change in the flow structure occurs when a specific parameter that indicates a non dimensional balance between inertial and viscous forces, called Reynolds number, oversteps a critical value. This signifies that inertial forces prevail over viscous forces. Many examples of turbulent flows can be observed in natural and artificial environments. In the following pictures some examples are reported.

Osborne Reynolds[1] was the first to study turbulence in single-phase flows, in works such as [Rey95]. More recently other scientist, such as Stephen B. Pope [Pop01], have studied this phenomena and made consistent advances, although an analytical solution remains unknown.

However the reasons for the breakdown of a laminar flow into turbulence has been one of the central issues in fluid mechanics for over a hundred years, for the many applications in the engineering, meteorology, oceanography and astrophysics. The theoretical work on transition is mainly based on the linear stability studies, which were firstly initiated in the nineteenth century by Helmholtz, Rayleigh and Kelvin; while the formulation for the

[1] *Osborne Reynolds* (23 August 1842 - 21 February 1912) was a prominent Irish-born British innovator in the understanding of fluid dynamics.

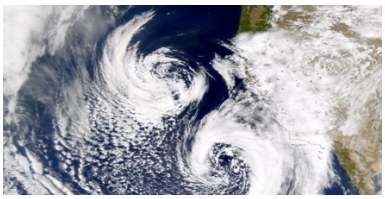

(a) *Atmospheric turbulence taken by a satellite*

(b) *Turbulence introduced by FIAT 500 model in wind tunnel*

(c) *Turbulent wake aft of a motor driven boat*

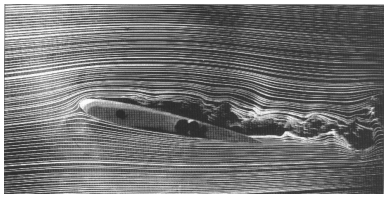

(d) *Turbulence introduced by an airfoil in wind tunnel*

Figure 1.1: Examples of single-phase turbulent flows. See [Sin].

viscous stability problem is due to Orr and Sommerfeld, who dedicated respectively to the *plane Couette flow*[2] and to the *plane Poiseuille flow*[3].

One can attribute to turbulence, under certain conditions, three important features: *isotropy*, *homogeneity* and *stationary*. *Isotropy* refers to the propriety of turbulence of having invariant statistical properties for full rotation of the reference coordinate system, *homogeneity* refers to the propriety of maintaining invariant statistical properties under arbitrary translations of the point in which they are measured. Eventually, *stationary* turbulence is the one in which the statistical properties in a certain physical point are invariant under backward or forward time shifting.

In turbulence *eddies* and *vortices* appear into the flow due to the disruption of the straight laminar streamlines into a chaotic pattern. Eddies elude precise definition, but they are conceived to be a turbulent motion, localized within a region of size e, that are at least moderately coherent over this region. On the other hand vortices are regions where the flow is spinning about an axis. In both cases there is backflow causing the fluid to rotate.
Turbulence hence appear to be made up by eddies and vortices of at different dimension

[2]The *Couette flow* is a theoretical case of study in fluid dynamics that represents the shear flow between two horizontal walls, one immobile and one moving with velocity V. The fluid, at first still, adhere to both the walls due to the viscosity and thus assumes a linear profile of velocity. It is named after the french physicist Maurice Couette.

[3]The *Poiseuille flow* is a theoretical case of study in fluid dynamics that represents the flow into a pipe with no slip condition between fluid and walls due to viscosity. Hence the velocity distribution of the flow assumes the characteristic axial-symmetric parabolic profile. It is named after the french physicist Jean Léonard Marie Poiseuille.

scale: an eddy contains a number of eddies of the smaller length scale, and so forth till the smallest length scale. The same happens for vortices.

Turbulence is characterized, as aforesaid, by sudden and unpredictable oscillations of velocity and pressure, in both direction and magnitude. It is a stochastic process and can not be treated in analytical way for it is is unpredictable in detail, but statistical properties are reproducible. Consequently a statistical approach is adopted. The first one to introduce this method was O. Reynolds with the *Reynolds decomposition*, in which every oscillating property, such as local velocity $u = \bar{U} + u'$ or local pressure $p = \bar{P} + p'$, is then divided into an average stationary component and an oscillating component.

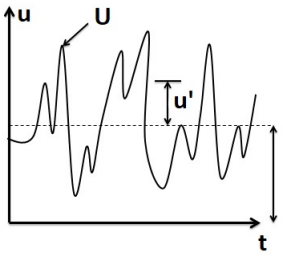

Figure 1.2: Reynolds decomposition for the velocity component u

The *Reynolds Averaged Navier-Stokes equations* directly from this statistical decomposition.

$$\begin{cases} \mathbf{v} = \mathbf{V} + \mathbf{v}' \\ p = P + p' \end{cases} \tag{1.1}$$

$$\begin{cases} \nabla \cdot \mathbf{V} = 0; \nabla \cdot \mathbf{v}' = 0 \\ \frac{\partial V_i}{\partial t} + V_j \frac{\partial V_i}{\partial x_j} = -\frac{1}{\rho}\frac{\partial P}{\partial x_i} + \nu \frac{\partial^2 V_i}{\partial x_j^2} - \frac{\partial \widehat{v_i' v_j'}}{\partial x_j} \end{cases} \tag{1.2}$$

An essential feature of turbulent flows is that they are *rotational*, namely they have non-zero *vorticity*. Vorticity is defined as the rotor of the velocity vector and its value is 0 in a perfectly laminar flow, while it assumes value different from 0 if a certain amount of turbulence arises.

$$\mathbf{\Omega} = \nabla \times \mathbf{V} \tag{1.3}$$

It is straightforward that the vorticity vector $\mathbf{\Omega} = (\omega_1, \omega_2, \omega_3)$ is always perpendicular to velocity vector $\mathbf{V} = (v_1, v_2, v_3)$ due to the rotor operation. The instantaneous velocity of an infinitesimal fluid particle appears to be the sum of the velocity of its centroid plus a rotation at velocity equal to half the vorticity, hence $\mathbf{V} = \mathbf{V_p} + \frac{\mathbf{\Omega}}{2}$.
Hence an additional equation for *vorticity* has to be written in addition to the 1.1 and 1.2, obtained by taking the curl of the Navier-Stokes equations:

$$\frac{D\omega}{Dt} = \nu \nabla^2 \omega + \omega \cdot \nabla \mathbf{V} \tag{1.4}$$

or, in expanded form:

$$\frac{\partial \omega_i}{\partial t} + v_j \frac{\omega_i}{\partial x_j} = \omega_j \frac{\partial v_i}{\partial x_j} + \nu \frac{\partial^2 \omega_i}{\partial x_j^2} \tag{1.5}$$

Some extra components of stress arises in turbulent flows, the *Reynolds stresses*, due to the averaging of the velocity components. This new component of stress is enlightened in the following writing of the second equation of 1.2:

$$\frac{\partial V_i}{\partial t} + V_j \frac{\partial V_i}{\partial x_j} = -\frac{1}{\rho}\frac{\partial P}{\partial x_i} + \underbrace{\nu \frac{\partial^2 V_i}{\partial x_j^2}}_{viscous\ stresses} - \underbrace{\frac{\partial \widehat{v_i' v_j'}}{\partial x_j}}_{Reynolds\ stresses} \tag{1.6}$$

Note that in fully developed turbulence Reynolds stresses overcome viscous stresses, while in a laminar flow they are negligible in comparison to viscous ones. To better visualize this difference in the following are represented the stress decomposition for a fully laminar and fully turbulent regime in a single-phase flow.

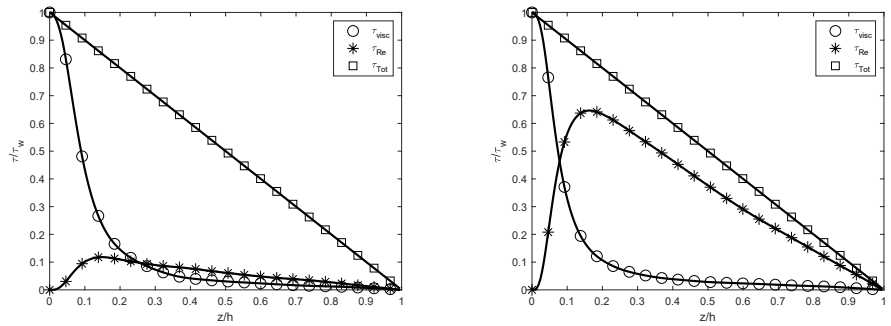

(a) *Re=700* (b) *Re=2800*

Figure 1.3: Stress decomposition in flows with different Reynolds number

From this decomposition in fact yields the *Reynolds stress tensor*:

$$\tau_{\Re} = \begin{bmatrix} \widehat{u'u'} & \widehat{v'u'} & \widehat{w'u'} \\ \widehat{u'v'} & \widehat{v'v'} & \widehat{w'v'} \\ \widehat{u'w'} & \widehat{v'w'} & \widehat{w'w'} \end{bmatrix} \tag{1.7}$$

The terms on the principal diagonal are normal stresses, while components away from the principal diagonal are shear stresses. The *Reynolds stress tensor* is obviously symmetric. In fully homogeneous turbulence only component on the principal diagonal survive,

Consider that the notation $\widehat{\cdot}$ signifies the average of the quantity underneath it.

on the other hand all the components of Reynolds stresses survive in average chaotic turbulence, thus resulting in an extra tensor term to be added to the strain tensor of the fluid.

$$\tau = \begin{bmatrix} -p & 0 & 0 \\ 0 & -p & 0 \\ 0 & 0 & -p \end{bmatrix} + \begin{bmatrix} u_{,x} & \frac{1}{2}\left(u_{,y} + v_{,x}\right) & \frac{1}{2}\left(u_{,z} + w_{,x}\right) \\ \frac{1}{2}\left(v_{,x} + u_{,y}\right) & v_{,y} & \frac{1}{2}\left(v_{,z} + w_{,y}\right) \\ \frac{1}{2}\left(w_{,x} + u_{,z}\right) & \frac{1}{2}\left(w_{,y} + v_{,z}\right) & w_{,z} \end{bmatrix} \tag{1.8}$$

It is remarkable that normal stresses in the stress tensor are produced by pressure, by viscosity and by turbulence via the Reynolds tensor; while shear stresses are produced only by viscosity and inhomogeneous turbulence.

$$\frac{\partial V_i}{\partial t} + V_j \frac{\partial V_i}{\partial x_j} = \frac{1}{\rho} \frac{\partial}{\partial x_j} \left[\underbrace{-P\delta_{ij}}_{pressure\ stresses} + \underbrace{\mu\left(\frac{\partial V_i}{\partial x_j} + \frac{\partial V_j}{\partial x_i}\right)}_{viscous\ stresses} - \underbrace{\widehat{\rho u_i' u_j'}}_{Reynolds\ stresses} \right] \tag{1.9}$$

In the code used along this study the main important sources of shear stresses are:

- **Turbulent velocity fluctuations**, cause Reynolds stresses that are computed by extracting the $v'w'$ components from the output text files for each iterations and then are time and space average thus obtaining $tau_{zy} = \bar{v'w'}$;
- **Interaction between main and dispersed phase**, in terms of pressure jump across the interface of the bubbles. These stresses are computed by subtracting τ_{Re} and tau_{bubble} form the total stresses;
- **Dissipation of momentum between adjacent flow streamlines**, due to viscous transport. These stresses are computed by linear interpolation between the shear stress at the wall, which is due to viscosity, and the centreline in which the total amount of shear stresses is equal to 0;
- **Total amount of shear stresses present in the fluid**, due to the joint action of all the above components.

One matter of fact is the evidence that turbulence dissipates energy. When turbulence arises in a flow, i.e. at high Reynolds number, a transfer of kinetic energy from the larger scales of the flow to the smaller ones takes place. This is called the *inertial cascade*, introduced by L. F. Richardson[4] in 1922. Energy is extracted from the mean flow by the large scale motions and is transmitted down via smaller and smaller scales until it is dissipated by viscous action at the smallest scales in which viscous stresses and Reynolds stresses are comparable and the Reynolds number assumes approximately unitary value. These are called *Kolmogorov scales* η, and they become smaller and smaller as Reynolds number increases. The phenomena of energy cascade is essentially inviscid and hence kinetic energy is conserved until it arrives to the smaller scales, where viscous dissipation takes place. At these scale Reynolds number $Re = \frac{\rho V l}{\mu}$, where L is the characteristic dimension of the scale, is sufficiently small that the eddy motion is stable, and molecular viscosity is effective in dissipating the kinetic energy.

length scale	$\eta = \left(\frac{\nu^3}{\varepsilon}\right)^{\frac{1}{4}}$
time scale	$\tau_\eta = \left(\frac{\nu}{\varepsilon}\right)^{\frac{1}{2}}$
velocity scale	$u_\eta = (\nu\varepsilon)^{\frac{1}{4}}$

Table 1.1: Kolmogorov microscales

where ν is the kinematic viscosity and ε is the rate of dissipation defined as:

$$\varepsilon = \nu \widehat{\frac{\partial u_i'}{\partial x_j} \frac{\partial u_i'}{\partial x_j}} \tag{1.10}$$

The theory of the inertial cascade relates on two fundamental *hypotheses* made by Kolmogorov[5] in 1941:

1. At sufficiently high Reynolds number, the small-scale turbulent motions are statistically isotropic *(local isotropy)*;
2. In every turbulent flow at sufficiently high Reynolds number, the statistics of the small scale motions have a universal form that is uniquely determined by η and ε.

The eddies in the largest size range are characterized by the lengthscale l_0 which is comparable to the flow scale $\mathcal{L}$. It is useful to introduce a lengthscale l_{EI} to represent the

[4] *Lewis Fry Richardson* (11 October 1881 - 30 September 1953) was an English mathematician, physicist, meteorologist, psychologist and pacifist who pioneered modern mathematical techniques of weather forecasting, and the application of similar techniques to studying the causes of wars and how to prevent them.

[5] *Andrey Nikolaevich Kolmogorov* (25 April 1903 - 20 October 1987) was a Soviet mathematician who made significant contributions to the mathematics of probability theory, topology, logic, turbulence, classical mechanics, algorithmic information theory and computational complexity.

demarcation between the anisotropic large eddies ($l > l_{EI}$) and the isotropic small eddies ($l < l_{EI}$).

The length-scale l_{EI} is the delimitation between the anisotropic large eddies ($l > l_{EI}$) and the isotropic small eddies ($l < l_{EI}$) in a length scale range called *universal equilibrium range*. The universal equilibrium range is split into two subranges: the *inertial subrange* ($l_{EI} > l > l_{DI}$) and the dissipation range ($l < l_{DI}$). Motions in the inertial subrange are determined by inertial effects, viscous effects being negligible.
The suffixes EI and DI indicate that EI is the demarcation line between energy (E) and inertial (I) ranges, as DI is that between the dissipation (D) and inertial (I) subranges.

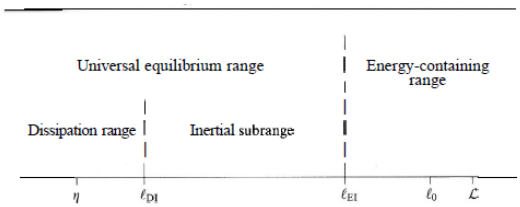

Figure 1.4: Partition of turbulent scales into subranges

Many different techniques have been used to extrapolate a model capable of predicting the behaviour of turbulent flows via both experimental and computational tools. For what concerns the first branch the main instrument is the hot-wire anemometer, an apparatus that can be immersed into the flow at very close distance from the wall and can detect instantaneous variation in velocity magnitude and directions with a very high frequency, even into the viscous sub-layer. Obviously this instrument must be employed along with a wind tunnel facility and an adequate electronic transducer that can collect data an huge amount of data at high frequency. It is not unusual that data from an hot wire anemometry have size of TB!
On the other hand, for what concerns the computational approach, one can computing analytically the full velocity field solving the Navier-Stokes equations, compute the average field of velocity and then then apply statistical averages to the oscillations or solve only the larger scales of turbulence and then apply theoretical methods to describe the smaller ones. The first approach is the Direct Numerical Simulation and is very demanding in terms of computational resources and time, hence is applied only to elementary cases for scientific research sake; the second one is the solution of the aforementioned RANS and finally the third approach is called LES, Large Eddy Simulation.

Turbulence in multi-phase flows Turbulence in two-phase flow has been a subject of interest for many years. However, only low concentration suspensions are relatively well understood; in such flows, the turbulence of the mainstream is not affected by the dispersed phase. Those cases when the turbulence in the surrounding fluid is affected are much more difficult. For the remainder of this document we will refer to turbulent double-phase flows with the acronym TDMF.

Multi-phase flows are involved in a number of industrial application and studying their behaviour is very important for optimizing those factory processes. They can be classified into *segregated flows* and *dispersed flows* depending on whether both fluids are more or less contiguous throughout the domain or one of the fluids is dispersed as non-contiguous involved: liquid-gas flows are observed in heat exchangers or in cavitation of marine propellers, while liquid-liquid flows, better said *emulsions*, are exploited for chemical production, mixing and reaction of immiscible liquids.

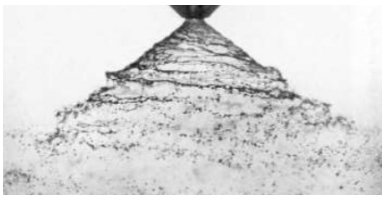

(a) *The injections of fuel in combustion chamber in a car engine*

(b) *Sedimentation flow after a flood*

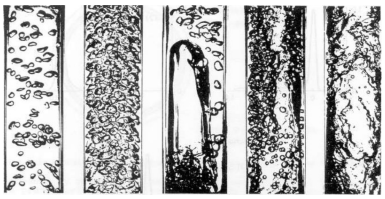

(c) *Various bubble regimes in heat exchanger pipes*

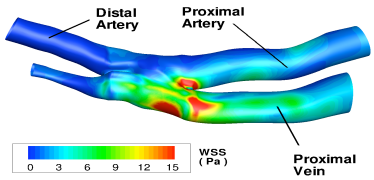

(d) *Computer simulation of pressure distribution in an arterial bifurcation*

Figure 1.5: Examples of multi-phase turbulent flows. See [Sta].

In emulsion flows the two phases are both liquid, hence they are separated by a deformable interface subject to inter-facial surface tension. Given the number of applications in which these flows are involved it is often desirable to predict or manipulate the rheology of emulsions, even though there has been limited progress toward the creation of theoretical models that can reliably predict the rheology and micro-structure of such flows. Direct numerical simulations (DNS) of TDMF are far more challenging than DNS of turbulent single-phase flows (TSPF), since TDMF possess, in general, a much wider spectrum of important length scales and time-scales than that of TSPF.
Experimental data show that turbulence can be attenuated or augmented depending on the size of the particles with respect to the length scale of the turbulence. In general *three sources affecting turbulence energy*, K, in a single phase flow have been identified:

diffusion D_K, production P_K and dissipation ε, see [Cro93].

$$\frac{\partial K}{\partial t} = D_K + P_K - \varepsilon \tag{1.11}$$

The first one relies on the gradient of turbulent energy and it is proven to be null in homogeneous turbulence; the second one is attributed to the work done by shear in a velocity gradient and third one accounts of the effect of dissipation rate, which is the results of viscous effects.
As aforesaid in 1.10, dissipation rate ε is produced by the turbulent velocity fluctuations. The effect of a dispersed phase is usually included by subtracting another term, ε_d, defined as the dissipation rate due to the dispersed phase.

Many models have been proposed in order to give a proper description of the second phase dissipation rate throughout the years, since the very rudimentary models that dealt only with the turbulence energy, or turbulence intensity to the more accurate direct numerical simulations of turbulent fields with particles and discrete vortex methods with particles and droplets. All these models rely on the $K - \varepsilon$ model, that prescribes two additional equations for turbulent kinetic energy and dissipation rate and was firstly introduced by Launder and Spalding in 1972.

Experimental data collected by Hetsroni and Sokolov [HS71] found that the presence of particles decreased the turbulence level in a jet in comparison with the single-phase case. In 1989 the work of Gore and Crowe [GC89] highlighted that the diameter of the dispersed phase particles or bubbles affects the level of turbulence in a channel flow: smaller particles or bubbles tend to decrease the level of turbulence, while larger ones tend to increase the level of turbulence. Small particles can move with the turbulent eddies so the energy required to maintain particle motion comes at the expense of the turbulent energy in the fluid. On the other hand, the large particles are less responsive to the fluid motion but generate wakes which represent a source of turbulence energy. The transition occurs at a particle/length scale ratio of approximately 0.1.

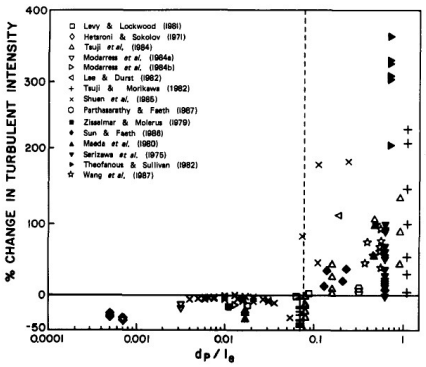

Figure 1.6: Effects of dispersed phase on the mean flow turbulence in function of the ratio between particle diameter and the integral scale of turbulence.(See [GC89])

No significant effects of particles in pipe flows on the energy spectrum for large values of $\frac{D}{\Lambda}$ appear to be significant. However Tsuji and Morikawa, [TMS84] and [TM82], found

that for small values of $\frac{D}{\Lambda}$ that the power spectrum was reduced at lower frequencies but increased at higher frequencies. For particle-laden boundary layers, Kulic [Kul93] found that particles tend to reduce the power spectrum at the low frequencies and increase it at the high frequencies. Hence it appear straightforward that the influence of the second phase on the energy spectrum depends strictly on the size of particles or bubbles.
Hetsroni and Rashidi [RHB90] noted that small particles attenuate turbulence but larger particles with Reynolds numbers exceeding 400 will enhance turbulence due to vortex shedding. His results were not conclusive and he suggested the need for more data. Further data by Yokuda and Crowe [YC91] on the self-generated turbulence in a liquid-solid flow corroborated the importance of Reynolds number.

From the outcomes of Crowe [Cro93] it appears that there are at least five sources of modification in the turbulence structure of multi-phase flows compared to single-phase flows:

1. *Velocity disturbances created by displacement of flow around a particle or droplet*, in laminar flow around a particle, the streamlines are displaced and the fluctuation in velocity due to streamline displacement can be regarded as "turbulence";

2. *Modification of energy production rate in carrier phase*, the presence of the particles can alter the velocity gradients of the carrier phase and change the energy production rate giving rise to augmentation of turbulence energy;

3. *Viscous dissipation due to the presence of dispersed phase*, most models predict that viscous dissipation attenuates turbulence energy, even if Elghobashi and Truesdell's [ET93] work suggests that there are cases where this term is negative which would result in an increase in turbulence;

4. *Wake-generated turbulence*, the wakes of particles or droplets could contribute to the turbulence energy but this mechanism is not possible for particles smaller than the Komolgorov length scale;

5. *Particle-particle interaction*, as the number density of a particulate flow is increased, the motion of the particles induced by collisions will provide a source of turbulence energy. Of course, the energy used for work on the particles comes from the carrier flow so the net effect on turbulence energy is neat.

There are several dimensionless parameter that describe this phenomena. The Reynolds number computed on the shear layer is called *Shear Reynolds number* and is defined as:

$$Re_Z = \frac{SL_Z^2}{\nu} \tag{1.12}$$

An additional parameter that we ought to define is the *Weber number* [6], used as a measure of the relative importance of the fluid's inertia compared to its surface tension:

[6] *Moritz Weber* (18 July 1871 - 10 June 1951) was a German engineer.

$$We_{S_0} = \frac{\rho S^2 D_0^3}{f_i} \tag{1.13}$$

$$We_{rms_0} = \frac{2\rho K D_0}{f_i} \tag{1.14}$$

Both the Weber numbers 1.13 and 1.14 are of interest since they are based on two different mechanisms that may affect the droplets dynamics: on large scales (large droplets) the effect of the mean shear is dominant (1.13), while on small scales (small droplets) the flow is mainly dominated by the isotropic turbulent fluctuations (1.14).

Eventually there is the *Capillary number*:

$$Ca = \frac{\mu V}{f_i} \tag{1.15}$$

that accounts for the relative effect of viscous drag forces versus surface tension forces acting across the interface between the two phases.
Note that the Weber number can be rewritten as:

$$We = \frac{\rho V^2 l}{f_i} = \frac{\mu V}{f_i} \cdot \frac{\rho V l}{\mu} = Ca \cdot Re \tag{1.16}$$

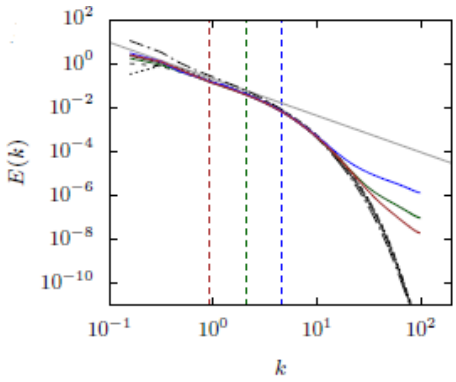

Figure 1.7: Energy spectrum for multiphase flows. The black and green lines represent the single and multiphase flows, while other three colored solid lines (blue, green and brown) are used for the spectra of the two-phase flows with $We_0 = 0.5, 4, 10$. The grey line is $\propto k^{-5/3}$. (See [Ros+19])

The presence of the droplets modifies the flow profoundly. The averaged spectrum of the turbulent kinetic energy in both phases in the two-phase case is reported in Figure 1.7, where we observe that the interface mostly affects the large wave numbers (small scales) for which higher levels of energy are evident, while slightly lower energy is present at the large scales.

The increased energy at high wave numbers has been explained by the breakup of large eddies due to the presence of the suspended phase and the consequent creation of

new eddies of smaller scale. In the same figure we can also observe that the effect of the droplets decreases as the Weber number increases; in other words, the spectra of the multiphase cases approach the single phase one as *We* increases [Ros+19].

The size of the bubbles decreases with the increase of the Weber number. Although using Weber number 1.13 or 1.14 is inappropriate given that the droplets can break up or coalesce, this measure may not be fully representative of the state of the multiphase problem. It is preferable to use a Weber number based on a flow length scale We_λ.

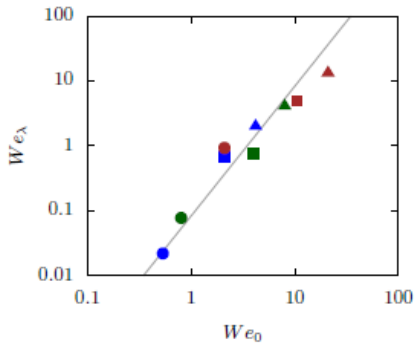

Figure 1.8: Relation between We_λ and We_0 ($We_\lambda \propto We_0^2$). (See [Ros+19])

This effect can be evaluated in the results obtained by Rosti M. and Ge J. using a computational mesh of $1312 \times 640 \times 624$ grid points and imposing $Re = 15200$, see [Ros+19].

Different techniques have been proposed to numerically tackle the problem at hand. The so-called front tracking method is an Eulerian/Lagrangian method, used to simulate viscous, incompressible, immiscible two-fluid systems, first developed by Unverdi and Tryggvason [UT92] and Tryggvason et al. [Try+01]. When dealing with moving and deformable boundaries, an alternative approach are the so-called front-capturing methods, which are fully Eulerian and handle topology changes automatically. A strong advantage of these methods is that they are easier to parallelize than their Lagrangian counterpart. Eulerian interface representations include essentially the volume of fluid (VOF in short) [Sus+07] and level-set (LS in short) [SS03], [SSO94] methods.

As will be discussed diffusely in section 2.5, the presence of the two phases originates another type of shear stress forces, apart from the viscous shear stresses and the Reynolds stresses due to turbulent velocity fluctuations.

This third component originates from the surface tension at the interfaces between the two phases at the bubble boundaries, which acts as a constraint for the dispersed phase within the shape of the bubble dispersed along the main phase flow. This causes a discontinuity in the pressure at the interface of the two phases, that is evaluable as the force per unit surface due to the *surface tension*.

In the MTHINC method the following boundary conditions are implemented in order to couple the two phases:

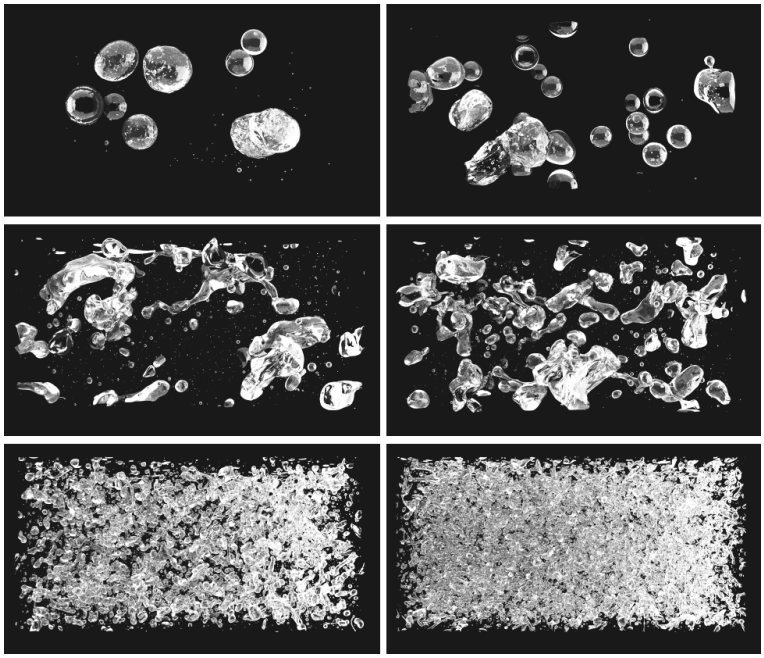

Figure 1.9: Visualization of multiphase flow at different We_λ value. We_λ:(top left) $We_\lambda = 0.02$, (top right) $We_\lambda = 0.08$, (middle left) $We_\lambda = 0.8$, (middle right) $We_\lambda = 0.4$, (bottom left) $We_\lambda = 0.5$ and (bottom right) $We_\lambda = 13$. In the figures the flow is from left to right. (See [Ros+19])

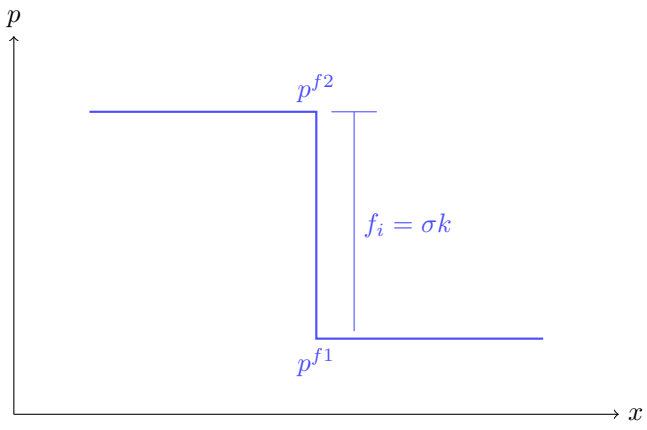

Figure 1.10: Pressure discontinuity across the interface between the two phases.

$$\begin{cases} u_i^{f1} = u_i^{f2} \\ \sigma_{ij}^{f1} n_j = \sigma_{ij}^{f2} n_j + \sigma k n_i \end{cases} \tag{1.17}$$

where u_i represents every component of the *velocity* vector, and the written σ_{ij} represents every component of the *shear stress tensor*. Hence the formulas in 1.17 express a vectorial identity.

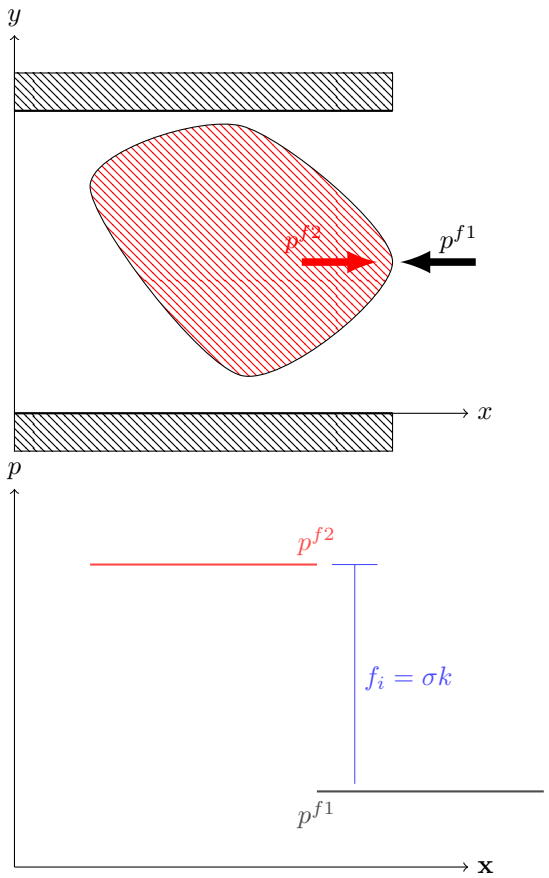

Figure 1.11: Pressure discontinuity across the interface between the two phases.

For further studies on decomposing of shear stresses in multi-phase emulsion flows see [Ros+18], [RDVB19]. On the contrary for what concerns liquid-solid interaction, present in flows such as sedimentation and turbidity currents, see [RB18], [Las+16], [Las+14] and [Pic+13].

1.3 Numerical methods for multiphase flows

Over the last few years, numerical simulation has become an essential tool for the investigation of multiphase flow. In a limited number of cases, computation can solve actual practical problems which lend themselves to direct numerical simulation, but, more frequently, computation is the only available tool to investigate crucial physical aspects of the situation of interest, for example the role of gravity, or, as will be presented in this

study, surface tension, which can be set to arbitrary values unattainable with physical experimentation.

Direct numerical simulation (*DNS* in short) have been used to numerically solve the Navier-Stokes equations since their very humble beginning, when Orszag and Patterson computed a low Reynolds number turbulent flows on a staggered 32^3 grid back in 1971. That results, which nowadays appears laughable, was the very beginning of turbulent DNS.

Nevertheless performing direct numerical simulation is not always feasible because the computational effort would be too demanding for complex geometries, in fact As a result, most engineering problems, e.g. the flow around a car, have too wide a range of scales to be directly computed using DNS. Hence for engineering applications simpler models are used: the resolution of a statistical averaged form of the Navier-Stokes equations, named *Reynolds Averaged Navier-Stokes Equations*, (*RANS* in short), or a intermediate complexity model called *Large Eddy Simulations*, (*LES* in short) in which the largest scales are fully solved while the smaller ones are modelled using statistical tools.

The range of scales that need to be accurately represented in a computation is dictated by the physics of the problem. The grid determines the scales that are represented, while the accuracy with which these scales are represented is determined by the numerical method. For what concerns time discretization, in incompressible DNS is common to use implicit time advancement for the viscous terms and explicit time advancement for convection terms.

In fact, in turbulent flows, very large time steps adopted by implicit methods were found to cause the turbulence in the channel to decay to a laminar state. At time steps small enough for time accuracy to be maintained, the overhead associated with the implicit algorithm made it uncompetitive with explicit time advancement for the convection terms.

For what concerns boundary conditions, these are usually imposed with periodic conditions in channel flows or similar geometries, in which statistics are homogeneous in the stream-wise direction. In this case boundary conditions are used in the stream-wise direction while generating a statistically stationary turbulent flow whose statistics corresponded to a single experimental stream-wise station. Unfortunately this is not the case of the majority of flows. DNS of more complex flows must specify turbulent inflow and outflow boundary conditions. The earliest methods for specification of inflow turbulence essentially generates a three-dimensional, divergence-free field of random fluctuations that was homogeneous in the stream-wise direction and had second order statistics prescribed by the model.

Compressibility introduces additional boundary-condition issues. Characteristic analysis must be used in compressible DNS to determine the number of boundary conditions required. Typically, formulations used in Aeroacoustics are used by current compressible DNS.

Chapter 2

Governing equations for multiphase flows

In the first section of this Chapter the most general governing equations for fluids will be treated then, in the second part, the governing equations for the peculiar case of multiphase flows will be derived. But first some fundamentals aspects of Computational Fluid Dynamics are to be introduced.

2.1 Fundamental aspects

Computational Fluid Dynamics relates on how to numerically solve the conservation laws that describes the behaviour of the fluid, when an analytical solution is either not feasible or too demanding in terms of computational resources, so as to have an *approximate solution* that contains a certain *numerical error*.

Fluid The first and more common concept one has to face when approaching fluid-dynamics is the concept of *fluid*. *Encylopædia Britannica*, see [EB69] and [Enc], defines a *fluid* as

> *liquid or gas or generally any material that cannot sustain a tangential, or shearing, force when at rest and that undergoes a continuous change in shape when subjected to such a stress.*

From the common sense it is known that a fluid is, in general, a substance that has no own geometry and that can assume any shape. Fluid can be classified into *liquids*, *vapours* or *gases*. The first ones have a defined volume, while the latter two have no defined volume and the difference between them depends on whether or not they are above the critical temperature: gases are above T_{cr} and can not be liquefied via compression, vapours are below T_{cr}.

Control volume Starting from this sentence the concept of *control volume* can be better defined as a volume of fluid in which properties are evaluated and on whose surfaces can be defined fluxes of the aforesaid properties.
The control volume can be *finite* or *infinitesimal*. In the first case conservations laws shall be written in *integral form*,while in the latter they shall be written in *differential form*.

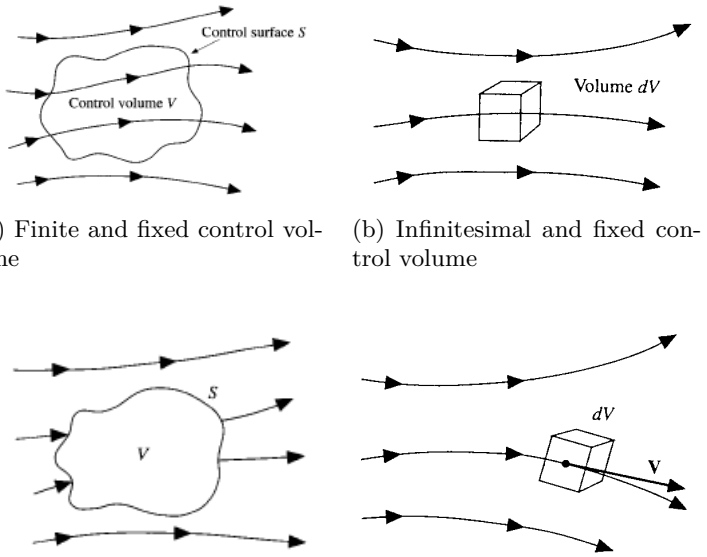

(a) Finite and fixed control volume

(b) Infinitesimal and fixed control volume

(c) Finite and moving control volume

(d) Infinitesimal and moving control volume

Figure 2.1: Various type of control volume

In the first case conservation laws contain integrals, while in the second the contain only derivatives. The integral form is more general since it allows the presence of discontinuities such as shock wave within the control volume, while discontinuities cannot be treated with the differential form.

Conservation form Another concept on which it is desirable to reflect is the difference between *conservative* and *non conservative* form. The first one provides terms cancellation for the derivatives when they are discretized, hence only values at the boundaries are counted. On the contrary, with non-conservative form, every time a new grid point is added, new terms of the Taylor's series are added and the number of terms in the sum grows. In other words, what comes in does not balance what goes out, so it is called *non-conservative*.
If the solution is expected to be smooth, for instance for shock-free flows,then non-conservative may work; while is the solution is expected to have shocks, or chemical reactions, or any other sharp interfaces, then the conservative form is preferable.

Fluid particle A fluid particle is the smallest control volume in which statistical values for the thermodynamics properties can be defined. At the same time it is so small that it can be considered as a point with respect to the entire fluid domain. This peculiar aspect can be expressed via the Knudsen number $Kn = \frac{l_{mfp}}{L}$, where l_{mfp} is the geometric mean free path between the molecules, depending only on thermodynamics parameters (for instance for air it is $l_{mfp} \simeq 6.35 \cdot 10^{-10}$) and L is the characteristic dimension of the domain. If $Kn \ll 1$ the fluid can be considered as a continuum and fluid particles approximation can be used.

Numerical grid Computational domain has to be discretized in points. Numerical values for the fluid properties are assigned to every discrete point of the grid. Grids can be *structured* or *unstructured* depending on whether or not cell boundaries are orthogonal with each other.

Discretization method A method of approximating the differential or integro-differential equations in the system of algebraic equations for the variables at some set of discrete locations in space and in time. Most used discretization methods are *finite differences*, *finite volumes* and *finite elements*.

2.2 Conservation laws

Conservation laws represents three elementary principles of physics applied to fluids: mass is conserved (incompressible flows), momentum is conserved and energy is conserved. In general conservation laws can be written in the following integral form:

$$\int_{V(t_2)} \Psi dV - \int_{V(t_1)} \Psi dV + \int_{t_1}^{t_2} \oint_{S(t)} \mathbf{n} \cdot \mathbf{F} dS dt = \int_{t_1}^{t_2} \int_{V(t)} P dV dt \tag{2.1}$$

where Ψ is a vector containing the variables that are conserved, $\mathbf{F}$ is a vector containing the fluxes of the variables through the surface $S(t)$ and P represents the rate of production of Ψ per unit volume per unit time. Hence the former two term to the left hand side represents the variation of the variables along with time, the third term accounts for the convective transport for the variables due to the fluxes, while the term to the right hand side represents the production of variables due, for example, to the presence of sources/wells.
If all the variables are continuous in time, then 2.1 can be rewritten as:

$$\frac{\partial}{\partial t} \int_{V(t)} \Psi dV + \oint_{S(t)} \mathbf{n} \cdot \mathbf{F} dS = \int_{V(t)} P dV \tag{2.2}$$

See [LPZ13] and [JA95] for further details.
Applying the Gauss's theorem to the 2.2 it is possible to write it in the divergence or differential form, suitable for infinitesimal control volume:

$$\frac{\partial \Psi}{\partial t} + \nabla \cdot \mathbf{F} = P \tag{2.3}$$

2.3 Navier-Stokes equations

The governing equations of fluid were firstly derived by Leonhard Euler[1] in the 18th century to describe the flow of incompressible and frictionless fluids, thus obtaining the Euler equations for an incompressible and non viscous fluid. In 1821 Claude Louis Marie Henri Navier[2] accounted for the effect of viscosity in order to describe a more realistic model for fluids. Throughout the middle of the 18^{th} century, Sir George Gabriel Stokes [3] worked on the papers of his forerunner, improving his work, and obtained the final form of the Navier-Stokes equations, a set of partial differential equations whose analytical solution is still unknown nowadays.

Navier-Stokes equations represent the analytical form of three physical principles applied to fluids: conservations of the mass, conservation of the momentum and conservation of energy.

Navier-Stokes equations represents the Taylor series expansion of the Burnett equations, truncated to the first order.

Order	Equations
0	Euler equations
I	Navier-Stokes equations
II	Burnett equations

Table 2.1: Taylor series expansions for Burnett equations

2.3.1 Conservation of mass

The first Navier-Stokes equation accounts for the fact that, given an incompressible flow,

> *the total mass of any isolated material system is neither increased nor diminished by reactions between the parts*

Let's consider an infinitesimal volume of fluid:

where the three component of the velocity vector are represented: u along x direction, v along y direction and w along z direction.

[1] *Leonhard Euler* (15 April 1707 - 18 September 1783), was a Swiss mathematician, physicist and astronomer, who made outstanding contribution to mathematics of his time.

[2] *Claude Louis Marie Henri Navier* (10 February 1785 - 21 August 1836), was a French engineer and physicist who specialized in structural mechanics, being renamed for his theorem of elasticity. He is now considered the founder of structural mechanics.

[3] *Sir George Gabriel Stokes*, 1st Baronet (13 August 1819 - 1 February 1903), was an Anglo-Irish physicist and mathematician, best known for his works on fluid dynamics and the theorem of algebra which is named after him, the *Stokes theorem*.

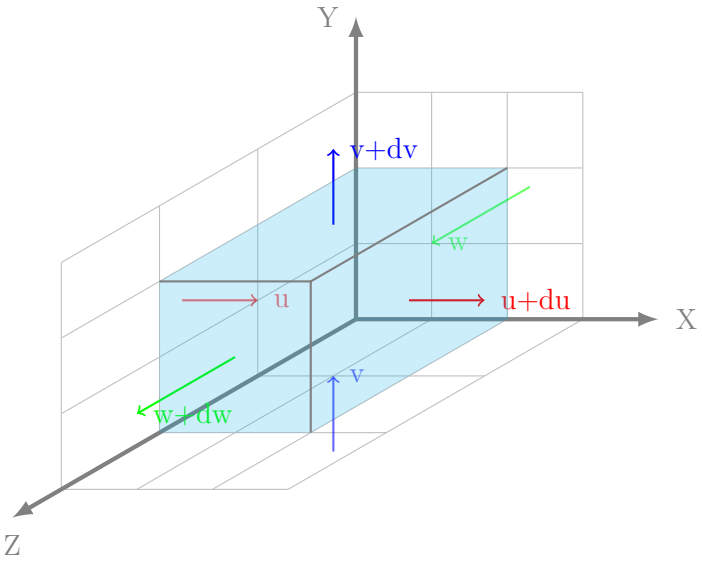

Figure 2.2: Infinitesimal control volume with reference coordinate system

Mass conservation	
Integral conservative form	$\frac{\partial}{\partial t}\int_V \rho dt + \int_S \rho \mathbf{V}\cdot\mathbf{n}dS = 0$
Integral non conservative form	$\frac{D}{Dt}\int_{V(t)} \rho dt = 0$
Differential conservative form	$\frac{\partial \rho}{\partial t} + \nabla\cdot(\rho\mathbf{V}) = 0$
Differential non conservative form	$\frac{D\rho}{Dt} + \rho\nabla\cdot\mathbf{V} = 0$

Table 2.2: Equation of mass conservation

2.3.2 Conservation of momentum

Second principle of dynamics, stated by Isaac Newton [4] in 1687, affirms that

> *the change of motion is proportional to the impressed force, and is in the direction of the right line in which that force is impressed*

[4] *Sir Isaac Newton* (Woolsthorpe-by-Colsterworth, 25 December 1642 - London, 20 March 1727), was an English physicist and mathematician, whose work *PhilosophiæNaturalis Principia Mathematica*, in which he first stated the three principles of dynamics, has represented a milestone in the comprehension of the nature that surrounds us.

$$\mathbf{F} = \frac{m\partial \mathbf{V}}{\partial t} \tag{2.4}$$

where the quantity $m\mathbf{V}$ is called *momentum*.

This principle is directly applicable to fluids, that cannot stand shear solicitations but can be considered as a body, having mass and hence inertia. Fluid are subjected to two different kind of forces, *body forces* and *volume forces*. The first ones have to be in contact with the body on which they act in order to have effect, and they are hydrodynamic pressure, tangential shear stresses and normal stresses. On the contrary the second ones do not need the physical contact to act, for instance electromagnetic force or inertia are body forces. Let's consider the same fluid particle of Figure 2.3, but this time body and volume forces are represented as well, together with surface forces per unit surface.

Body forces per unit volume	$f_x dxdydz$
Surface shear stresses per unit surface	$\tau_{ij} didk$
Hydrostatic pressure per unit surface	$pdndm$

Note that for sake of simplicity, only quantities along x-direction are represented. One could apply the same reasoning to the other directions.

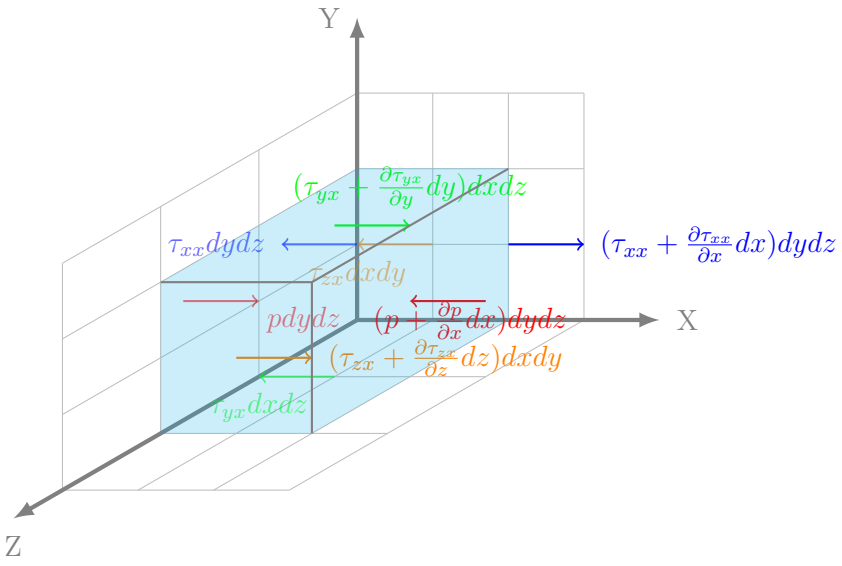

Figure 2.3: Infinitesimal control volume with reference coordinate system

Applying the II principle of dynamics to the fluid volume it yields:

Note that, unlike mass conservation and energy conservation equations, the momentum conservation equation is a *vectorial* equation, meaning that it must be written along every direction x, y and z. Equation for momentum conservation in integral non conservative form is written in compact vectorial notation.

Momentum conservation	
Integral conservative form	$\begin{cases} \frac{\partial}{\partial t}\int_V \rho u dV + \int_S \rho u \mathbf{V}\cdot\mathbf{n}dS + \int_S p n_x dS = \int_S \tau_{\mathbf{x}}\cdot\mathbf{n}dS + \int_V \rho f_x dV \\ \frac{\partial}{\partial t}\int_V \rho v dV + \int_S \rho v \mathbf{V}\cdot\mathbf{n}dS + \int_S p n_y dS = \int_S \tau_{\mathbf{y}}\cdot\mathbf{n}dS + \int_V \rho f_y dV \\ \frac{\partial}{\partial t}\int_V \rho w dV + \int_S \rho w \mathbf{V}\cdot\mathbf{n}dS + \int_S p n_z dS = \int_S \tau_{\mathbf{z}}\cdot\mathbf{n}dS + \int_V \rho f_z dV \end{cases}$
Integral non conservative form	$\frac{\partial}{\partial t}\int_V \rho\mathbf{V}dV + \int_S \rho\mathbf{v}\mathbf{v}\cdot\mathbf{n}dS + \int_S p\mathbf{I}\cdot\mathbf{n}dS - \int_S \tau\cdot\mathbf{n}dS = \int_V \rho\mathbf{f}dV$
Differential conservative form	$\begin{cases} \frac{\partial \rho u}{\partial t} + \nabla\cdot(\rho u\mathbf{V}) = -\frac{\partial p}{\partial x} + \frac{\partial \tau_{xx}}{\partial x} + \frac{\tau yx}{\partial y} + \frac{\partial \tau_{zx}}{\partial z} + \rho f_x \\ \frac{\partial \rho v}{\partial t} + \nabla\cdot(\rho v\mathbf{V}) = -\frac{\partial p}{\partial y} + \frac{\partial \tau_{xy}}{\partial x} + \frac{\tau yy}{\partial y} + \frac{\partial \tau_{zy}}{\partial z} + \rho f_y \\ \frac{\partial \rho w}{\partial t} + \nabla\cdot(\rho w\mathbf{V}) = -\frac{\partial p}{\partial z} + \frac{\partial \tau_{xz}}{\partial x} + \frac{\tau yz}{\partial y} + \frac{\partial \tau_{zz}}{\partial z} + \rho f_z \end{cases}$
Differential non conservative form	$\begin{cases} \rho\frac{Du}{Dt} = -\frac{\partial p}{\partial x} + \frac{\partial \tau_{xx}}{\partial x} + \frac{\tau yx}{\partial y} + \frac{\partial \tau_{zx}}{\partial z} + \rho f_x \\ \rho\frac{Dv}{Dt} = -\frac{\partial p}{\partial y} + \frac{\partial \tau_{xy}}{\partial x} + \frac{\tau yy}{\partial y} + \frac{\partial \tau_{zy}}{\partial z} + \rho f_y \\ \rho\frac{Dw}{Dt} = -\frac{\partial p}{\partial z} + \frac{\partial \tau_{xz}}{\partial x} + \frac{\tau yz}{\partial y} + \frac{\partial \tau_{zz}}{\partial z} + \rho f_z \end{cases}$

Table 2.3: Equation of momentum conservation

2.3.3 Conservation of energy

The third one of Navier-Stokes equations, even if the first two are generally considered to be the proper Navier-Stokes equations, accounts for the balance between work and heat fluxes supplied to the control volume and the variation of the energy contained in it along time.

The principle of conservation of energy, also known as the first principle of thermodynamics, states that

> *the change in internal energy of a system is equal to the heat added to the system minus the work done by the system*

$$\Delta E = Q - W \tag{2.5}$$

This principle was first written by Clausius[5] and Rankine[6] around 1850.

In order to give a proper description of work and heat transition to and from the control volume, the following sources of work and heat fluxes are considered:

[5] *Rudolf Julius Emanuel Clausius* (2 January 1822 - 24 August 1888) was a German physicist and mathematician and is considered one of the central founders of the science of thermodynamics.

[6] Prof. *William John Macquorn Rankine* (5 July 1820 - 24 December 1872) was a Scottish mechanical engineer who also contributed to physics and mathematics. He was a founding contributor, with Rudolf Clausius to the science of thermodynamics, particularly focusing on the first of the three thermodynamic laws. He is also known for the Rankine scale for temperature measurement.

Mechanical work	
Work done per unit time on the control volume by volumetric forces	$\rho \mathbf{f} \cdot \mathbf{V} dxdydz$
Work done per unit time on the control volume by surface forces	$\tau_{ij} didk$
Conduction and heat production	
Heat flux per unit surface	$\dot{q}_i djdk$
Volumetric heating per unit volume	$\rho\dot{\xi} dxdydz$

Fourier's law The heat flux due to thermal conduction depends from the temperature gradients through the Fourier's law:

$$\dot{\mathbf{q}} = -k\nabla T \tag{2.6}$$

where k is the thermal conductivity of the material and ∇T is the temperature gradient. Note that equation 2.6 is a vectorial equation and it is written here in compact form.

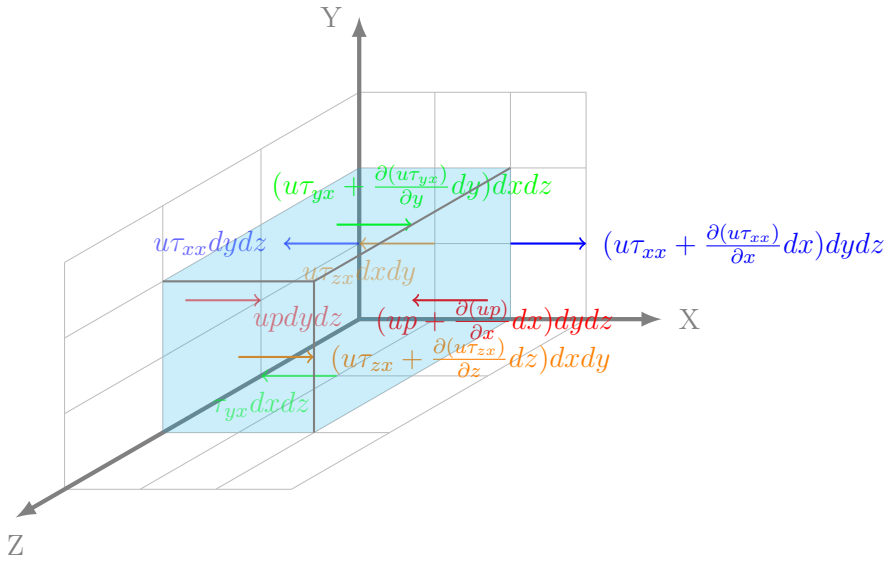

Figure 2.4: Infinitesimal control volume with reference coordinate system

As the previous case, again for the sake of simplicity, only quantities along x direction

are drawn in the graphs, even though the equation of energy conservation is a scalar equation and accounts for the quantities along every direction.

Hence, total variation of energy per unit volume with respect to time can be linked the fluxes of heat through the volume's surfaces, inner heat sources, and work don by external body and volume forces with the following equations:

Energy conservation	
Integral conservative form	$\int_V \frac{\partial E}{\partial t} dV + \int_V \nabla \cdot (E\mathbf{V}) dV = \int_V \rho\dot{\xi} dV - \int_V \nabla \cdot \dot{\mathbf{q}} dV - \int_V \nabla \cdot (p\mathbf{V}) dV + \int_V \nabla \cdot (\tau \cdot \mathbf{V}) dV \int_V + \rho\mathbf{f} \cdot \mathbf{V} dV$
Integral non conservative form	$\int_V \frac{\partial E}{\partial t} dV + \int_V \nabla \cdot [(E+p)\mathbf{V}]\, dV - \int_V \nabla \cdot (\tau \cdot \mathbf{V}) dV + \int_V \nabla \cdot \dot{q} = \int_V \rho\dot{\xi} dV + \int_V \rho\mathbf{f} \cdot \mathbf{V} dV$
Differential conservative form	$\frac{\partial E}{\partial t} + \nabla \cdot (E\mathbf{V}) = \rho\dot{\xi} - \nabla \cdot \dot{\mathbf{q}} - \nabla \cdot (p\mathbf{V}) + \nabla \cdot (\tau \cdot \mathbf{V}) + \rho\mathbf{f} \cdot \mathbf{V}$
Differential non conservative form	$\rho \frac{D}{Dt} \left(e + \frac{1}{2} \mid \mathbf{V} \mid^2 \right) = \rho\dot{\xi} - \nabla \cdot \dot{\mathbf{q}} - \nabla \cdot (p\mathbf{V}) + \nabla \cdot (\tau \cdot \mathbf{V}) + \rho\mathbf{f} \cdot \mathbf{V}$

Table 2.4: Equation of energy conservation

Note that all the equations of table 2.4 are written in compact form, where the quantities written in bold characters are vectors.

2.4 Enclosure of the algebraic system

Seven Navier-Stokes equations have been written so far: 1 for mass conservation, 3 for momentum conservation along the directions of the physical space, and 1 for energy conservation. They form a non-linear system of partial differential equations with 7 unknowns: u, v, w, p, ρ, T, and e. It is straightforward that the system is not closed, since it has just 5 equations of 7 unknowns. Hence two additional equation have to be found in order to provide a closed system: they are the *ideal gas law* and the *constitutive equation* for an ideal gas.

2.4.1 Ideal gas law

This equations, first stated by Clapeyron[7] in 1834, correlates all the thermodynamic quantities p, ρ and T by mean of a universal constant, the ideal gas constant R.

$$p = \rho \frac{R}{M} T = \rho R^* T \tag{2.7}$$

where the ideal gas constant R is equal to $8.314472 \, \frac{\mathrm{J}}{\mathrm{molK}}$.

2.4.2 Constitutive equation for an ideal gas

It is possible to write an equation that correlate the inner energy of a fluid with its temperature by mean of a constant. The constant is the constant volume specific heat capacity c_v.

$$e = c_v T \tag{2.8}$$

The 2.8 states a proportional relationship between the inner energy of a body and its temperature measured in Kelvin degrees.

One can obtain now the closure of the algebraic system putting together the equations in tables 2.2, 2.3 and 2.4 with the constitutive laws 2.7 and 2.8.
Even thought the system of partial differential equations is now fully determined, having 7 unknowns for 7 equations, it is still non-linear and an analytical solution to it is still to be found. Hence the are discretized and numerical tools are used in order to solve this set of equations.

2.5 Navier-Stokes equations for multiphase flows

It has been considered the flow of two incompressible viscous fluids, separated by an interface, in a channel with immobile walls, i.e. a plane Poiseuille[8] flow. Note that he following notation has been taken from the article *Numerical simulations of emulsions in shear flows*, of the authors M. E. Rosti e F. De Vita ([RDVB19]). Figure 2.15 shows a sketch of the geometry and the Cartesian coordinate system, where x, y, and z denote the wall-normal, streamwise, and spanwise coordinates, while u, v, and w denote the corresponding components of the velocity vector field. The lower and upper impermeable walls are located at $y = -h$ and $y = h$ respectively.

[7] *Benoît Paul Émile Clapeyron* (26 January 1799 - 28 January 1864) was a French engineer and physicist, one of the founders of thermodynamics. He is best known for having summed up together Boyle's law, Charles's law, Avogadro's law and Gay-Lussac's law in the ideal gas law.

[8] *Jean Léonard Marie Poiseuille* (22 April 1797 - 26 December 1869) was a French physicist and physiologist.

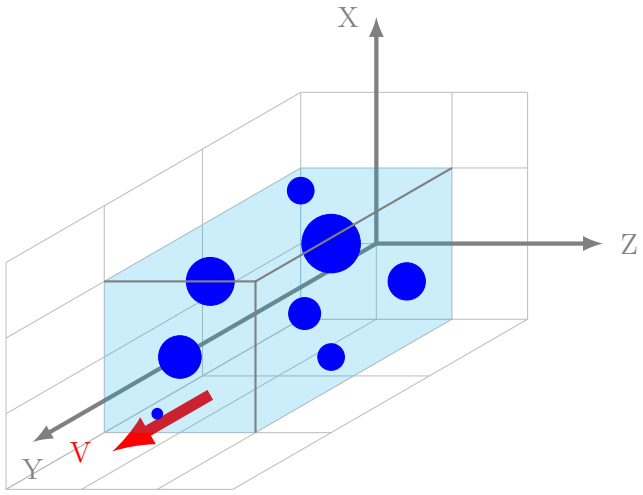

Figure 2.5: Infinitesimal control volume with reference coordinate system

The two-fluid motion is governed by the conservation of momentum and the incompressibility constraint, and the kinematic and dynamic interactions between the two fluid phases are determined by enforcing the continuity of the velocity and traction force at the interface between the two phases.

$$\begin{cases} u_i^{f1} = u_i^{f2} \\ \sigma_{ij}^{f1} n_j = \sigma_{ij}^{f2} n_j + \sigma k n_i \end{cases} \tag{2.9}$$

where notation $f1$ and $f2$ refers to the most abundant phase, the *main phase*, and to the less abundant phase, the *dispersed phase*, respectively. Vectors n_i and n_j refers to the *normal* to surfaces, k is the *curvature* of the interface surface and σ is the *surface tension*.

On the contrary u_i represents every component of the *velocity* vector, and the written σ_{ij} represents every component of the *shear stress tensor*. Hence the formulas in 2.22 express a vectorial identity.

The terms σ_{ij} are the components of the *Cauchy's stress tensor*[9], defined as follows:

$$\sigma = \begin{bmatrix} \sigma_{xx} & \sigma_{yx} & \sigma_{zx} \\ \sigma_{xy} & \sigma_{yy} & \sigma_{zy} \\ \sigma_{xz} & \sigma_{yz} & \sigma_{zz} \end{bmatrix} \tag{2.10}$$

in which every component of the stress tensor is defined as:

[9]Baron *Augustin-Louis Cauchy* (21 August 1789 - 23 May 1857) was a French mathematician, engineer and physicist who made pioneering contributions to continuum mechanics. He is best known for his theorems in the field of elasticity.

$$\sigma_{ij} = \underbrace{-p\delta_{ij}}_{\text{hydrostatic pressure}} + \underbrace{\delta_{ij}\lambda(\nabla \cdot \mathbf{V})}_{\text{bulk stress}} + \underbrace{\mu\left(\frac{\partial u_i}{\partial x_j} + \frac{\partial u_j}{\partial x_i}\right)}_{\text{shear stresses}} \tag{2.11}$$

The first term on the right hand side of 2.11 accounts for the hydrodynamic static pressure, in fact it occurs only for terms on the main diagonal, second term accounts for the resistance made by the fluid when some external factor tries to expand or compress it. This is called *bulk viscosity*, represented as λ. This contribute will not be considered from now on since the two fluids are non compressible. Finally there is the the contribution of shear stresses due to the fact that the two considered fluids are viscous.

Given the particular case that is being examined, we necessitate to account separately for the contribution of the two fluids as follows:

$$\sigma_{ij} = (1 - \Phi)\sigma_{ij}^{f1} + \Phi\sigma_{ij}^{f2} \tag{2.12}$$

For what concerns parameter μ and ρ, which are essential for calculating the stress tensor, they are calculated using the *lever rule*:

$$\begin{cases} \rho = (1 - \Phi)\rho^{f1} + \Phi\rho^{f2} \\ \mu = (1 - \Phi)\mu^{f1} + \Phi\mu^{f2} \end{cases} \tag{2.13}$$

To numerically solve the two-phase interaction problem at hand, it has been used the volume of fluid method. We introduce an indicator function H to identify each fluid phase so that $H = 1$ in the region occupied by the fluid $f1$ and $H = 0$ otherwise. Considering that the fluid is transported by the flow velocity, we update H in the Eulerian framework by the following advection equation written in divergence form:

$$\frac{\partial \Phi}{\partial t} + H\frac{\partial u_i}{\partial x_i} = \Phi\frac{\partial u_i}{\partial x_i} \tag{2.14}$$

where Φ is the cell-averaged value of the indicator function.
Once Φ is known, the two-fluid equations can be rewritten in the so-called one-continuum formulation, see [TSH07] for references, so that only one set of equations is solved over the whole domain. This is achieved by introducing a monolithic velocity vector field u_i, defined everywhere and found by applying the volume averaging procedure. Thus, u_i is governed by the following set of equations:

$$\begin{cases} \frac{\partial u_i}{\partial t} + \frac{\partial u_i u_j}{\partial x_j} = \frac{1}{\rho}\left(\frac{\partial \sigma_{ij}}{\partial x_j} + f_i\right) \\ \frac{\partial u_i}{\partial x_i} = 0 \end{cases} \tag{2.15}$$

where f_i is the surface tension force define as $f_i = \sigma k n_i \delta$.
The first one of equations 2.15 refers to momentum conservation, while the second one accounts for mass conservation.

2.5.1 The MTHINC method

The indicator function H can be reconstructed in various ways; here, we use the multi-dimensional tangent of hyperbola for interface capturing ($MTHINC$) method, developed by Ii et al. [Ii+12], where a multi-dimensional hyperbolic tangent function is used as an approximated indicator function. In particular, the indicator function H is approximated as

$$H(\bar{x},\bar{y},\bar{z}) \simeq \hat{H}(\bar{x},\bar{y},\bar{z}) = \frac{1}{2}\left(1+\tanh\left((\beta(H(x,y,z)+d)\right)\right) \tag{2.16}$$

where $(\bar{x},\bar{y},\bar{z}) \in [0,1]$ is a centred local coordinate system defined in each cell, P is a three-dimensional surface function, β a sharpness parameter, and d a normalization parameter. The function P can for instance a linear function (a plane):

$$P(\bar{x},\bar{y},\bar{z}) = a_{100}\bar{x} + a_{010}\bar{y} + a_{001}\bar{z} \tag{2.17}$$

The constants a_{1mn} are calculated algebraically by imposing the correct value of the three normal components n_i and the six components of the *cartesian curvature tensor* $l_{ij} = \left(\frac{\partial n_i}{\partial x_j} + \frac{\partial n_j}{\partial x_i}\right)/2$ for the function P in each cell. Finally, the parameter d is found by enforcing the following constraint:

$$\int_0^1\int_0^1\int_0^1 \hat{H}d\bar{x}d\bar{y}d\bar{z} = \Phi \tag{2.18}$$

The integration can be performed analytically in one direction, and numerically in the other two directions by the two-point Gaussian quadrature.
The unit normal vector is defined as $n_i = \frac{m_i}{|\nabla\Phi|}$, being m_i the gradient of the volume of fluid function, i.e. $m_i = \frac{\partial\Phi}{\partial x_i}$. Once the normal vector is known, the curvature k can be easily found by taking the divergence of the normal vector, i.e. $k = \frac{\partial n_i}{\partial x_i}$, and the surface tension force f_i can be computed by the *continuum surface force*, see [BKZ92] for references. In this model 1D approximate delta function δ is directly approximated by $\delta \simeq |\nabla\Phi|$. It yields:

$$f_i = \sigma k n_i \delta \simeq \sigma k \frac{\partial\Phi}{\partial x_i} \tag{2.19}$$

2.5.2 Numerical solution

The equations of motion are solved with an in-house code, written in FORTRAN 95, on a staggered uniform grid with velocities located on the cell faces and all the other variables (pressure, stress, and volume of fluid) at the cell centres. All the spatial derivatives are approximated with *second-order centred finite differences*, while the time integration is discussed hereafter.
First, the volume of fluid function is updated in time from the time step (n) to (n + 1) by solving equation 2.14, following the procedure proposed by Ii et al. [Ii+12]. In particular, the time evolution of Φ is calculated by evaluating the numerical fluxes sequentially in

each direction, a robust and easy approach called directional splitting. Thus, 2.14 is discretized sequentially in the three Cartesian direction:

$$\begin{aligned}
\Phi_{*}^{ijk} &= \Phi_n - \frac{1}{\Delta x}\left(f_{(n)}^{i+\frac{1}{2},j,k} - f_{(n)}^{i-\frac{1}{2},j,k}\right) + \frac{\Delta t}{\Delta x}\Phi_{n+1}^{i,j,k}\left(u^{i+\frac{1}{2},j,k} - u^{i-\frac{1}{2},j,k}\right) \\
\Phi_{**}^{ijk} &= \Phi_{*} - \frac{1}{\Delta x}\left(g_{*}^{i+\frac{1}{2},j,k} - g_{*}^{i-\frac{1}{2},j,k}\right) + \frac{\Delta t}{\Delta x}\Phi_{**}^{i,j,k}\left(v^{i+\frac{1}{2},j,k} - v^{i-\frac{1}{2},j,k}\right) \\
\Phi_{***}^{ijk} &= \Phi_{**} - \frac{1}{\Delta x}\left(h_{**}^{i+\frac{1}{2},j,k} - h_{**}^{i-\frac{1}{2},j,k}\right) + \frac{\Delta t}{\Delta x}\Phi_{***}^{i,j,k}\left(w^{i+\frac{1}{2},j,k} - w^{i-\frac{1}{2},j,k}\right)
\end{aligned} \tag{2.20}$$

where the subscript in parenthesis indicates the time iteration, with n and $n+1$ being the old and new time steps, and $*$, $**$, and $***$ being the inner sub-iterations. The time step is defined by $\Delta t = t_{n+1} - t_n$ and f, g and h are the numerical fluxes defined as the space/time integration of the product of the velocity and the indicator function H,which is substituted by its approximate counterpart $\hat{H}$:

$$\begin{aligned}
f_{n}^{i+\frac{1}{2},j,k} &= \begin{cases} \frac{1}{\Delta y \Delta z}\int_{\Delta x+}\int_{\Delta y}\int_{\Delta z}\hat{H}_{n}^{i,j,k}dxdydz\ u^{i+\frac{1}{2},j,k} \geq 0 \\ -\frac{1}{\Delta y \Delta z}\int_{\Delta x-}\int_{\Delta y}\int_{\Delta z}\hat{H}_{n}^{i+1,j,k}dxdydz\ u^{i+\frac{1}{2},j,k} < 0 \end{cases} \\
g_{*}^{i,j+\frac{1}{2},k} &= \begin{cases} \frac{1}{\Delta y \Delta z}\int_{\Delta x}\int_{\Delta y+}\int_{\Delta z}\hat{H}_{*}^{i,j,k}dxdydz\ v^{i,j+\frac{1}{2},k} \geq 0 \\ -\frac{1}{\Delta y \Delta z}\int_{\Delta x}\int_{\Delta y-}\int_{\Delta z}\hat{H}_{*}^{i+1,j,k}dxdydz\ v^{i,j+\frac{1}{2},k} < 0 \end{cases} \\
h_{**}^{i,j,k+\frac{1}{2}} &= \begin{cases} \frac{1}{\Delta y \Delta z}\int_{\Delta x}\int_{\Delta y}\int_{\Delta z+}\hat{H}_{**}^{i,j,k}dxdydz\ w^{i,j,k+\frac{1}{2}} \geq 0 \\ -\frac{1}{\Delta y \Delta z}\int_{\Delta x}\int_{\Delta y}\int_{\Delta z-}\hat{H}_{**}^{i,j,k+1}dxdydz\ w^{i,j,k+\frac{1}{2}} < 0 \end{cases}
\end{aligned} \tag{2.21}$$

The temporal integration can be replaced by a spatial integration along the upwind path on the velocity field. For example, in the x-direction the upstream path is $\Delta x+ = \left[x^{i+\frac{1}{2}} - \Delta t u^{i+\frac{1}{2},j,k}, x^{i+\frac{1}{2}}\right]$ for $u^{i+\frac{1}{2}} \geq 0$ or $\Delta x- = \left[x^{i+\frac{1}{2}}, x^{i+\frac{1}{2}} - \Delta t u^{i+\frac{1}{2},j,k}\right]$ for $u^{i+\frac{1}{2}} < 0$. A similar procedure is applied in the other two coordinate directions.

Aside from equations 2.20, an additional equation is solved in order to ensure the divergence-free condition of the fully multi-dimensional operator:

$$\begin{aligned}
\Phi_{n+1}^{ijk} = \Phi_{***} - \Delta t\Bigg(\Phi_{*}^{ijk}\frac{u^{i+\frac{1}{2},j,k} - u^{i-\frac{1}{2},j,k}}{\Delta x} + \Phi_{**}^{ijk}\frac{u_2^{i,j+\frac{1}{2},k} - u_2^{i,j-\frac{1}{2},k}}{\Delta y} + \\
+\Phi_{***}^{ijk}\frac{w^{i,j,k+\frac{1}{2}} - w^{i,j,k-\frac{1}{2}}}{\Delta z}\Bigg)
\end{aligned} \tag{2.22}$$

Once the volume of fluid function has been updated, hence Φ_{n+1} is available, the time integration of the first of equations 2.15 is performed with a *fractional-step method* [KM85] where the evolution equation is advanced in time with a *second-order Adam-Bashforth scheme*, and a *Fast Poisson Solver* is used to enforce zero divergence of the velocity field. Due to the non-uniformity of the density, the Poisson equation used to enforce a divergence-free velocity field results in an equation with variable coefficients, i.e.:

$$\frac{\partial}{\partial x_i}\left(\frac{1}{\rho}\frac{\partial p}{\partial x_i}\right) = \frac{1}{\Delta t}\frac{\partial \hat{u}_i}{\partial x_i} \tag{2.23}$$

2.6 Code validation

This code has been extensively validated using the Zalesak's test case [Zal78] in both 2D and 3D and using a droplet in shear-driven flow and bouyanc-driven flow.

2.6.1 The Zalesak's test case

This test case represents a slotted disk undergoing solid body rotation and it is a standard benchmark to validate numerical schemes for advection problems. The initial shape should not deform under rigid body rotation.

The setup is the same as described by Ii et al. [Ii+12], and two different numerical grids have been taken into consideration by M. E. Rosti while performing the code validation, with 100 and 200 grid points per box size (being the disk of size 0.3), and two different values of the sharpness parameter β already used in 2.22: 1 and 2.

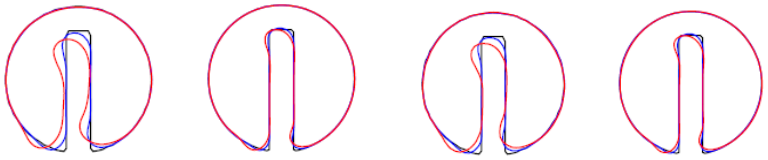

(a) $\beta = 1$ (b) $\beta = 2$

Figure 2.6: The 2D Zalesak's disk: simulation of a slotted disk undergoing solid body rotation.The black line denotes the exact initial solution, whereas blue and red the solutions obtained after one and five full revolutions. For both cases the picture on the left is obtained with 33 numerical grid point, while figure on the right is obtained with 66 numerical grid points. (See [RDVB19])

The deformed shape of the disk shows an overall good agreement with the initial one, with the comparison deteriorating when more rotations are performed. Better agreement is found on the finer grid, and this is further slightly improved in the case with $\beta = 2$. As expected, the major differences are found on the sharp edges of the geometry, which are difficult to maintain undeformed.

Quite good agreement is found between the initial and final shapes, with the difference reducing with increasing resolution.

The same study has been repeated for the 3D case, for two different grids with 33 and 66 grid points.

Again we can find the same behaviour observed in the 2D case.

(a) (b) (c)

Figure 2.7: The 3D Zalesak's disk. From left to right: the exact shape, the deformed shape after 1 full rotation with 33 grid points and the deformed shape after 1 full rotation with 66 grid points. (See [RDVB19])

2.6.2 The droplet test case

We consider a 3D spherical droplet immersed in a flow, located at the center of a computational domain of size $8 \times 4 \times 8$, with a resolution of 16 grid points for the drop diameter. The top and bottom boundaries move with opposite velocity $\pm U$, giving a shear rate $\dot{\gamma} = \frac{U}{2}$, while periodic boundary conditions are imposed in the streamwise x and spanwise z directions. The same density and viscosity are specified for the spherical drop and the surrounding fluid, the Reynolds number is fixed to 0.1, and three Capillary numbers are studied: 0.1, 0.2 to 0.3.

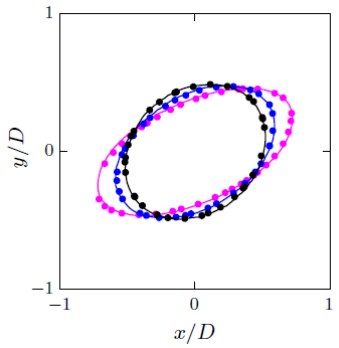

Figure 2.8: Shape of a 3D deformable drop in shear flow for different Capillary numbers. The black, blue, and magenta colors are used for $Ca = 0.1, 0.2$, and 0.3, respectively.(See [RDVB19])

The results obtained by Rosti et al. [Ros+18] are in good agreement with the ones of Ii et al. [Ii+12], reported in fig. 2.8 with dots of the same colours.

Chapter 3

Results

This chapter, in which the outcomes of this work are presented, is subdivided into five subsections: in Sec. 3.1, the introduction, we will discuss the parameter taken into consideration for this study and their effects on the results; in Sec. 3.2 we will discuss the effect of the volume of dispersed phase; in the third Sec. 3.3 we will carry on an analogous synthesis with the effects of the Reynolds number; while in the fourth Sec. 3.4 we will underline the combined effect of these two parameters and, lastly, in the fifth one Sec. **??** we will shed light on the mechanism of heat conduction in multiphase turbulent flows and point to possible future developments of this area of study.

N.B. In this Chapter are taken into account all the results derived from the computation for the sake of clarity and comprehensiveness. They are put into the adequate order, that is the most suitable for the description of the phenomena according to the author. However we must assert that the results of the cases with percentage of dispersed phase equal to 15%, that is to say cases XIII, XIV, XV and XVI, appear to be shifted from the common trend of the cases with other Φ percentage.

3.1 Introduction

In order to compare the effects of Reynolds number and second phase percentage, simulations with the following Reynolds number and second phase percentage have been carried out:

Re \ **Φ**	5%	10%	15%	20%	25%
700	X	XI	XVI	XII	XX
1400	IV	V	XV	VI	XIX
2100	VII	VIII	XIV	IX	XVIII
2800	I	II	XIII	III	XVII

Table 3.1: Overview of the cases for the study of turbulent shear stresses.

Thus 20 different simulations have been processed for what concerns the study shear stresses in turbulence and 3 additional simulations have been developed in order to observe the effects of wall heat convection in a turbulent multiphase flow.

Re \ **Φ**	5%	20%
1400	QIV	QIII
2800	QII	QI

Table 3.2: Overview of the cases for the study of turbulent heat transmission.

Despite the number of data collected not all of the cases will be taken into consideration, but in Sec. 3.2 and Sec. 3.3 we will consider only the limit cases and an intermediate case. On the contrary, to consider the whole global effect in Sec. 3.4 we will take into account all the 20 cases in order to obtain 3D maps that set the separation between one regime to another.

Volume of dispersed phase The volume of dispersed second phase is defined as

$$\Phi = \frac{\Phi_{2P}}{\Phi_{1P}} \tag{3.1}$$

The influence of this parameter on the mean flow results mainly in significant increase of the bubble shear stresses along with the increase of Φ. This phenomena is due to the

larger amount of bubbles of second phase present in the mean flow, thus resulting in a more effective dissipation of momentum due to the interaction between the bubbles.

Reynolds number Along the course of this study we used Reynolds number with values 700, 1400, 2100 and 2800. With the increase of Reynolds number we observe an augment of the Reynolds stresses in the shear stresses decomposition. In fact for higher Reynolds number the velocity fluctuations assume greater magnitude and hence the module of the component of the Reynolds stress tensor increases as a consequence.

$$\tau_{Re} = -\rho\widehat{u_i' u_j'} \tag{3.2}$$

Note that we have used the Reynolds number calculated on half the width of the channel $h = \frac{l_z}{2}$. This is an arbitrary choice, dictated by the convenience and by the fact that the profiles of the characteristics are symmetrical along the width of the channel. Furthermore this is the most common solution that can be found in the literature concerning plane channel flows.

$$Re = Re_{\frac{l_z}{2}} = \frac{\rho V h}{\mu} \tag{3.3}$$

For instance in the study [Las+16], the Reynolds number was calculated using the full width of the channel as a spacial dimension.

Weber number The Weber number is defined as:

$$We = \frac{\rho V^2 L}{f_i} \tag{3.4}$$

and it accounts for the balance between inertial forces and surface tension. Hence if a multiphase flows, such as a liquid spray in still air, presents an high Weber number, the inertial forces will be times greater than the surface tension which tends to maintain the fluid particles together and this will result in dispersed jet of thousands of small droplets. On the other hand if a flow presents a low Weber number the jet will results in a few large bubbles, or at the furthest even in just one mass of coherent fluid, floating in the still air. For our case of study the Weber number remain unvaried since it depends on density, bulk velocity, characteristic length and surface tension. We have not varied any of the previous parameters along this study and, in order to obtain a variation of the Reynolds number, we have implemented a different viscosity, which does not affect the Weber number. Consequently we have worked at constant Weber number and we should observe the same mean behaviour of the bubbles in every case, despite having a larger number of them in the cases with larger Φ. The characteristic length taken into account for this study is the semi-width of the channel along the z coordinate, that is to say $l_z/2 = 1$. We obtain:

$$We = \frac{\rho V^2 \frac{l_z}{2}}{f_i} = 571.43 \simeq 600 \tag{3.5}$$

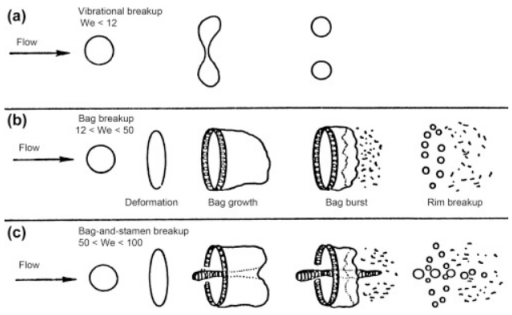

Figure 3.1: Comparison of break-up of large drop into small droplets for different Weber numbers. See [LF88]

The Weber number taken into account along the course of this study is elevate, thus the bubbles of dispersed phase are very likely to broke into smaller droplets. We will observe the effects of this parameter later on.

Capillary number The Capillary number is defined as:

$$Ca = \frac{\mu V}{\sigma} \tag{3.6}$$

It represents the effect of viscous drag forces versus surface tension forces acting across an interface between a liquid and a gas, or between the two phases of an emulsion flow. It accounts for the balance between viscous forces that tend to deform second phase droplets within the main phase and surface tension forces that tend to minimize the surface of the interface.

A flow with higher Capillary number tend to present higher deformations of bubbles, while a flow with low Capillary number tend to present spherical bubbles.

Capillary number varies from one simulation to another since it is proportional to dynamic viscosity μ.

Re	700	1400	2100	2800
Ca	0.82	0.41	0.27	0.20

Table 3.3: Capillary number values taken into account.

As a consequence we observe more spherical bubble for higher Reynolds number while for the cases with lower Reynolds number we observe more elongated, deformed bubbles.

3.2 Effects of the variation of volume of dispersed phase

We observe the effects of the volume of dispersed second phase on the mean flow while maintaining constant Reynolds number. We chose as a chase of study three different Reynolds number that are, ranging from the lowest to the highest: 700, 1400 and 2800.

3.2.1 Re=700

In the following diagram we represent the velocity profile in dimensionless *wall units*, that is to say that axial velocity and wall-normal coordinate, in our case of study z, are divided by characteristic values of velocity and length in order to obtain universal profiles of velocity.

$$u^+ = \frac{u}{u_\tau} \tag{3.7}$$

$$z^+ = \frac{z u_\tau}{\nu} \tag{3.8}$$

where u_τ is called *friction velocity*, $u_\tau = \sqrt{\frac{\tau_w}{\rho}}$.

The velocity profile should hence assume a characteristic trend given by the *law of the wall*. According to this law there is an area in which the effects of viscosity creates a gradient of mean velocity along the wall-normal coordinate, hence creating a velocity profile. This zone is the so called *boundary layer*, present in every viscous flow. Since the flow is also turbulent are present velocity fluctuations along the three physical directions both inside and outside the boundary layer. The only differences is that within the boundary layer is also present a gradient of velocity along the wall normal coordinate, while out of the boundary layer the mean velocity is *homogeneous* and there are no velocity gradients in space. The *turbulent boundary layer*, is subdivided into different areas along the dimensionless wall-normal coordinate z^+. The first subdivision is between the *inner layer* and the *outer layer*. In the first one the profile of velocity is determined only by u_τ and y^+, independently from the U_{bulk} an the geometry, while in the outer layer the direct effects of viscosity on the mean flow are negligible.

On the other hand the inner layer could be subdivided into inner layers in its turn. The velocity profile adjacent to the wall in turbulence assume a characteristic trend depending on which zone we are observing. Commencing from the wall surface and going further into the mean bulk fluid we observe a first area, called *viscous sublayer*, for $0 < z^+ < 5$, in which the transmission of momentum between the fluid veins, included the one adjacent to the wall, is still dominated by viscosity. Hence we observe a linear trend for the velocity in wall coordinates. The other major area is the *logarithmic layer*, going from $30 < z^+ < 50$, in which the velocity profile is given by an analytical law in which the logarithm is present. The two layers are separated by the buffer layer, in which is present a junction between the two velocity profiles, the logarithmic one and the linear one. For $z^+ > 50$ we encounter the *overlap region*, within the boundary of the inner layer.

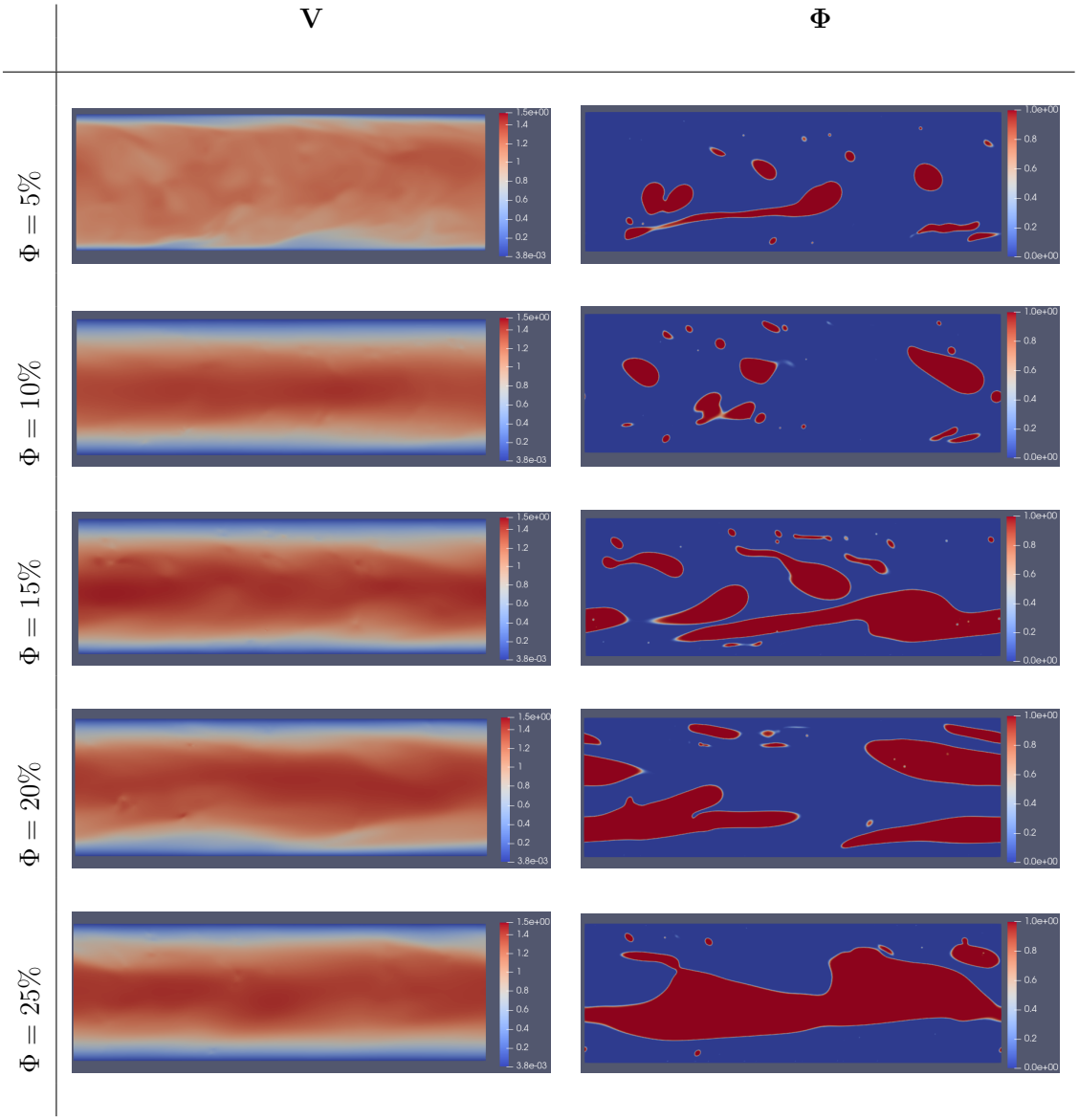

Figure 3.2: Rendering of axial velocity V and bubbles distribution along the channel on the x-z plane for $Re = 700$.

Taking Figure 3.3 as a reference we can observe how the wall velocity decreases along with the increase of Φ. This outcome would suggest that the presence of dispersed phase in emulsion flows has decreased the level of turbulence, resulting in steeper gradients of velocity near the wall for flows with low presence of dispersed phase, and smoother gradients of velocity for flows with higher presence of dispersed phase.

This effect is enlightened in Figure 3.4, where are clearly reported the velocity profiles for a laminar flow and a turbulent flow in a pipe with circular section.

Region	Layer	Velocity law	Domain
Inner layer $\left(0 < \frac{z}{\delta} < 0.1\right)$	viscous sublayer	$u^+ = z^+$	$0 < z^+ < 5$
	buffer layer	-	$5 < z^+ < 30$
	logarithmic layer	$u^+ = \frac{1}{\kappa} \log z^+ + C$	$30 < z^+ < 50$
	overlap region	-	$z^+ > 50$
Outer layer $\left(0.1 < \frac{z}{\delta} < 1\right)$			

Table 3.4: Subdivision of the turbulent boundary layer.

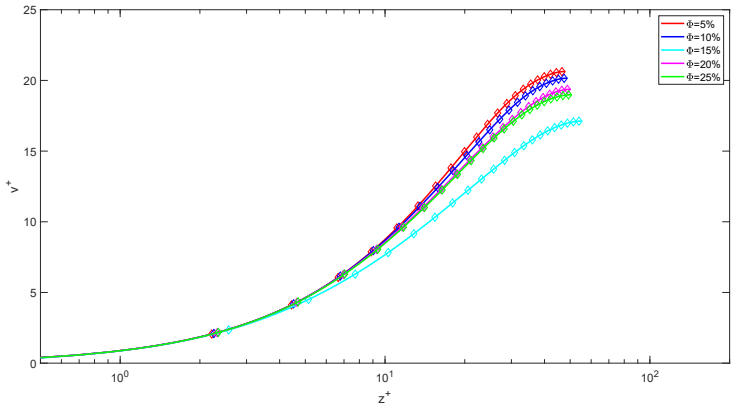

Figure 3.3: $v^+(z^+)$ at Re=700.

However, since we have taken into account a flow with Reynolds number equal to 700, thus resulting in a completely laminar flow, we cannot accept turbulence as an explanation for the flattening of the velocity profile.

The gradient of velocity along the wall-normal direction accounts for the balance of momentum transport along this direction. We must consider that the diffusive transport between the two phases is the same, given that the viscosity is equal between the two phases, hence the advective transport has increased in the cases with larger percentage of dispersed phase.

Looking at equation 3.9 we can assert that, given that the pressure gradient is constant along the axial direction of the flow, the convective and diffusive terms must balance themselves in order to have a sum equal to zero.

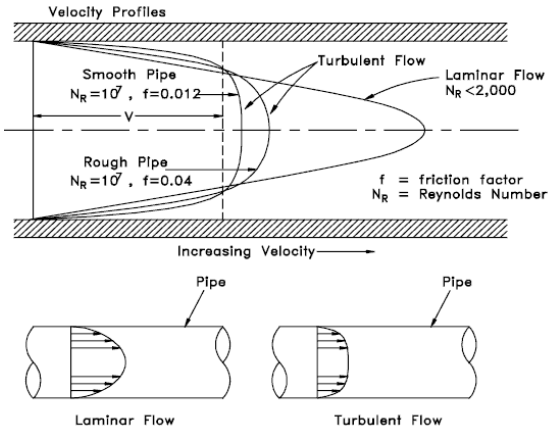

Figure 3.4: Velocity profiles in a pipe flow.

$$\frac{\partial \overline{p}}{\partial y} + \frac{\partial}{\partial z}\left(\mu \frac{\partial \overline{v'}}{\partial z} - \rho \overline{v'w'}\right) = 0 \tag{3.9}$$

where the quantities under the bar ($\bar{\cdot}$) refer to the time average of the quantity.

In conclusion it seems that the presence of dispersed phase increase the momentum transport across the width of the channel. Given that the two phases have equal viscosity this increase in momentum transport can only be attributed to an increment in advective transport due to the velocity fluctuations along the wall-normal direction across the width of the channel. This leads to a plateau shaped velocity profile along the width of the channel, the more elevated the percentage of dispersed phase is, the more flattened is the velocity profile. This effect is clearly visible in Figure 3.13a.

However, even if the behaviour of the flows resembles the behaviour of a turbulent flow, we must state the this flow is not turbulent, in fact the spectrum of the velocity fluctuations presents a peak for a peculiar frequency and it is not distributed along many frequencies as the spectrum of a turbulent flow should be.
Hence we can assert that the cases with Re=700 are *laminar* for every percentage of dispersed phase.

Looking at Figure 3.6a we can observe how the velocity profile assumes a more parabolic trend along with the decrease of percentage of dispersed phase, while for higher values of Φ it assumes a flatter profile. The first derivative of the axial velocity with respect to the wall normal coordinate, hence $\frac{\partial v}{\partial z}$, is directly proportional to the wall shear stress. This value, graphically expressed by the tangent to the velocity profile at $z = 0$. Consequently we can state that the value of the wall shear stress increases along with the increase of Φ.

For what concerns the turbulent velocity fluctuations along x and z axes we can deduce from figures 3.6c and 3.6b that if we increase the second phase percentage the peaks of velocity fluctuations move towards the outer channel. This phenomena is due to the fact that velocity fluctuations are smaller in second phase bubbles and, since they migrate

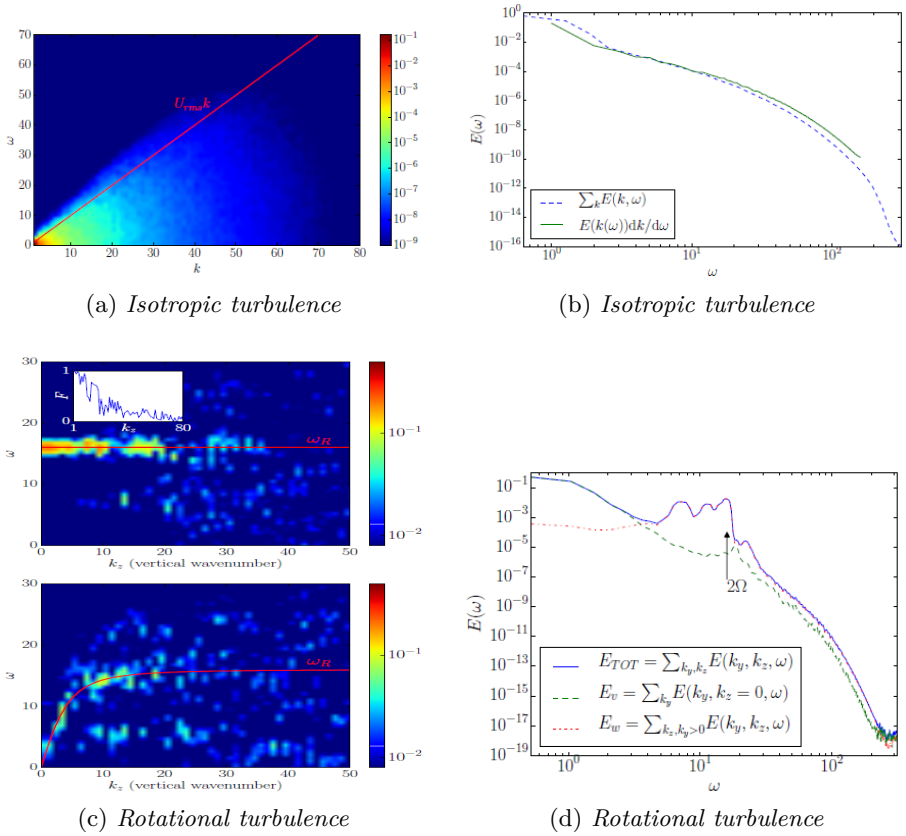

(a) *Isotropic turbulence* (b) *Isotropic turbulence*

(c) *Rotational turbulence* (d) *Rotational turbulence*

Figure 3.5: Energy spectrum comparison between isotropic turbulence and rotating turbulence flows. On the lower figures, the spectra of rotating turbulence present the largest peak in E_w corresponds to a frequency 2Ω, indicated by the arrow, while the spectrum of the isotropic turbulence is evenly distributed along the entire frequency spectrum in the upper figures. See [Geo+18].

towards the center of the channel with the increase of Φ, the peak in velocity fluctuations moves towards $z = \frac{1}{3}\frac{l_z}{2}$. On the contrary in the more dispersed cases the bubbles are equally distributed along the width of the channel and the velocity fluctuations peaks tend to be towards the centreline of the channel.
This effect is clearly visible in Figure 3.6c, representing the velocity fluctuations parallel to the axial velocity, $v'v'/U^2_{bulk}$. Note that the velocity oscillations in Figure 3.6c are slightly larger than the ones in Figure 3.6b, because the turbulence, even if is isotropic, presents larger velocity fluctuations along the flow bulk velocity.

For what concerns the quantity $v'w'$, representing the non-diagonal component of the Reynolds stress tensor R_{ij}, it accounts for the shear stress produced by the cross velocity fluctuations. From Figure 3.6d we infer that the profile assumes linear growth rate between the two peaks located at $z = 0.3h$ and $z = 1.7h$, where $h = \frac{l_z}{2}$ represent the semi-width of the channel, and its value is 0 at the centreline.

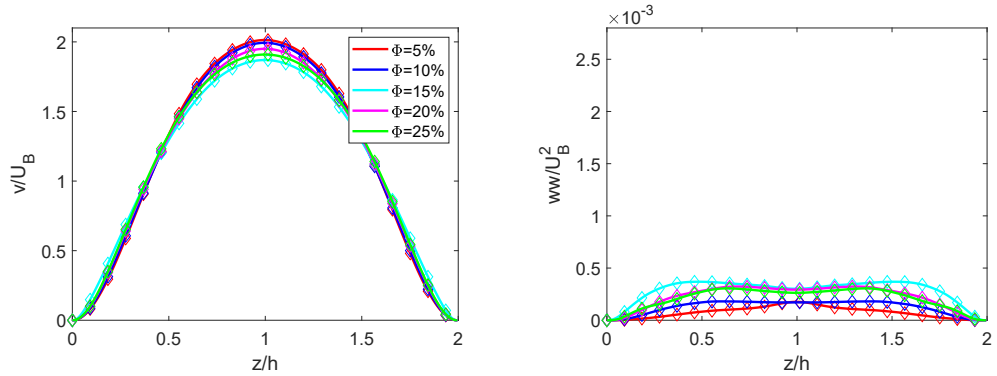

(a) $\frac{v(z)}{U_{bulk}}$ *at Re=700* (b) $\frac{w'w'(z)}{U^2_{bulk}}$ *at Re=700*

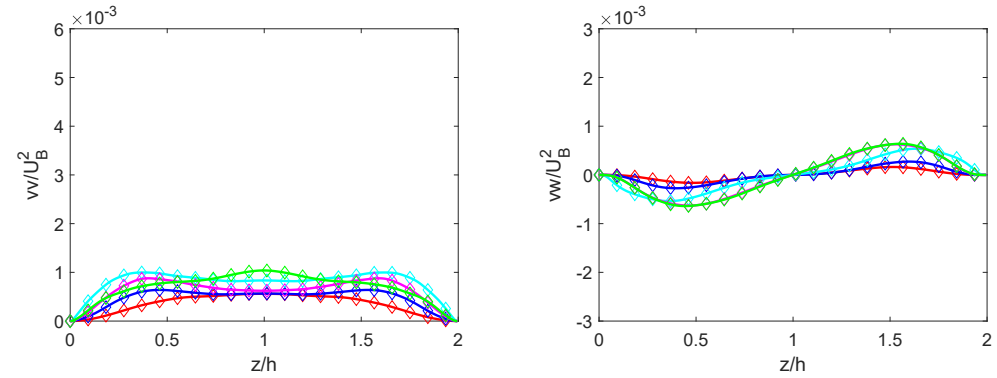

(c) $\frac{v'v'(z)}{U^2_{bulk}}$ *at Re=700* (d) $\frac{v'w'(z)}{U^2_{bulk}}$ *at Re=700*

Figure 3.6: Velocity fluctuations at Re=700.

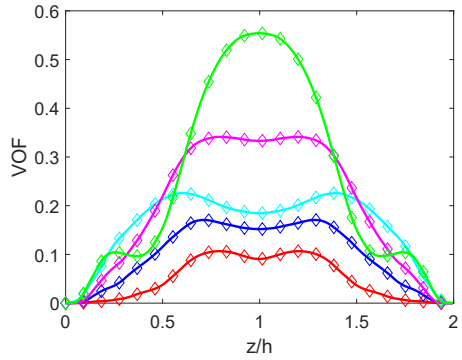

Figure 3.7: VOF at Re=700.

Moreover we can predict that for cases with high percentage of dispersed phase the bubbles of this phase will be confined to a smaller region towards the centreline of the channel.

This effect is clearly visible from Figure 3.7.
Consistently with the outcomes of the diagrams 3.6c and 3.6b we underline the link between the turbulent velocity fluctuations and the presence of the second phase. The second phase bubbles affects the turbulence field and mitigate the velocity fluctuations.

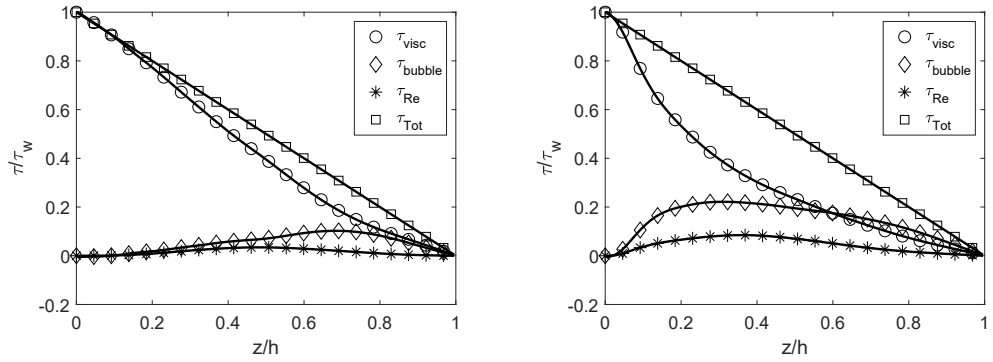

(a) $\tau(z)$ *at* $\Phi = 5\%$ (b) $\tau(z)$ *at* $\Phi = 15\%$

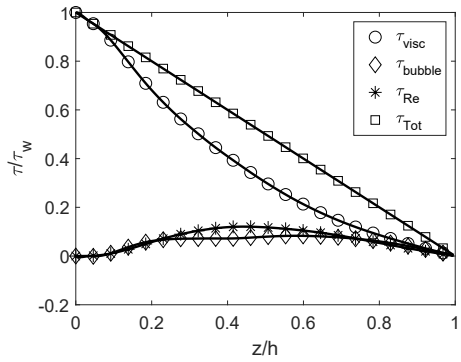

(c) $\tau(z)$ *at* $\Phi = 25\%$

Figure 3.8: Shear stress decomposition at Re=700.

For what concerns the stress decomposition it is appropriate to state the way in which the stresses have been computed along the course of the present study.
In general, single-phase flows undergo only shear stresses induced by viscosity and normal stresses induced by hydrostatic pressure. The first component disappears when the fluid is in static conditions.
In the peculiar case of multi-phase flows a new source of stresses generation arises, that is to say the interaction between bubbles via the surface tension forces. This phenomena has already been treated along the present study in Chapter 2.5.

Hence in this specific case of flows characterized by Reynolds number equal to 1400, or rather in *turbulent regime*, we encounter the presence of three different types of shear stresses in the bulk flow: *viscous shear stresses*, *Reynolds stresses* and the third component arising from surface tension, that has been indicated with the nomenclature *bubble shear*

stresses in the present document.

The stresses have been computed in this code using the following method:

- **Reynolds stresses** τ_{Re}, are computed by extracting the $v'w'$ components from the output text files for each iterations and then are time and space average thus obtaining $\tau_{zy} = \overline{v'w'}$;
- **Viscous shear stresses**, due to viscous transport. These stresses are computed by multiplying the first derivative of the axial velocity along the wall-normal coordinate $\frac{\partial V}{\partial z}$ for the viscosity μ using a forward first order numerical scheme: $\mu\frac{\partial V}{\partial z} \simeq \mu\frac{V_{i+1}-V_i}{z_{i+1}-z_i}$;
- **Total shear stresses**, due to the joint action of all the above components, they are computed by linear interpolation between the shear stress at the wall, which is due to viscosity, and the centreline in which the total amount of shear stresses is equal to 0;
- **Bubble stresses** τ_{bubble}, the last ones to be computed, they are calculated by subtracting τ_{Re} and τ_{bubble} from the total stresses for each cell along the width of the channel.

In the above figures, Figure 3.8a, 3.8b and 3.8c, we observe that the stress profile goes from a finite value (positive) at the wall region to a null value at the left end side. This happens because the above figures are drafted on half-channel. But if we take the shear stress profile along the entire channel we observe that the stress profile shows an anti-symmetric trend, ending in a finite negative value to the left end side, which has the exact same value in module as the τ_{wall} at the left end side.
See Figure 3.9.
Hence the diagram of the shear stress along the entire width of the channel is anti-symmetric. This characteristic is due to the fact that the shear stresses represents the momentum transport between adjacent fluid streamlines and thus they are proportional to $\frac{\partial V}{\partial z}$. As is well known to compute the derivative we have to set a coordinate reference system. In our case the *z axis* points upwards and hence it is straightforward that, with a parabolic velocity profile, the derivative will be positive for the first half of the channel and will be negative for the second half of the channel, giving origin to the anti-symmetric stress profile.

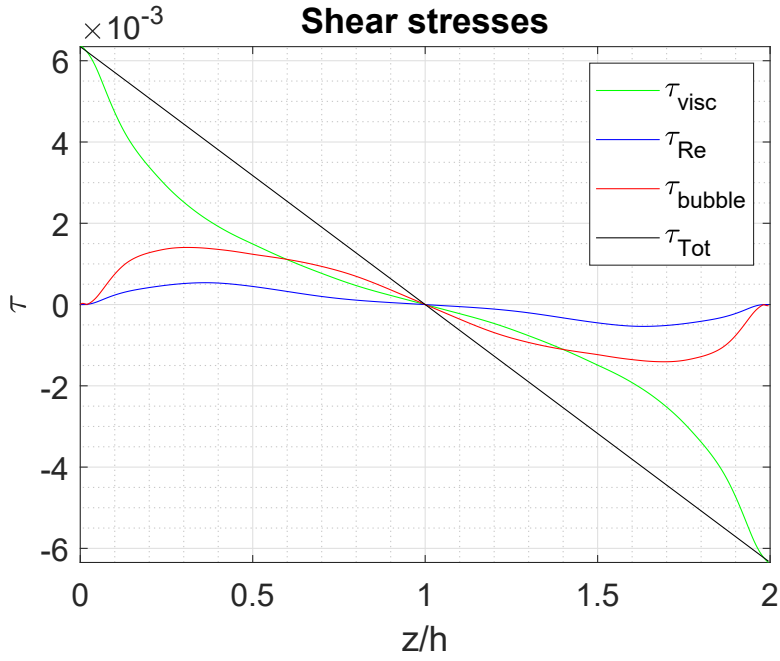

Figure 3.9: $\tau(z)$ along the entire channel width for $Re = 700$ and $\Phi = 15\%$.

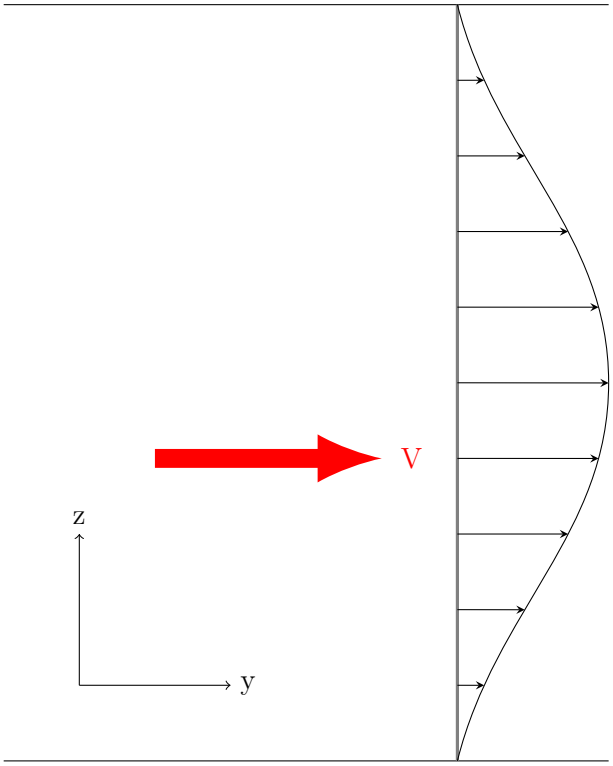

Figure 3.10: Dimensional velocity profile with coordinate reference system

3.2.2 Re=1400

In this section a more turbulent flow field is taken into account, hence it is expected that it will undergo typical phenomena of the turbulent flow fields such as instantaneous velocity fluctuations and the presence of eddies, vortices and streaks.

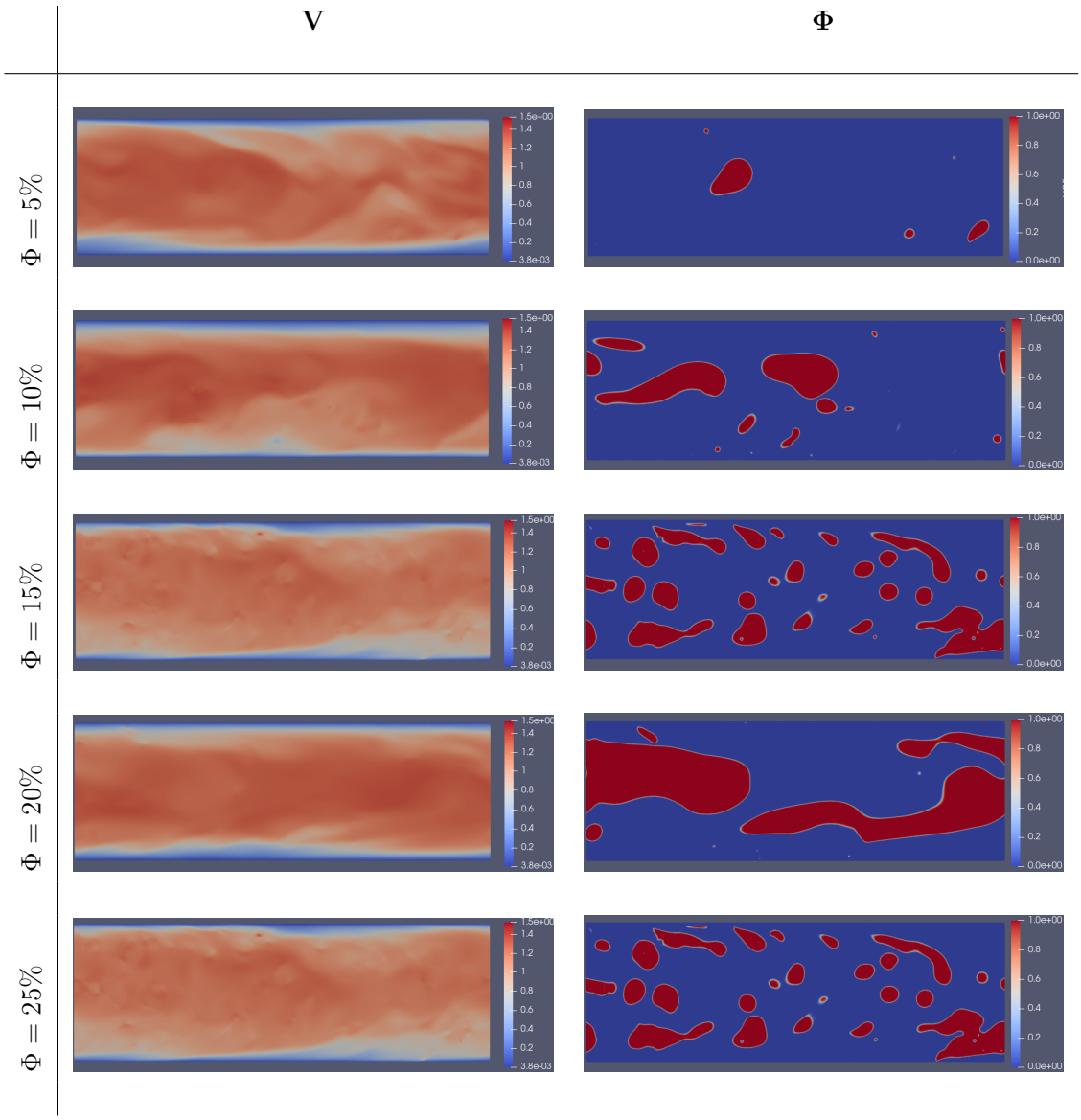

Figure 3.11: Rendering of axial velocity V and bubbles distribution along the channel on the x-z plane for $Re = 1400$.

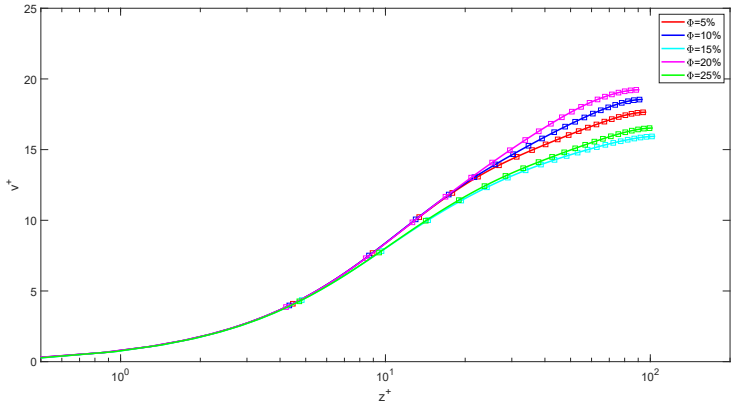

Figure 3.12: $v^+(z^+)$ at Re=1400.

In Figure 3.12 we can see how the dimensionless velocity profiles for the various percentages of second phase are much closer on to another in comparison with Figure 3.3, but they present an opposite trend for $\Phi \leq 15\%$ with respect to the ones in Figure 3.3. Hence we can state that the presence of a dispersed phase alters the structure of the bulk flow in turbulent regime.
Here the presence of a dispersed phase creates a more parabolic velocity profile, hence it causes a less steep velocity gradient near the wall and a lower drag coefficient.
This phenomena is also visible in figure 3.13a along the entire width of the channel in dimensional coordinates.
For what concerns the bulk structure of the flow it is important to observe that the higher the percentage of dispersed phase is, the more the bubbles tend to migrate towards the centreline of the channel.
Hence along the walls of the channel there is a scarcity of dispersed phase and this is due to two main reasons:

1. there are less bubbles of dispersed phase;
2. the bubbles are smaller and similar to droplets.

In our case the second mechanism appears to be more plausible, since the Weber number calculated in Sec. 1.7 is high and the bubbles tend to break up into smaller droplets. This phenomena is more effective along the walls, where there are small vortices, called *streaks*, whose axes are parallel to the y axis and parallel to the wall.
These streaks creates high recirculation and mixing of the flow in the regions along the walls, in both laminar and turbulent regimes, that contributes to the advective transport of momentum. On the other hand it creates steep gradient of velocity along the wall normal coordinate and elevate shear stresses that break up the bubbles into smaller droplets. The elevate value of the Weber parameter ($We \simeq 600$) allow this break-up mechanism.

For what concerns the shear stresses profile we observe that the Reynolds stresses play the major role in contributing to the total stress, as we see for the figures above.

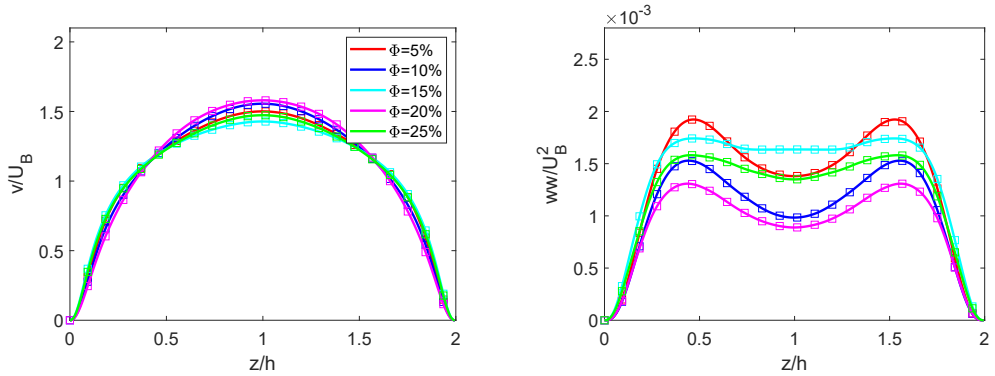

(a) $\frac{v(z)}{U_{bulk}}$ *at Re=1400* (b) $\frac{w'w'(z)}{U^2_{bulk}}$ *at Re=1400*

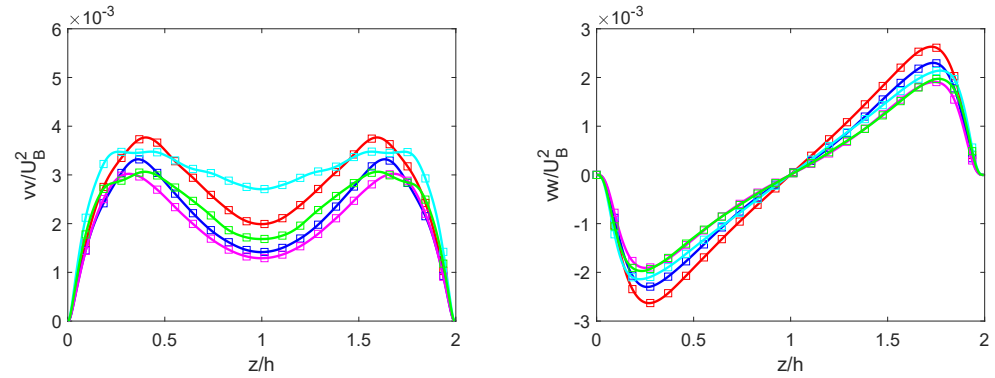

(c) $\frac{v'v'(z)}{U^2_{bulk}}$ *at Re=1400* (d) $\frac{v'w'(z)}{U^2_{bulk}}$ *at Re=1400*

Figure 3.13: Velocity fluctuations at Re=1400.

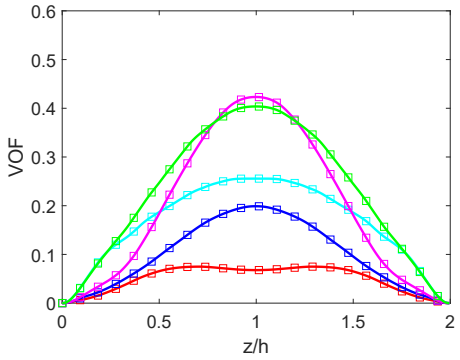

Figure 3.14: VOF at Re=1400.

Even though we are in turbulent regime, with the increase of dispersed phase we notice that τ_{bubble} assume larger magnitude, ending up at the same magnitude order of Reynolds

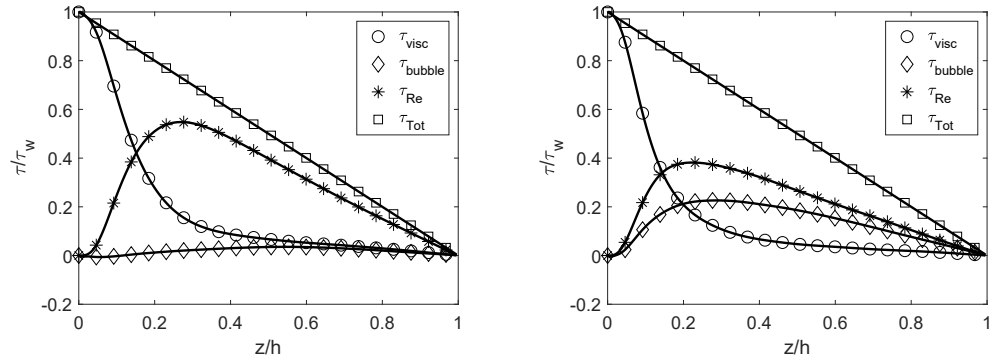

(a) $\tau(z)$ *at* $\Phi = 5\%$ (b) $\tau(z)$ *at* $\Phi = 15\%$

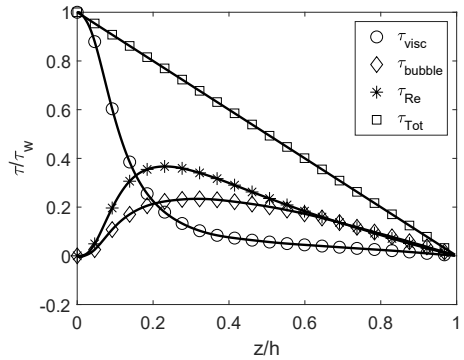

(c) $\tau(z)$ *at* $\Phi = 25\%$

Figure 3.15: Shear stress decomposition at Re=1400.

stresses in Figure 3.15c for $Re = 1400$ and $\Phi = 25\%$.

3.2.3 Re=2800

In this section we can state that we are in fully developed turbulence according to the velocity fluctuations spectrum. The most important feature of the turbulent flow field is that the presence of significant instantaneous fluctuations in the velocity fields in both direction and magnitude become the major mechanism of fluid mixing and momentum transport. As we stated in the previous section, a similar mechanism is present in the multi-phase flow even in low Re regimes due to the presence of the dispersed phase.

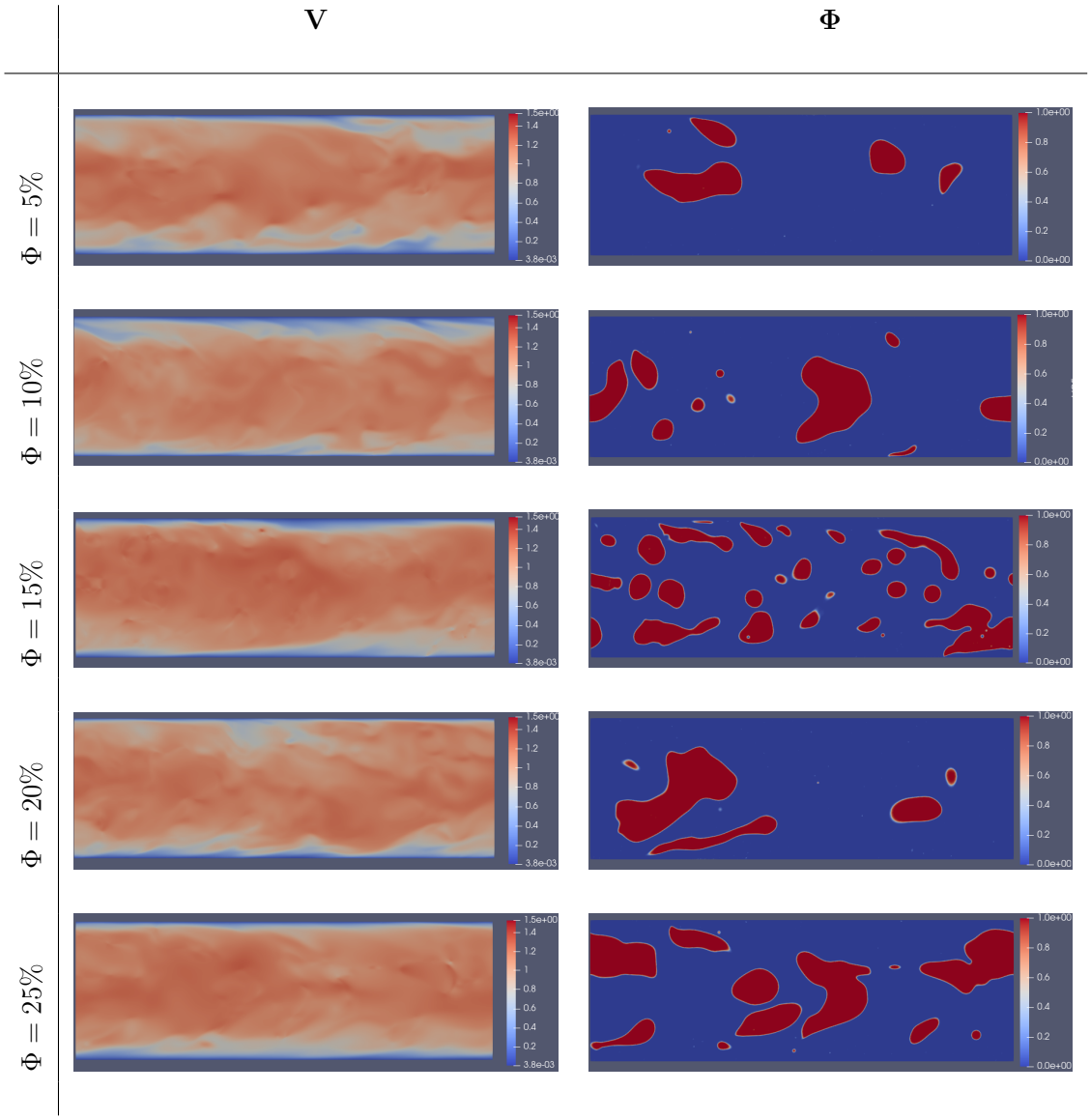

Figure 3.16: Rendering of axial velocity V and bubbles distribution along the channel on the x-z plane for $Re = 2800$.

Now we must observe whether or not the turbulence emphasize or mitigates this phenomena.

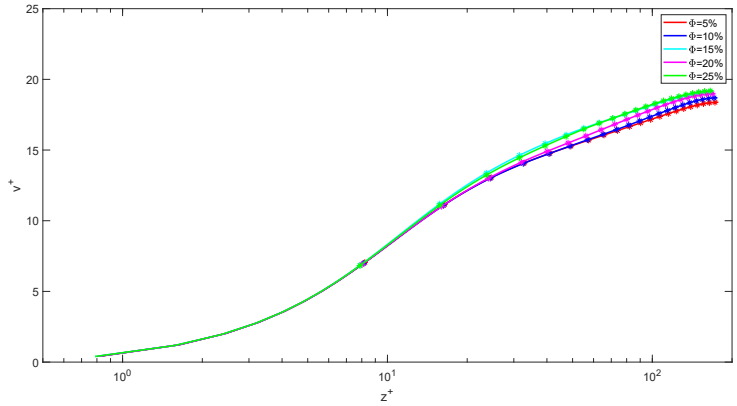

Figure 3.17: $v^+(z^+)$ at Re=2800.

In Figure 3.17 the same trend observed for $Re = 1400$ is repeated, even though now the velocity profile in wall coordinates are more aligned towards a common trend. We deduce that with progressing to high Reynolds number the dimensionless velocity profile in wall coordinates tend to assume a universal form.

Note that in every diagram with the velocity profile, with variation of both Φ and Re, the lines are overlapped towards the left end side of the diagram, hence very close to the wall surface. This is due to the fact that the velocity is divided by u_τ for every case.

In Figure 3.18a we observe that the presence of the dispersed phase causes the flattening of the velocity profile along the channel width, even if this effect is remarkably less effective than in the case with $Re = 700$.
In Figures 3.18c and 3.18c we observe that the velocity fluctuations have increased in comparison with the cases at $Re = 1400$ and $Re = 1700$, as expected, and the ones in Figure 3.18c are much larger than the ones in Figure 3.18b. This is due, as aforesaid, to the fact that the velocity fluctuations along the flow direction are large than the ones along the other two directions and we could deduce a common trend that the velocity fluctuations $v'v'$ are 1.2 times bigger than the $w'w'$ fluctuations.

The fluctuations $v'w'$, which represents the shear stresses as aforementioned, are larger in Figure 3.18d than in Figures 3.6d and 3.13d.

In Figure **??** we obtain the confirm of the trend that we have supposed in the previous Section. The bubbles tend to migrate towards the centreline of the channel along with the increase of percentage of dispersed phase.

As we stated previously, the Reynolds stresses contribute to the major part of the shear stresses in the bulk flow in turbulent flows, and in this case with $Re = 2800$ this effect is magnified. With the increase of the percentage of dispersed phase the bubble stresses assume a larger and larger contribution to the total shear stress, as we see in Figures 3.20c

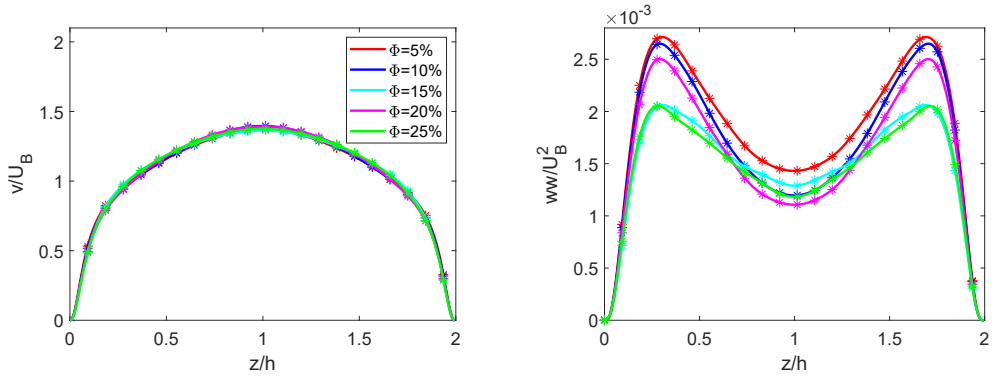

(a) $\frac{v(z)}{U_{bulk}}$ *at Re=2800* (b) $\frac{w'w'(z)}{U^2_{bulk}}$ *at Re=2800*

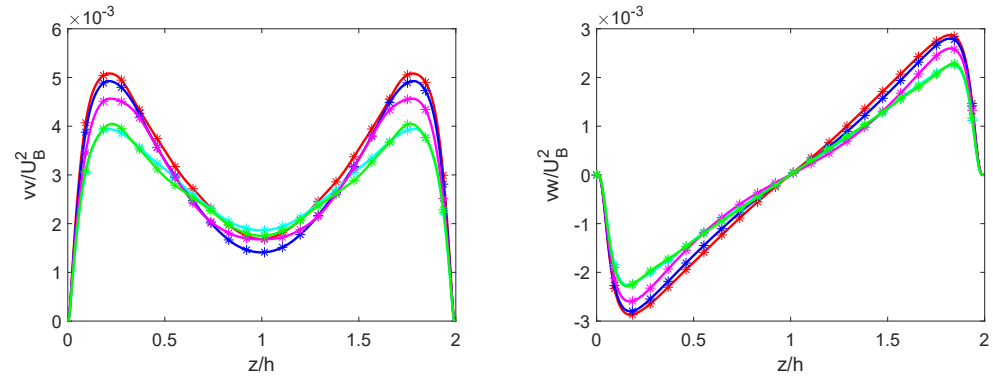

(c) $\frac{v'v'(z)}{U^2_{bulk}}$ *at Re=2800* (d) $\frac{v'w'(z)}{U^2_{bulk}}$ *at Re=2800*

Figure 3.18: Velocity fluctuations at Re=2800.

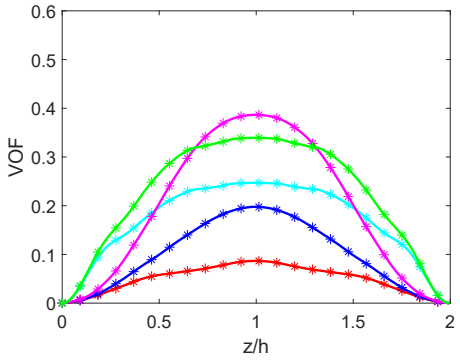

Figure 3.19: VOF at Re=2800.

and 3.20b in comparison with Figure 3.20a. Even so in fully developed turbulence the Reynolds stresses are times larger than the viscous and bubbles ones, as we can deduce

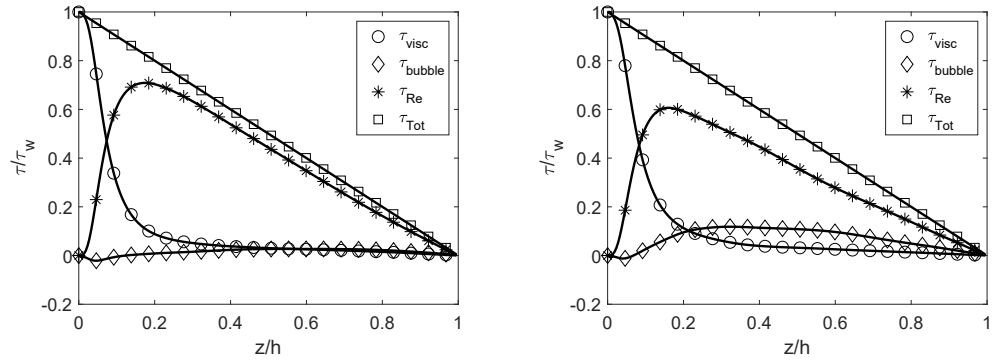

(a) $\tau(z)$ *at* $\Phi = 5\%$ (b) $\tau(z)$ *at* $\Phi = 15\%$

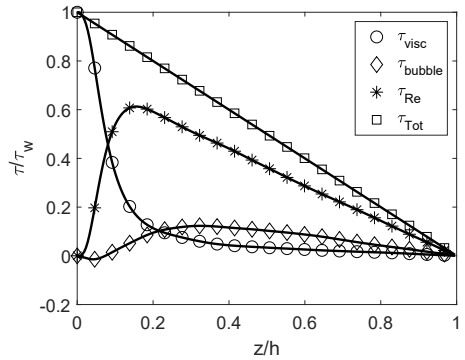

(c) $\tau(z)$ *at* $\Phi = 25\%$

Figure 3.20: Shear stress decomposition at Re=2800.

from the figures above.

3.3 Effects of the variation of Reynolds number

In this Section we observe the effects of the increase of Reynolds number on the mean flow while maintaining constant percentage of the dispersed phase. We chose as a chase of study three different values of Φ that are, ranging from the lowest to the highest: 5%, 15% and 25%.
As stated at the beginning of this Chapter, the case with $\Phi = 15\%$ is not fully reliable since its outcomes deviate from the common trend.

3.3.1 $\Phi = 5\%$

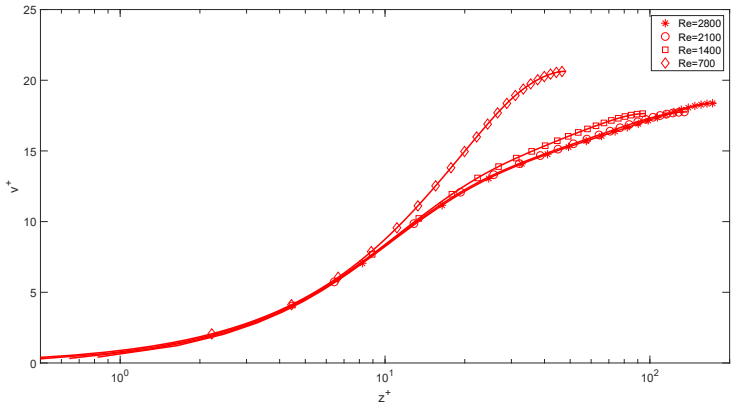

Figure 3.21: $v^+(z^+)$ at $\Phi = 5\%$.

In Figure 3.21 we observe that the diagrams of the velocity along the wall-normal coordinate in wall coordinates assume the same trend for the turbulent cases, while the laminar case with $Re = 700$ presents a velocity profile that stands apart from the others, well above the others.
Hence we deduce that the laminar case shows a more parabolic velocity profile, while turbulent cases present the typical flattened velocity profile. This trend is confirmed in Figure 3.22a as well.

In figure the mean velocity profile across the width of the channel assume a flatter shape, as expected in turbulent flows, while for low Reynolds number, see line with diamond markers equivalent to $Re = 700$, it assumes the parabolic shape similar to the Poiseuille profile, with the velocity field mostly distributed around the centreline. This is underlined in Figure 3.23.

This phenomena produces a higher gradient of velocity along the wall-normal coordinate in the turbulent case and thus a higher value of the wall shear stress, see Eq. 3.10. In fact in pipe flows in turbulent regime present a higher value of the friction coefficient in comparison with laminar ones.

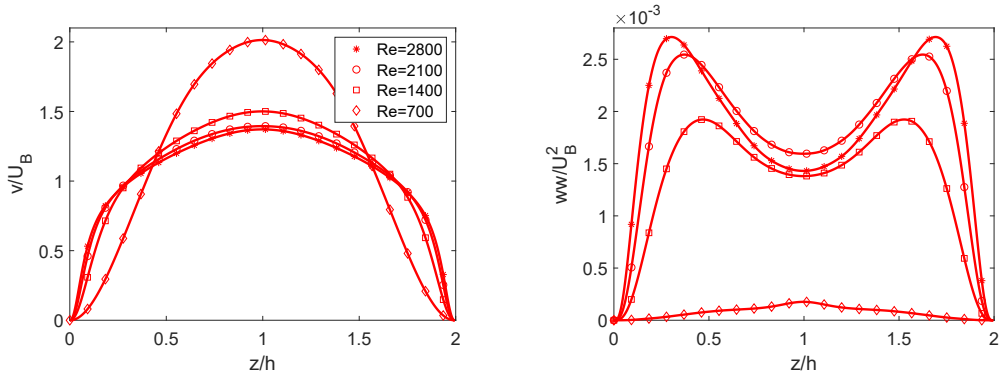

(a) $\frac{v(z)}{U_{bulk}}$ *at* $\Phi = 5\%$ (b) $\frac{w'w'(z)}{U^2_{bulk}}$ *at* $\Phi = 5\%$

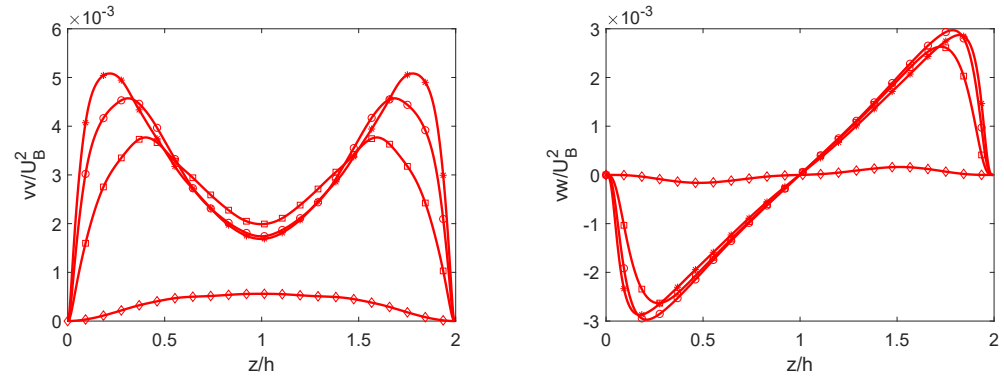

(c) $\frac{v'v'(z)}{U^2_{bulk}}$ *at* $\Phi = 5\%$ (d) $\frac{v'w'(z)}{U^2_{bulk}}$ *at* $\Phi = 5\%$

Figure 3.22: Velocity fluctuations at $\Phi = 5\%$.

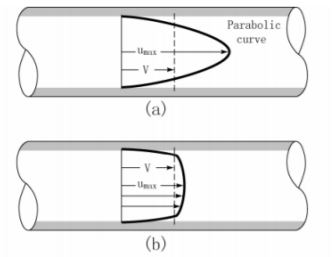

Figure 3.23: Velocity profile in a pipe for laminar (a) and turbulent (b) flow ([Pip]).

$$\tau_w = \mu \left(\frac{\partial u}{\partial y} \right)_{y=0} \tag{3.10}$$

This effect was already studied by L. F. Moody [1] in 1944, resulting in the diagram which bears his name, reported in Figure 3.24.

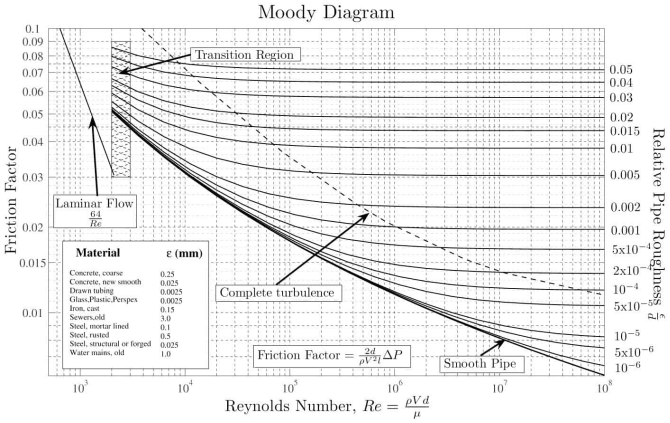

Figure 3.24: Moody's diagram for drag coefficient in pipe flows.

In the Moody's diagram it is clearly visible that turbulent flows in pipes have a larger friction factor with respect to the laminar flows. Note that this chart refers to pipes with circular section and presents different trends for different roughness coefficient.

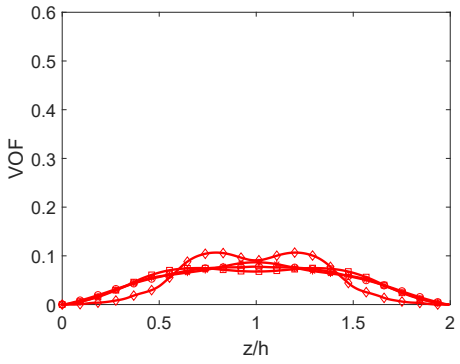

Figure 3.25: VOF at $\Phi = 5\%$.

From Figure 3.25 we deduce that turbulence acts with a scattering effect and distributes the bubbles more uniformly across the channel width. In fact the case with $Re = 700$ represented with the diamond markers, presents two peaks corresponding to $z = \frac{3}{4}h$ and $z = \frac{5}{4}h$. With the increase of dispersed phase in the flow it is observed a more remarkable migration of the bubbles towards the centreline, as reported in the following sections.

[1] *Lewis Ferry Moody* (5 January 1880 - 21 February 1953) was an American engineer and professor, best known for the Moody chart, a diagram capturing relationships between several variables used in calculating fluid flow through a pipe. He was the first Professor of Hydraulics in the School of Engineering at Princeton, and he owned 23 patents for his inventions.

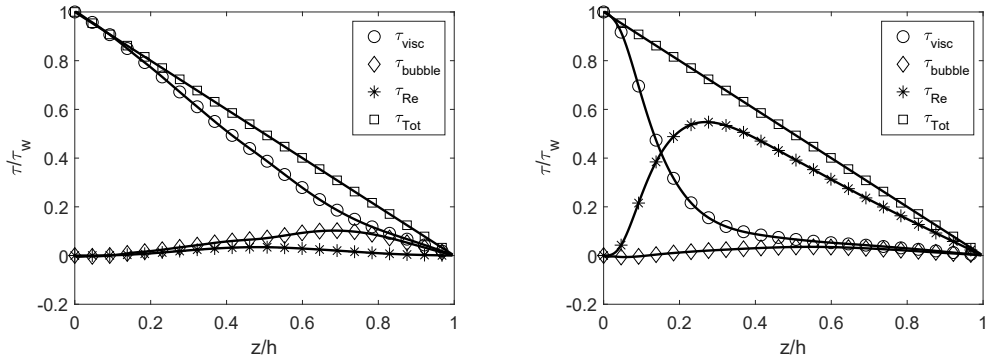

(a) $\tau(z)$ *at Re=700*

(b) $\tau(z)$ *at Re=1400*

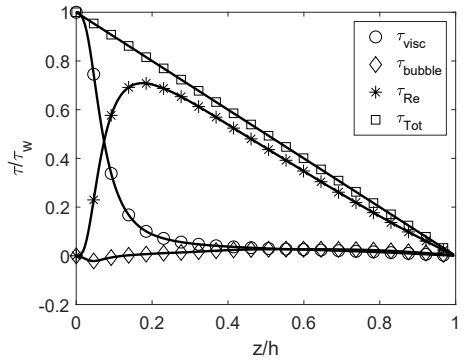

(c) $\tau(z)$ *at Re=2800*

Figure 3.26: Shear stress decomposition at $\Phi = 5\%$.

For what concerns the shear stresses, the increase of flow velocity causes the break up of the viscous fluid streamlines and produces a stochastic unsteady velocity field. The velocity oscillations transport momentum and this causes Reynolds stresses.

In these cases where $\Phi = 5\%$ the bubbles stresses are negligible, while in Figures 3.26b and 3.26c we observe that Reynolds stresses have arisen to almost the total amount of shear stress.

In short, in Figures 3.26b and 3.26c, the main source of shear stresses are Reynolds velocity fluctuations, hence we find that these cases are in fully turbulent regime and the presence of dispersed phase does not give rise to significant effects on the bulk flow.

3.3.2 $\Phi = 15\%$

In the first figure of this section, Figure 3.27, it is observed the same deviation from the common trend of the laminar case with $Re = 700$. Thus it is confirmed that the laminar case present a parabolic velocity profile along the width of the channel and a lower friction coefficient with respect to the turbulent cases.

In addition to that we witness an inversion in the trend along with the increase of percentage of dispersed phase: the cases with lower Reynolds number present a flatter velocity profile, while the one with larger Reynolds number present a more curved one. This is an inversion in the trend, since so far the literature and this work have enlightened that the velocity profile tend to be flatter at higher Reynolds number.
Anyway, as aforesaid at the beginning of Chapter 3, the outcomes of the simulations with $\Phi = 15\%$ are not completely reliable as they present a significant and peculiar deviation from the other data trends.

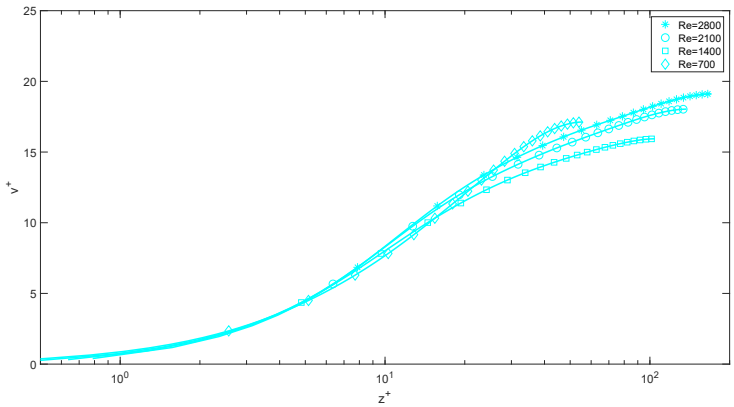

Figure 3.27: $v^+(z^+)$ at $\Phi = 15\%$.

In Figures 3.28b, 3.28c and 3.28d we observe the same trend for velocity oscillations as the previous cases.
Note that velocity fluctuations are present even in the laminar case, even they are very slight in comparison with the ones of the turbulent cases. This is due to the intrinsic instability of the flow, and to the presence of a dispersed phase, which accentuates these instabilities even at low Reynolds numbers.

We observe that the dispersed phase tend to migrate towards the centreline in the turbulent cases, even if this phenomena does not show a clear trend of direct or inverse proportionality with the Reynolds number. On the contrary the dispersed phase tend to accumulate the halves of the semi-channels in the laminar case.

In Figures 3.30a, 3.30b and 3.30c it is detected that the bubbles stresses have arisen with respect to Figures 3.26a, 3.26b and 3.26c of the case with $\Phi = 5\%$. Moreover Reynolds stresses are present in Figures 3.30b and 3.30c, corresponding to turbulent regimes with $Re = 1400$ and $Re = 2800$, and they overcome the bubbles stresses in the composition of the total shear stress

3.3.3 $\Phi = 25\%$

In this Section we will analyse the behaviour of the bulk flow with the maximum percentage of dispersed phase taken into account along this study. It is expected that the bubble stresses show the highest values between all the other cases, and that the presence

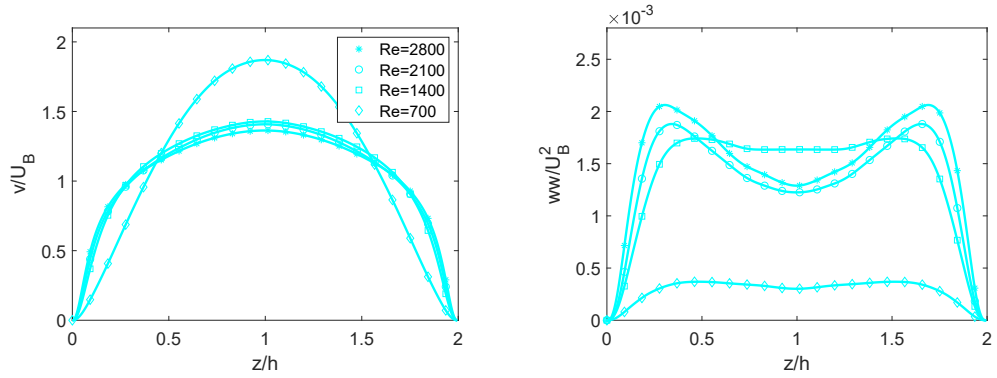

(a) $\frac{v(z)}{U_{bulk}}$ *at* $\Phi = 15\%$ (b) $\frac{w'w'(z)}{U^2_{bulk}}$ *at* $\Phi = 15\%$

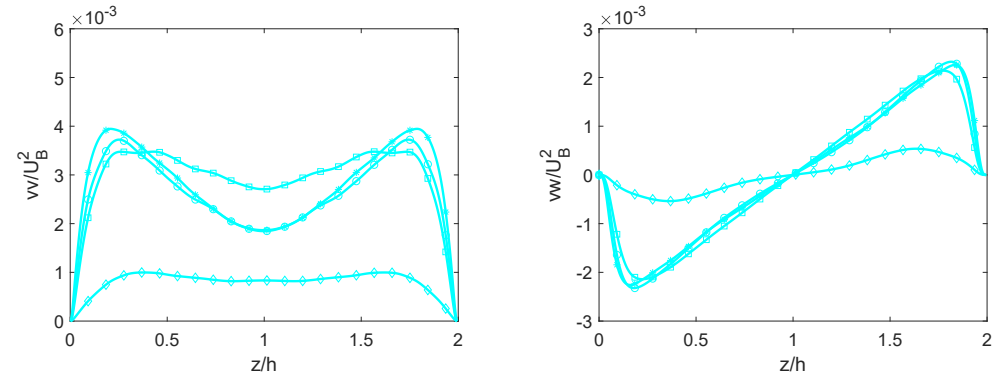

(c) $\frac{v'v'(z)}{U^2_{bulk}}$ *at* $\Phi = 15\%$ (d) $\frac{v'w'(z)}{U^2_{bulk}}$ *at* $\Phi = 15\%$

Figure 3.28: Velocity fluctuations at $\Phi = 15\%$.

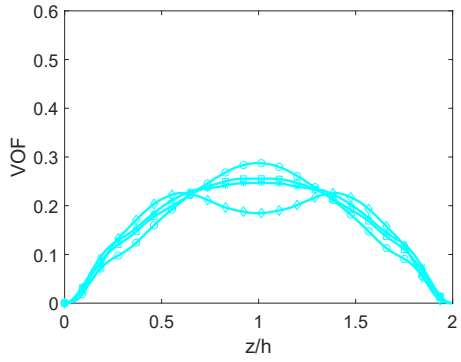

Figure 3.29: VOF at $\Phi = 15\%$.

of a large amount of dispersed phase in the bulk structure of the flow mitigates the velocity fluctuations even with fully developed turbulence.

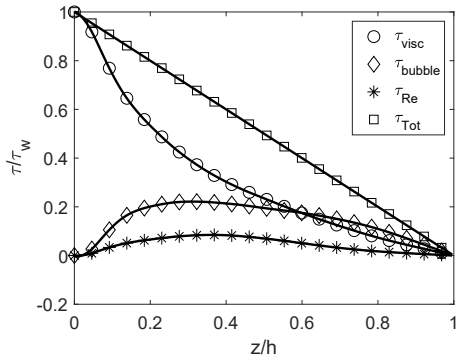

(a) $\tau(z)$ *at Re=700*

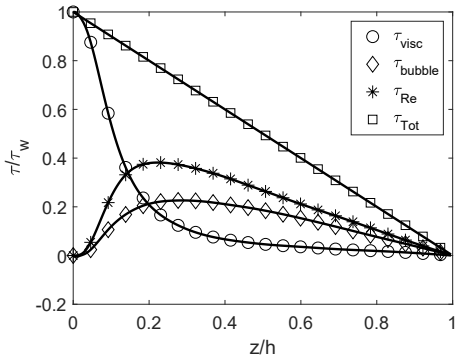

(b) $\tau(z)$ *at Re=1400*

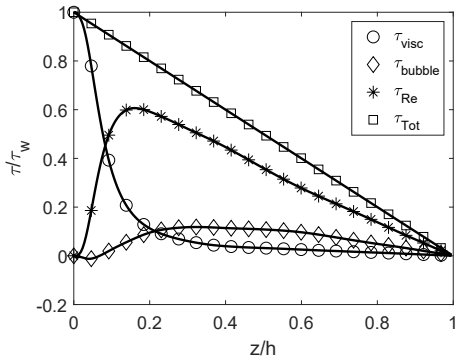

(c) $\tau(z)$ *at Re=2800*

Figure 3.30: Shear stress decomposition at $\Phi = 15\%$.

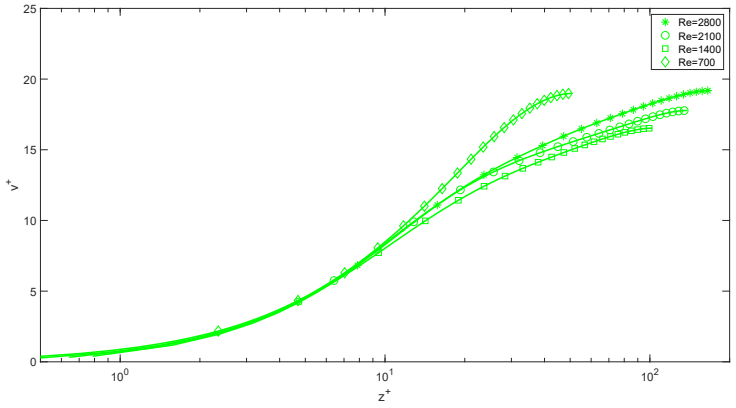

Figure 3.31: $v^+(z^+)$ at $\Phi = 25\%$.

In Figure 3.31 we observe, as already noticed in the previous sections, a parabolic velocity profile for the laminar case ($\diamond$) and flatter ones for the turbulent cases. In this graph the trend of proportionality between the velocity magnitude and the Reynolds number in turbulence recurs, after the scattered pattern of the case with $\Phi = 15\%$.

This phenomena is enlightened in Figure 3.32.

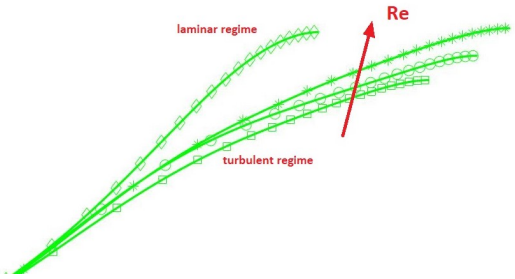

Figure 3.32: Magnification of the dimensionless velocity profile diagram. Here is enlightened the proportional dependency on the Reynolds number.

This trend is confirmed by the diagram of the dimensional velocity profile along the channel width, represented in Figure 3.33a.
In all the cases the velocity fluctuations in laminar regime are negligible in comparison to the ones of the turbulent case.

The velocity fluctuations along the y and z direction present the most elevated values so far and they respect the trend deduced from the previous experiments:

	Laminar	**Turbulent**
$\frac{v'v'}{w'w'}$	$\simeq 3.438$	$\simeq 1.886$

Notice that the velocity fluctuations in the flow at $Re = 700$ are due to unsteadiness of the emulsion flow even at Reynolds value under Re_{cr}.

Furthermore we observe that the diagrams in Figures 3.33c and 3.33b present two distinct peaks at $z \simeq \frac{1}{3}h$ and $z \simeq \frac{5}{3}h$. This phenomena is due to the fact that in high turbulence the combined action of lift-up of the mean profile, mean shear, and viscous diffusion give rise to small vortices, coaxial with the flow velocity, in the near wall region. The vortices are called *streaks* or *wall region streaks*. The pattern of streaks is dictated by these linear effects to a much greater extent than by the pattern of the wall-normal motions. Streaks are region of slow fluid flow and they are universal, they are always observed in near-wall turbulent flows and their characteristic dimensions are always the same if expressed in wall units and measured immediately at the wall: the length is about 1000 and the spanwise period about 100. Near-wall streaks are very important for

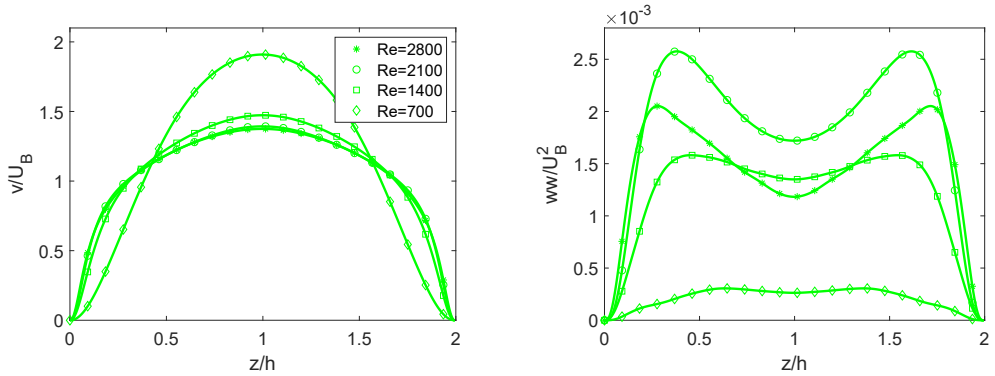

(a) $\frac{v(z)}{U_{bulk}}$ *at* $\Phi = 25\%$ (b) $\frac{w'w'(z)}{U^2_{bulk}}$ *at* $\Phi = 25\%$

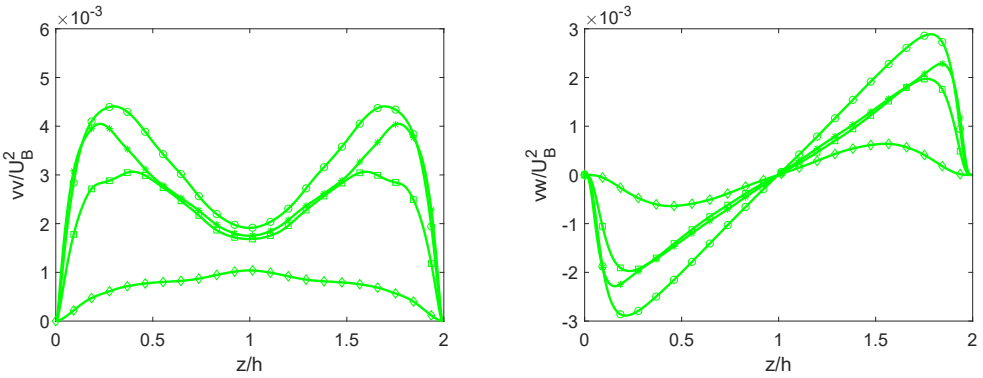

(c) $\frac{v'v'(z)}{U^2_{bulk}}$ *at* $\Phi = 25\%$ (d) $\frac{v'w'(z)}{U^2_{bulk}}$ *at* $\Phi = 25\%$

Figure 3.33: Velocity fluctuations at $\Phi = 25\%$.

drag reduction and turbulence control. Numerical experiments show that if streaks are somehow suppressed, the turbulence intensity is reduced significantly.

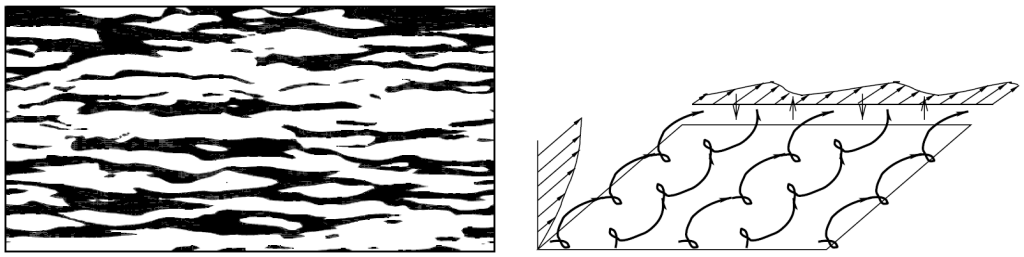

(a) *Streaks at* $y^+ = 5.6$ (b) *Wall region streaks streamlines*

Figure 3.34: On the right streaks in near-wall turbulent flow at $y^+ = 5.6$ from the wall and on the left the hypothetic mechanism of streak formation by longitudinal vortices. [CB05]

These region of slow fluid flow appear because there are wall-normal motions advecting the slow-moving near-wall fluid into the region away from the wall.
The phenomena of *streaks*, or *near wall streaks*, can be explained as follows:

Rows of vortices elongated in the direction of the mean flow and rotating in alternating directions capture the fluid and advect it from the wall and to the wall in alternating stripes. The fluid advected from the wall is moving slower than on average at this distance from the wall, while fluid advected to the wall is moving faster. This creates the wavy longitudinal velocity profile at a fixed distance from the wall shown in Figure 3.34b. The same vortices advect smoke if it is released from the wall thus creating streaks similar to Figure 3.34a.

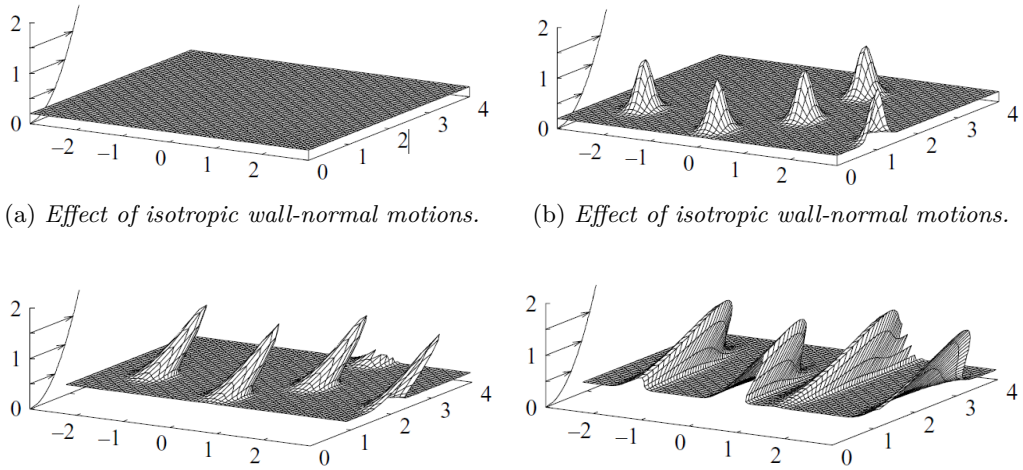

(a) *Effect of isotropic wall-normal motions.*

(b) *Effect of isotropic wall-normal motions.*

(c) *Effects of mean shear stress.*

(d) *Effects of diffusion.*

Figure 3.35: Mechanism of streak formation in near-wall turbulence. [CB05]

In the case of emulsion flows the wall region streaks causes elevate mixing ratio and momentum transport. The velocity fluctuations along the wall normal coordinate and the steep velocity gradient near the wall region causes the break up of bubbles and the migration of the dispersed phase towards the centreline, as we see in Figure 3.36.
For further informations on this subject see [CB05].

For what regards the shear stresses profiles we observe in Figure 3.37a that the largest component of shear stress in the flow is due to the viscosity action. Both Reynolds stresses and bubbles stresses are negligible and they have approximately the same magnitude order.

In Figure 3.37b, with $Re = 1400$, it is observed a great increase in both Reynolds and bubble stresses, that now form the hole amount of shear stresses. In this case we find the *inertial-shear thickening regime*, which is dominated by interaction between bubbles through momentum transfer and by velocity fluctuations due to turbulence arising.

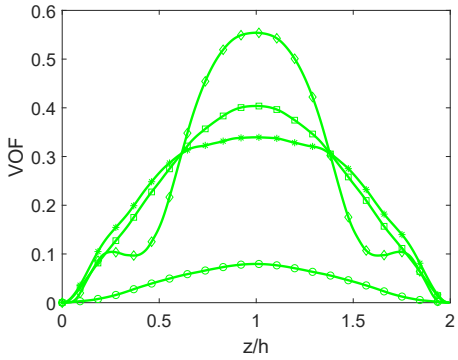

Figure 3.36: VOF at $\Phi = 25\%$.

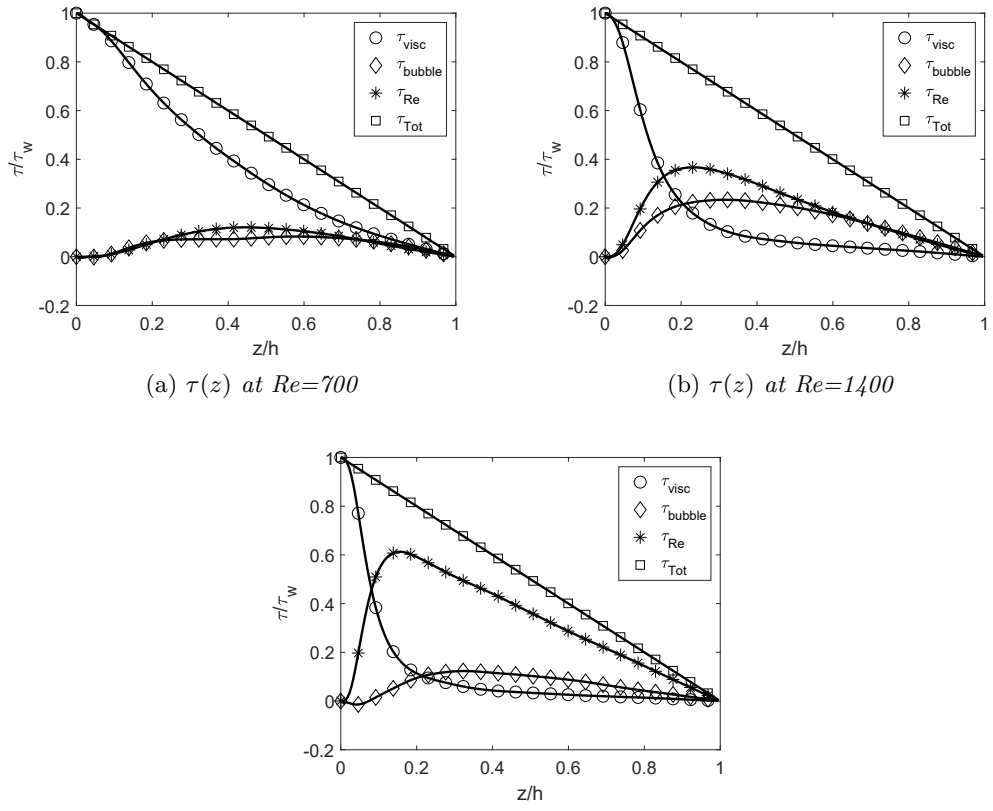

(a) $\tau(z)$ *at Re=700*

(b) $\tau(z)$ *at Re=1400*

(c) $\tau(z)$ *at Re=2800*

Figure 3.37: Shear stress decomposition at $\Phi = 25\%$.

Eventually, in Figure 3.37c, turbulence increases and Reynolds stresses arise to almost the entire amount of shear stress in the bulk flow. In this conditions we find again the

turbulent regime.

Summing up the outcomes of the Sec. 3.2 and 3.3 we can conclude that the presence of the second phase affects mainly the second *order statistics*, while the first *order statistics* remain essentially unvaried. In fact the first order statistics do not present any changes with respect to the variation of volume of dispersed phase. On the contrary second order statistics do.

For what concerns fluctuations in pressure and velocity, they present small shifts along with the variation of volume of dispersed phase.

Every numerical calculations shows that the viscous stresses are not dependent on the presence of a dispersed phase, and, as well known from the literature, their magnitude diminishes with the increase of Reynolds number.

3.4 Combined effects of Reynolds number and volume of dispersed phase

In this section we sum up the combined effect of variation of Re and variation of Φ through the use of diagrams and 3D maps.

In the first map we take into account the friction Reynolds number Re_τ, defined as:

$$Re_\tau = \frac{u_\tau \delta}{\nu} \tag{3.11}$$

where $u_\tau = \sqrt{\frac{\tau_w}{\rho}}$ is the *shear velocity* and δ is the thickness of the boundary layer. This quantity can be calculated, with some algebra, also as:

$$Re_\tau = \frac{u_\tau \delta}{\nu} = Re\frac{u_\tau}{U_b} \tag{3.12}$$

Since $U_b = 1$ in this case we obtain the friction Reynolds number simply by multiplying the bulk Reynolds number for the friction velocity:

$$Re_\tau = Reu_\tau \tag{3.13}$$

This parameter is important because, apart from defining the turbulence level of the flow, gives an indication of the drag coefficient of the flow in the channel by comparing the data from the computations with the analytical data for the same case with one phase flow we can discover if the drag coefficient has increased or decreased due to the presence of the dispersed phase.

The drag coefficient is defined as follows:

$$c_f = \frac{\tau_{wall}}{\frac{1}{2}\rho U_b^2} \tag{3.14}$$

Since the definition of friction velocity given in Section 3.2 we know that:

$$u_\tau = \sqrt{\frac{\tau_{wall}}{\rho}} \Longrightarrow \tau_{wall} = \rho u_\tau^2 \tag{3.15}$$

Substituting the definition in 3.15 it yields that:

$$c_f = \frac{\tau_{wall}}{\frac{1}{2}\rho U_b^2} = \frac{\rho u_\tau^2}{\frac{1}{2}\rho U_b^2} = 2\left(\frac{u_\tau}{U_b}\right)^2 = 2\left(\frac{\frac{u_\tau h}{\nu}}{\frac{U_b h}{\nu}}\right)^2 = 2\left(\frac{Re_\tau}{Re_b}\right)^2 \tag{3.16}$$

It is straightforward that there is a direct proportionality between c_f and Re_τ, in particular $c_f \propto Re_\tau^2$. Hence if the friction Reynolds number is higher in emulsion than in the single-phase flow this will result in a higher drag coefficient, and vice-versa.

The analytical formulas to compute Re_τ in both laminar and turbulent regime are:

Laminar regime $Re_\tau = \sqrt{3Re}$
Turbulent regime $Re_\tau = 0.09\,(2Re)^{0.88}$

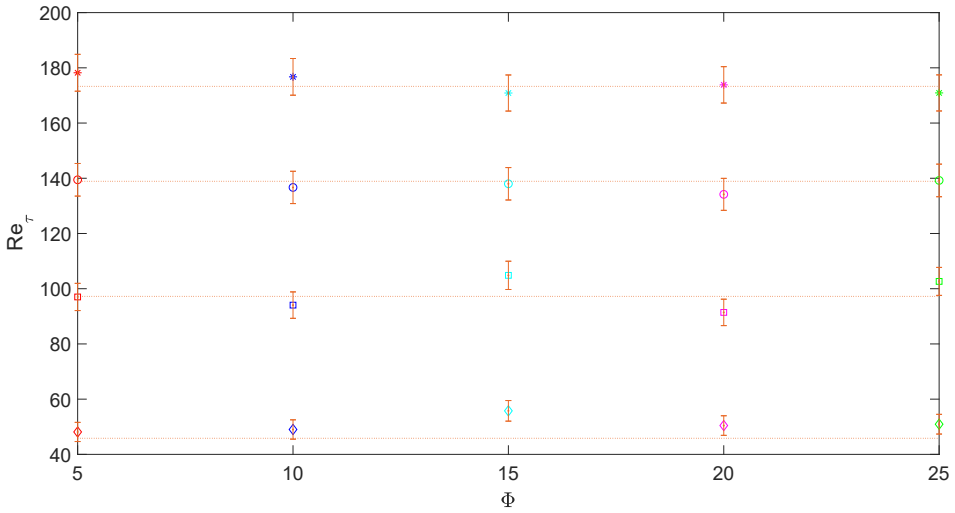

Figure 3.38: $Re_\tau(\Phi)$.

The comparison between the outcomes of the simulations and the analytical prediction is important in order to evaluate if the presence of the dispersed phase increases or deceases the drag coefficient.

In Figure 3.38 are reported the computed and the theoretical values of Re_τ for each case. The error bars are computed with the root mean square error of the time history of viscous wall stress.

$$\overline{\tau_w} = \frac{1}{\Delta t}\int_{t_0}^{t_f} \tau_w(t)dt \tag{3.17}$$

$$\varepsilon_{RMS} = \sqrt{\frac{1}{N}\sum_{i=1}^{N}\left(\tau_{w_i} - \overline{\tau_w}\right)^2} \tag{3.18}$$

As expected, the ε_{RMS} present higher values for Higher Reynolds numbers, due to the more elevated range of velocity fluctuations in cases with higher Reynolds number.

The first yellow dotted line, starting from the bottom, represent the theoretical value of Re_τ for $Re = 700$, hence in laminar regime.

Furthermore we can plot the shift of Δc_f between the various cases on a map with independent coordinates Re and Φ, thus obtaining:

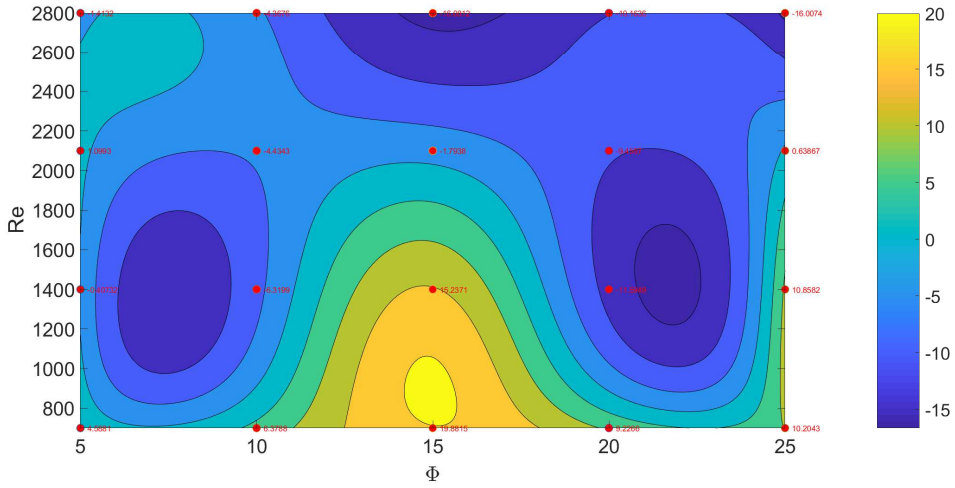

Figure 3.39: In this map the shift of c_f between the analytical one-phase cases and the data of the simulations for emulsion flows.

We can observe that for every percentage of dispersed phase the value of Re_τ is higher than the theoretical value. This results in a higher drag coefficient, hence we can state that *the presence of a dispersed phase increases the drag in laminar regime*. In Figure 3.39 it is shown that the increase of c_f and hence a larger drag force along the channel is viewed for mainly for high Φ percentages and low Reynolds number. It is important to observe that the map in Figure 3.39 resembles the one in Figure 3.43b, hence the arise of shear stresses due to the interaction between surface tension could be the major mechanism acting to increase the drag coefficient in multi-phase flows.

For what concerns the turbulent regime, the successive three dotted lines represent the theoretical Re_τ computed with the experimental formula, respectively with Re = 1400,2100,2800, going from the bottom to the top. The case with $Re = 1400$ present overall values smaller than the theoretical forecast, yielding in a reduction in drag.
On the contrary the cases with $Re = 2100$ and $Re = 2800$ present an increase of the Re_τ values computed by the simulations in comparison with the analytical data and this clearly indicates an increment in drag.
From the outcomes of the simulations it infers that the Reynolds number Re_τ remains constant with respect to the variation of second phase percentage Φ.

Eventually we can sum up the outcomes of the diagram in Figure 3.38 with the following statements:

- The drag in multiphase flows increases with respect to single-phase flows for high concentration of dispersed phase and low Reynolds numbers;

- The drag in multiphase flows decreases with respect to single-phase flows for low concentration of dispersed phase and high Reynolds numbers;
- In laminar flows the presence of a dispersed phase seems to increase the drag coefficient since it causes more turbulent-like fluctuations in the flow, while in turbulent regime the presence of a dispersed phase mitigates the turbulent fluctuations and causes the decrease of the drag coefficient.

In Figure 3.40 these same results are plotted on a 3D map that allow us to analyse the effects of Re and of Φ separately.

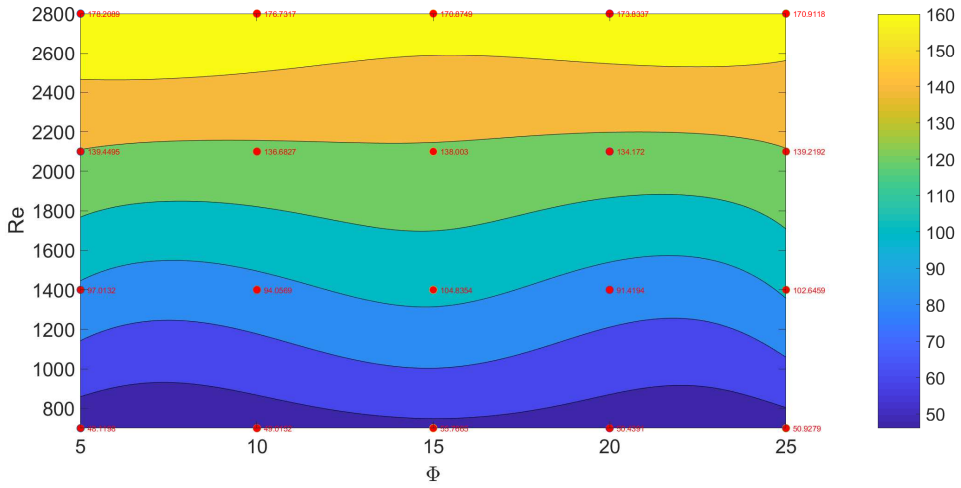

Figure 3.40: $Re_\tau(Re, \Phi)$.

We see from the map the direct proportionality between Re and Re_τ. The percentage of dispersed phase shows no particular influence on the friction Reynolds number Re_τ.

In Figure 3.41 is reported the trend of the magnitude of velocity fluctuations along the wall-normal coordinate $w'w'$. As expected the velocity fluctuations increases at higher Reynolds number, in fact in Figure 3.41 the highest iso-surfaces are located in the upper part of the diagram.

In addition to that, they show a peak for the case with $Re = 1400$ and $\Phi = 5\%$.

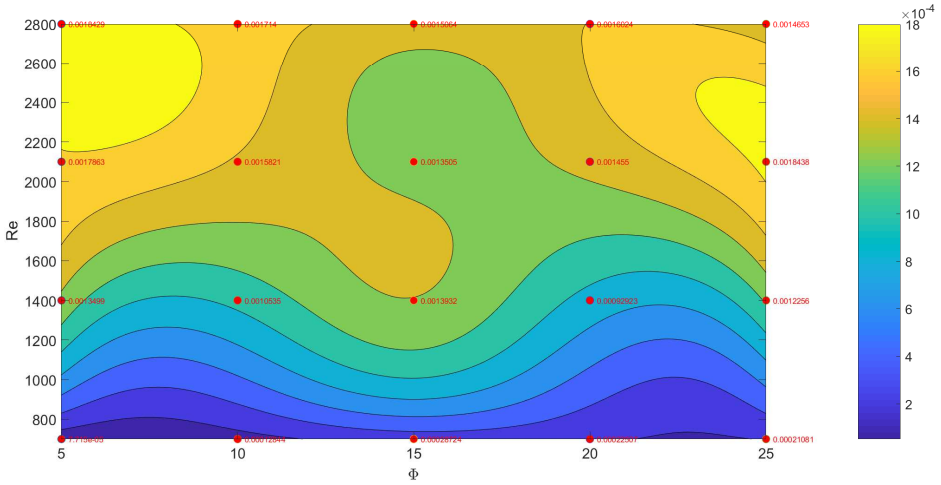

Figure 3.41: $\overline{w'w'}(Re, \Phi)$.

The shear stresses on the wall present the higher value for the case with $Re = 700$ and $\Phi = 15\%$ as reported in Figure 3.42, while they tend to decrease at higher Reynolds number.

From Figure 3.42 we deduce that the wall shear stress remain constant with respect to the variation of Φ, while it decreases proportionally to the Reynolds number. This could be explained with the fact that the bubbles tend to migrate towards the centreline and thus their effect is more appreciable in velocity fluctuations across the width of the channel, while it is null on the quantities measured on the walls surface.

Notice that Figures 3.43c and 3.41 are very similar since both of them represents velocity fluctuations, respectively $\tau_{Re} = \mu\overline{v'w'}$ and $\overline{w'w'}$.

In Figure 3.43a it is shown, as expected, a relation of inverse proportionality between viscous stresses and Reynolds number. In fact viscosity acts as a counterbalance of the turbulent velocity fluctuations. For higher Reynolds number the flow undergoes larger velocity fluctuations and hence the majority of the shear stresses is then composed by Reynolds stresses, while viscous stresses gradually decreases. As a matter of fact we have to state that viscosity plays a more important role in the near wall region and it progressively declines going towards the centreline of the channel.

On the contrary bubble stresses and Reynolds stresses arise the further we move from the wall surfaces towards the centreline, reaching two distinct peaks at $z = \frac{l}{2}$ and $z = \frac{3}{2}l$. Eventually they end up at null value at the centreline of the channel.

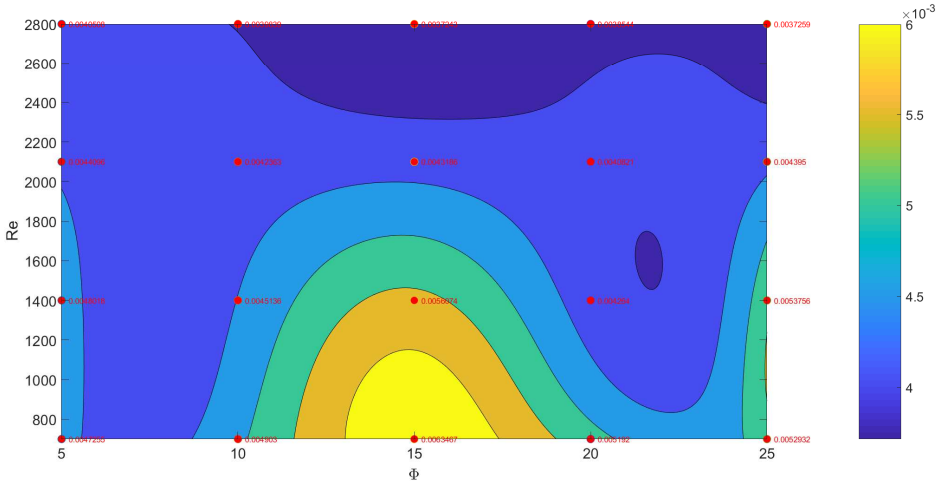

Figure 3.42: $\tau_{wall}(Re, \Phi)$. In this diagram is shown the total amount of stress acting on the wall due to the flow.

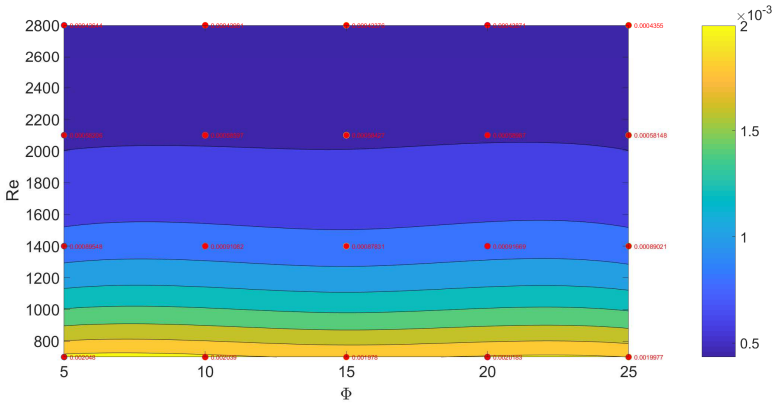

(a) $\tau_{\mu}(Re, \Phi)$

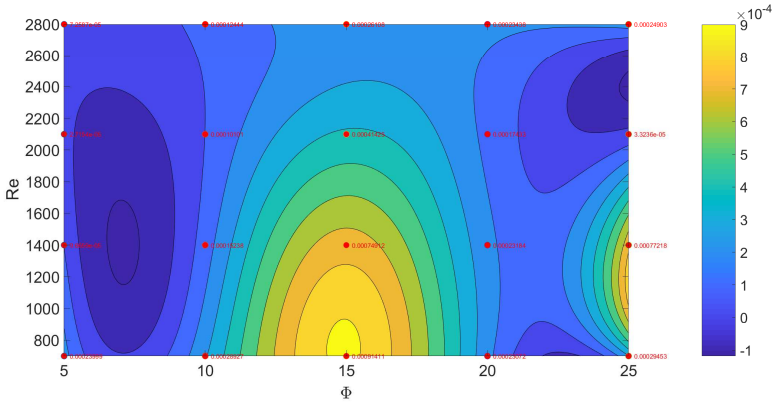

(b) $\tau_{bubble}(Re, \Phi)$

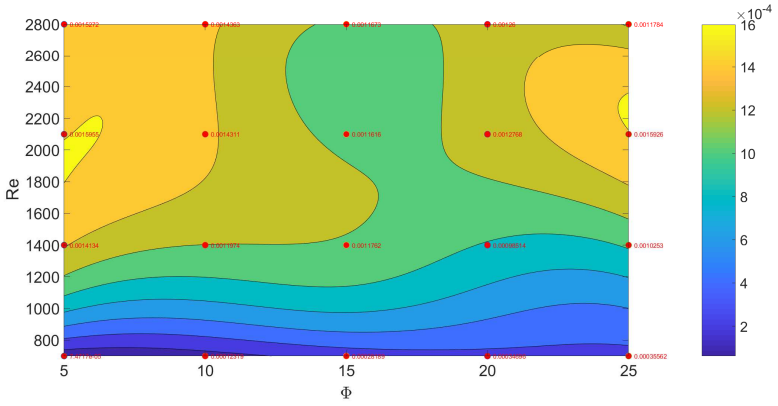

(c) $\tau_{Re}(Re, \Phi)$

Figure 3.43: 3D maps for shear stresses in the bulk flow.

Figure 3.43b shows a peaks in τ_{bubble} value in the middle of the map, for $\Phi = 15\%$ an low Reynolds numbers. Then bubbles stresses decrease going towards more turbulent regimes and going towards higher Φ values, and eventually they undergo another rise at the maximum Φ value, that is to say $\Phi = 25\%$.

We can define this area of the flow field in which one stress mechanism prevails on the other two by comparing between themselves the 3D maps. The areas in which $\tau_{bubblesprevail}$ are into *inertial shear-thickening* regime, areas in which τ_μ are dominant are in the *laminar* regime and where τ_{Re} are dominant are in *turbulent* regime.

To do so we have overlapped the 3D maps representing the stresses, τ_{bubble}, τ_{Re} and τ_μ, in Matlab and we have evaluated where one type of stress prevail on the others, as shown in Figure 3.44.

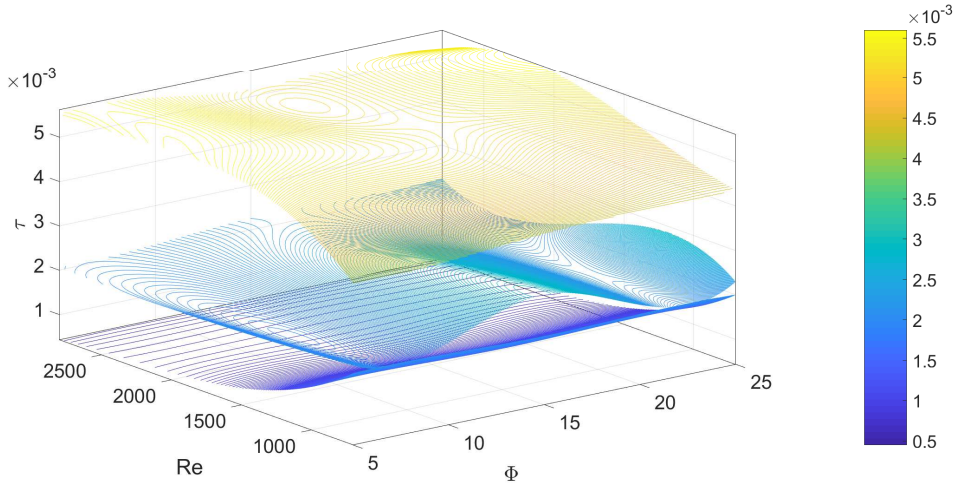

Figure 3.44: Interpolation of τ_{bubble}, τ_{Re} and τ_μ 3D maps. In yellow are represented τ_{Re} with a 0.004 offset, in cyan are represented τ_{bubble} with a 0.002 offset and in blue are represented τ_μ with no offset.

Eventually we have obtained the map shown in Figure 3.45, where the three regime are separated by the red lines.

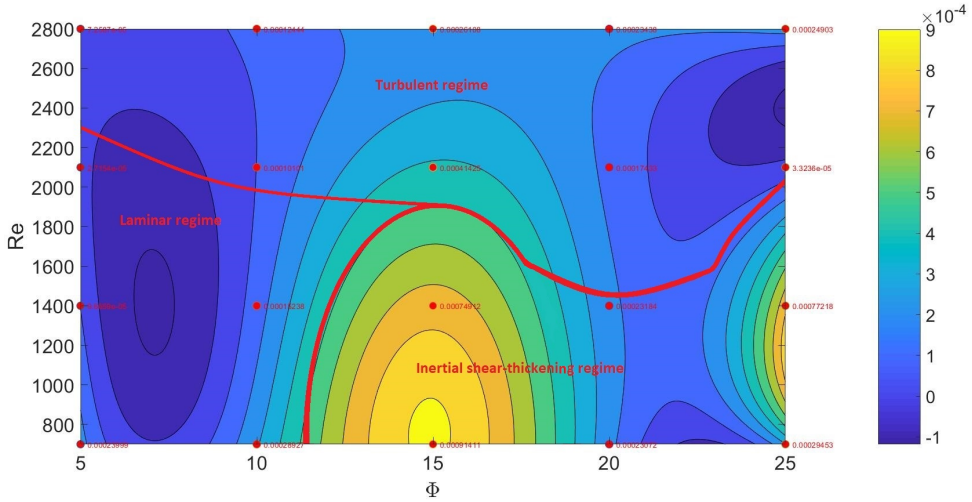

Figure 3.45: On this map, similar to the one in Figure 3.43b, are reported the three regimes individuated by this study.

The laminar region is located at the left end side, for low Reynolds numbers, where both velocity fluctuations and interaction between surface tension of the bubbles are negligible. On the top of the map is located the turbulent region, where the main source of shear stress are Reynolds velocity fluctuations for turbulent flows. Note that along the course of this study Reynolds number has been calculated on the half of the channel width $Re = \frac{\rho V_{bulk} h}{\mu}$. Hence the Reynolds number calculated using the full width of the channel would have been double the value of the ones in the diagram, with the transition to the turbulent regime occurring for $Re \simeq 5000$. This value is similar to the critical value of Reynolds number for transition between laminar and turbulent regime in plane channel flows, for instance see [Zha17].
Eventually we have extrapolated an area of the map where the majority of shear stress in the flow was produced by interaction between surface tension of adjacent bubbles. In this area occurs the *inertial shear-thickening regime*.

Chapter 4

Conclusions and way forward

4.1 Conclusions

To sum up the outcomes of the present study we can state that the presence of a dispersed phase modifies the bulk flow structure in the following way:

- The bubbles of dispersed phase tend to migrate towards the centreline of the channel ate steady-state flows due to the larger amount of stress in the near wall regions that contributes to the bubbles break up. This trend is emphasized by the increase of volume of second phase in the emulsion and it is decreased by the rise of Reynolds number;
- In fully developed turbulence, for $Re_{l_z/2} > 2000$ the presence of dispersed phase does not affect the bulk structure of the flow and does not modify significantly the drag produced by the flow in the channel;
- At low Reynolds number and for sufficiently high percentage of dispersed phase a new kind of shear stress arises to give a significant contribution to the total shear stress and this new component is caused by the transfer of momentum due to interaction between adjacent bubbles. Regimes in which this component arise to be a significant part of the total shear stress are said *inertial shear-thickening regimes*;
- In general the presence of a dispersed phase increases the drag coefficient at low Reynolds number and decreases it at elevate Reynolds numbers. This is due to the fact that in laminar regime the presence a dispersed phase accentuates the small velocity fluctuations present, thus resulting in a higher drag coefficient. On the contrary in fully-developed turbulence the presence of a dispersed phase mitigates the turbulent velocity fluctuations and hence reduces the drag coefficient;
- The combined action of turbulence and presence of a dispersed phase tend to localize velocity fluctuations in confined peaks at $z = \frac{1}{3}h$ and $z = \frac{5}{3}h$ for $Re =$ 700,1400,2100,2800. This phenomena is bound to external scales and not to wall scales.

For clarity sake here are here reported the shear stress profile for the three regimes.

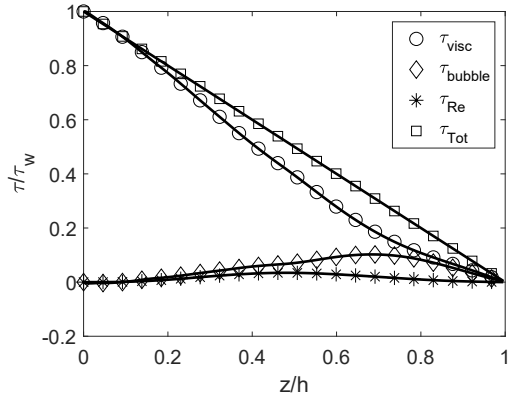

(a) $\tau(z)$

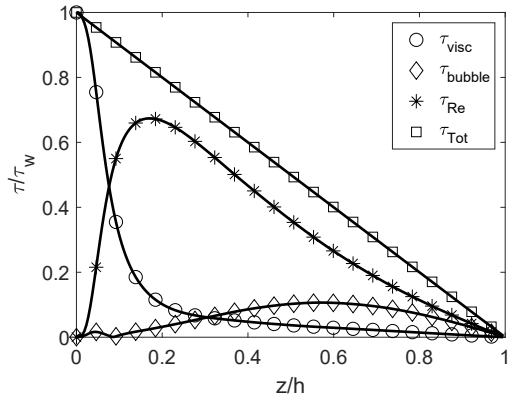

(b) $\tau(z)$

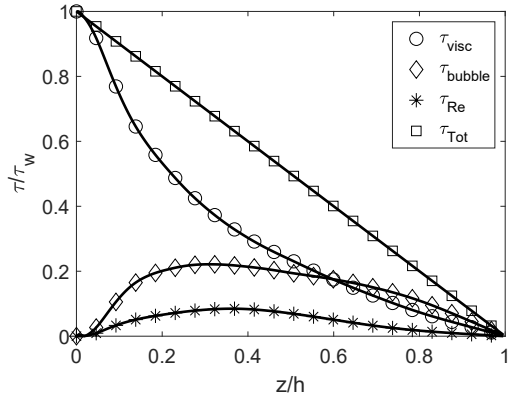

(c) $\tau(z)$

Figure 4.1: Shear stress profile for the three regimes. In Figure 4.1a we have a laminar stress profile for $Re = 700$ and $\Phi = 5\%$. In Figure 4.1b we observe a turbulent one for $Re = 2800$ and $\Phi = 20\%$ and eventually, in Figure 4.1c we have a inertial stress profile for the case with $Re = 700$ and $\Phi = 15\%$.

In Figure 4.1a is presented the shear stress profile for the case with $Re = 700$ and $\Phi = 5\%$. This case is, as well known,in the laminar regime and hence we observe that the major part of the shear stress is due to viscosity. Both Reynolds and bubbles stresses appears to be negligible in this regime.

In Figure 4.1b is plotted the shear stress profile for the case with $Re = 2800$ and $\Phi = 20\%$. We can deduce how the transitions to fully developed turbulence has occurred since we have a Reynolds number on the total width of the channel equal to 5600, that is similar to the critical Reynolds value for plane channel flows, $Re_{cr} = 5700$. We observe that, even is the percentage of dispersed phase is elevate, the bubble stresses are negligible in comparison with Reynolds stresses. Hence we state that the presence of a dispersed phase in emulsion flows does not affect the flow from a rheological point of view.

In the last figure, Figure 4.1c, we observe that the bubble stresses, even though they are lower than viscous ones, are considerably higher than in other cases, and overcomes the Reynolds stresses. This case with $Re = 700$ and $\Phi = 15\%$ is comprehended in the *inertial shear-thickening regime*. We can assert that the presence of a dispersed phase mitigates the velocity fluctuations and hence the Reynolds stresses, which appear to be smaller than Reynolds stresses in the laminar case with the same Reynolds number.

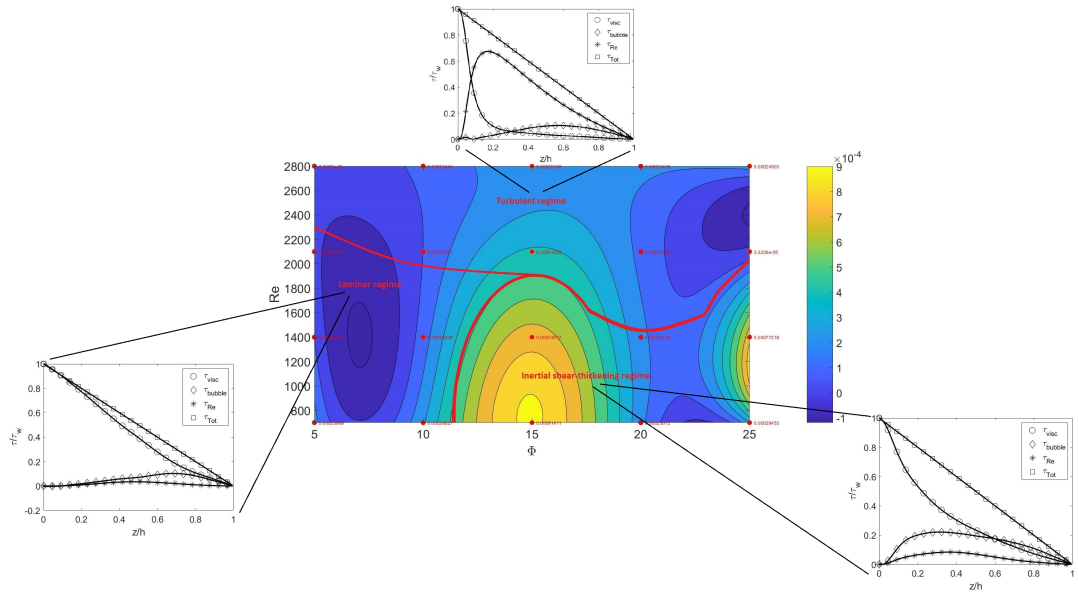

Figure 4.2: 3D map of τ_{bubble} with relative stress profile for each regime.

Finally it is possible to define a range for the two parameters for each regime, as it was hoped at the beginning of this study.

	Φ	**Re**
Laminar regime	$0\% \div 12\%$	$0 \div 2200$
Turbulent regime	$0 \div \infty$	> 2200
Inertial shear-thickening regime	$12\% \div 25\%$	$0 \div 2200$

Table 4.1: Overview on the ranges for the parameter Re and Φ in every regime.

4.2 Comparison with previous results

In this Section we confront the results of the present study with the outcome of the study conducted by Lashgari, Picano, Breugem and Brandt at the Linné Flow Centre on granular flows. For further details see the full article [Las+16].

Note that the data of the article [Las+16] are calculated on a range of Φ going from 0 % to 30 %, hence slightly bigger than the range of our study $5\% \leq \Phi \leq 25\%$, and on a range of Reynolds number going from 500 till 5000. This could appear as a much larger range of data, but actually this quantity represents the Reynolds number calculated on the full channel, while in the represent study the Reynolds number on half channel has been used.
To summarize this issue, the outcomes of the two studies are strongly comparable!

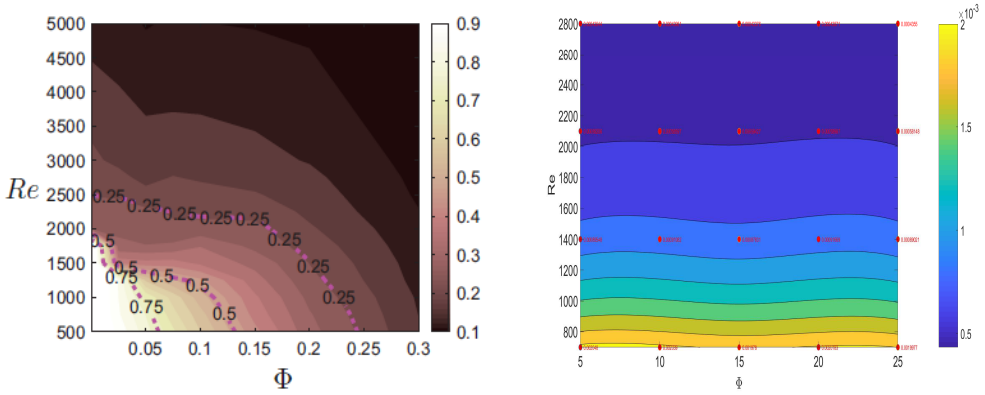

(a) *Viscous stresses according to [Las+16]*

(b) *Viscous stresses according to our computations*

Figure 4.3: Comparison of τ_μ between the two studies.

We can see that viscous stresses prevail at low Reynolds numbers, but in granular flows we observe that these stresses undergo a variation even along the variation of Φ, decreasing with the increase of dispersed phase, while viscous stresses in emulsion flows show no variation with the dispersed phase.

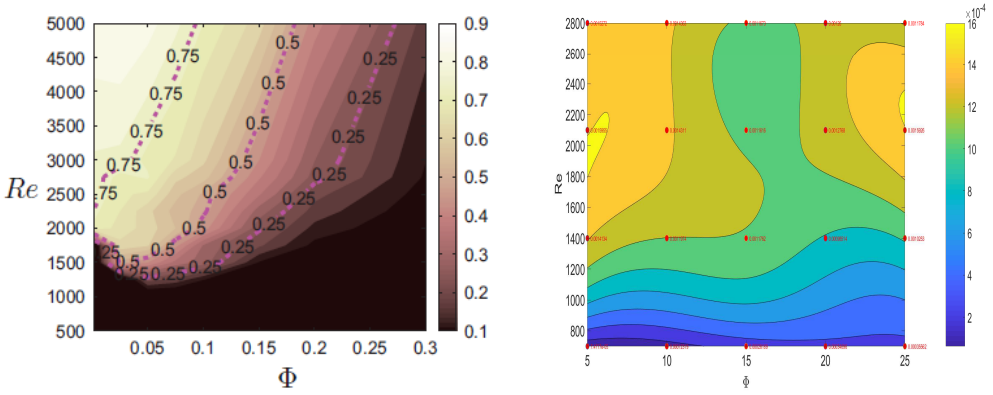

(a) *Reynolds stresses according to [Las+16]*

(b) *Reynolds stresses according to our computations*

Figure 4.4: Comparison of τ_{Re} between the two studies.

Even in Figures 4.4a and 4.4b we observe a even more similar pattern in the distribution of τ_{Re} along the various cases. The only exception is represented by a stripe of low τ_{Re} which runs across the cases with $\Phi = 15\%$ in the emulsion flows and is absent in the granular flow.

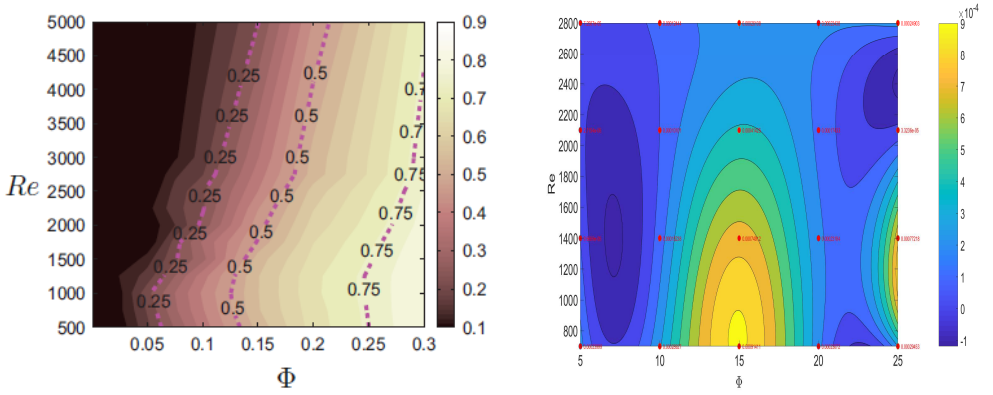

(a) $\tau_{granular}$ *according to [Las+16]* (b) τ_{bubble} *according to our computations*

Figure 4.5: Comparison of τ_{bubble} and $\tau_{granular}$ between the two studies.

In Figures 4.5a and 4.5b is reported the trend of the bubbles stresses along the variation of Re and Φ. Also in this case the outcomes are strongly comparable and they present, in general, an increase going towards denser regimes. In the emulsion case we observe a decrease in the magnitude of bubble stresses along the cases with $\Phi = 20\%$ for every Reynolds number.

Eventually we have to compare the map in which the transition between the three regimes is enlightened.

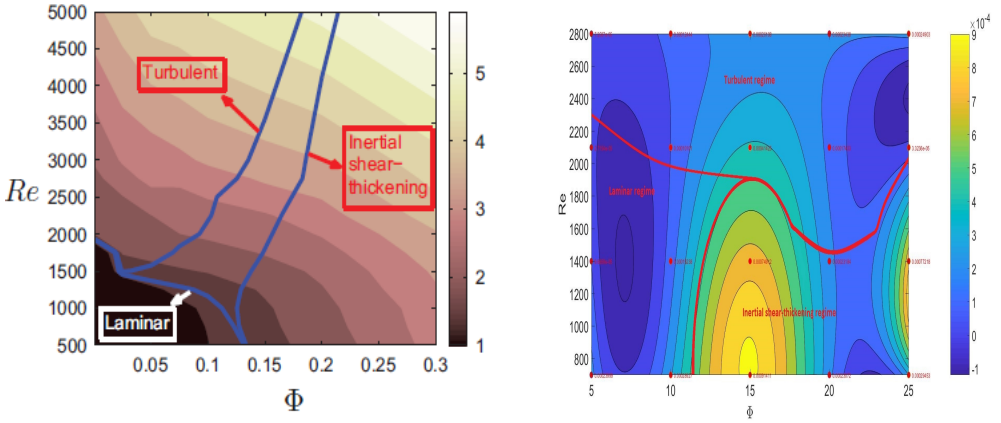

(a) $\tau_{granular}$ *according to [Las+16]* (b) τ_{bubble} *according to our computations*

Figure 4.6: Comparison of τ_{bubble} and $\tau_{granular}$ between the two studies with the transitions markers between regimes.

The most important difference between the diagrams is that in Figure 4.6a it is enlightened that the flow goes more and more into the shear-thickening regime as the percentage of granular phase increases, up to the right upper corner which presents the maximum of the $\tau_{granular}$. On Figure 4.6b, on the contrary, in the right upper corner we observe a decrease of the contribution of surface tension to the total amount of stress and an increase in Reynolds fluctuations contribution, indicating that in this corner the flow undergoes turbulent regime.

Furthermore the domain of the laminar regime is more restricted in the granular flow in comparison with the emulsion flow, since it ranges from $Re = 500(Re_{l_z/2} = 250)$ till $Re = 2000(Re_{l_z/2} = 1000)$ in Figure 4.6a, and it goes from $Re_{l_z/2} = 700$ till $Re_{l_z/2} = 2200$ in Figure 4.6b. In both cases the range of Φ for which the laminar regime is experimented is approximately the same, $\Phi \leq 12\%$.

4.3 Future studies

There are some areas in which detail study is required since the area of study of turbulence in emulsion flows is unexplored.

For what concerns the rheology of multi-phase flows there is room for further investigations performing simulations with different Reynolds number and dispersed phase percentages. For instance some simulations with $\Phi > 25\%$ could be performed in order to explore the area of the map 3.45 beyond the right border and hence going further into the inertial shear-thickening regime.

Another interesting area of investigation is exploring the effect of the Capillary number variation on the mean bulk flow. As we stated previously, the Capillary number affects the break-up mechanism of the bubbles, since this parameter represents the relative effect of viscous drag forces versus surface tension forces acting across an interface between two phases.

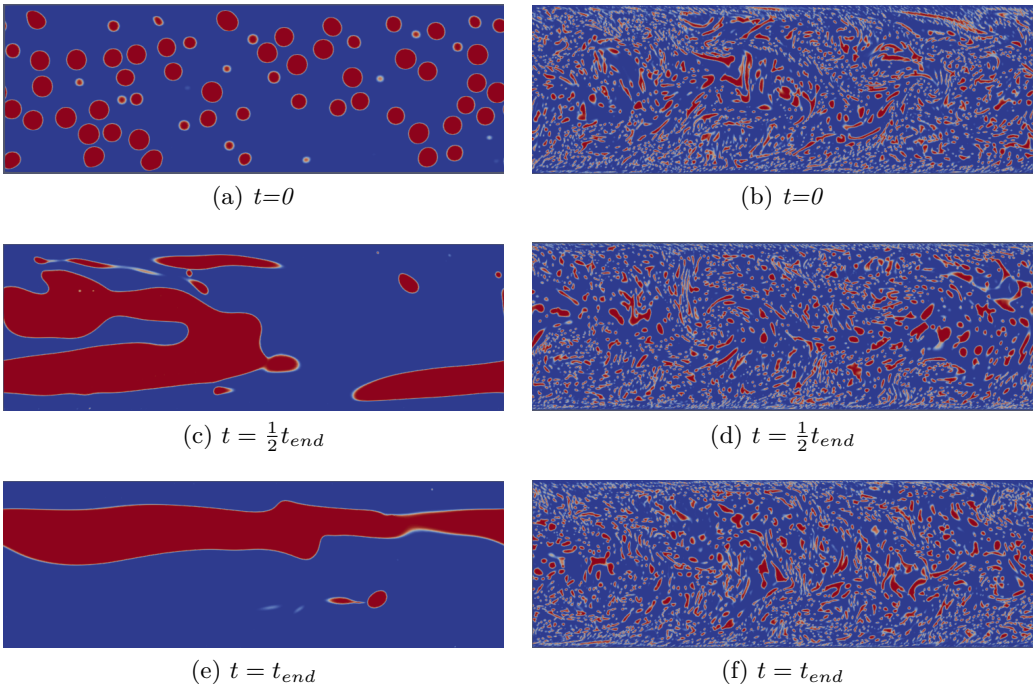

(a) t=0 (b) t=0

(c) $t = \frac{1}{2}t_{end}$ (d) $t = \frac{1}{2}t_{end}$

(e) $t = t_{end}$ (f) $t = t_{end}$

Figure 4.7: VOF distribution in the cases with Ca = 00.00175, on the left, and in the case with $Ca = 0.0000175$, on the right for $Re = 2800$ and $\Phi = 20\%$.

As clearly visible even from this coarse example, the Capillary number affects the way the bubbles distribute within the boundaries of the channel, and, with the time advancement, it affects event the mechanism in which the bubbles merge. Already from this primitive simulations it is evident that for too low Capillary number the bubbles cannot merge even at steady-state point, striving to maintain almost spheroidal bubbles.

Furthermore, an interesting aspect of turbulent multi-phase flows to be studied is the heat transmission between an hot wall and the flow. This phenomena has countless application in the field of industrial processes, such as the cooking process in the food industry, and mechanical equipment, such as heat exchangers and cavitating propellers. Some aspects of this field of study have already been explored throughout this study, for instance Appendix B reports the discretization of the heat equation in the case of numerical codes, ad Appendix C reports the outcomes of the heat equation implemented on an elementary case of study. Both appendices describes the results of the implementation of the heat transmission equation in the code already used for analysing the rheology of the emulsion flow. The code with the implementation of the modifies could be used to perform computation of more complex cases such as the ones studied in the present document, with the ground-breaking addition of heat transmission across the channel. In this way we could discover how the presence of a dispersed phases affects the heat transmission besides the shear stresses structure.

Appendices

Appendix A

Boundary conditions

In general boundary conditions allow to suppress the inherent degree of freedom present in any set of differential equations. It is known form mathematical analysis that the solution to a differential equation is a family of primitives, but the solution to a physical problem that involves differential equations must be unique. Hence the boundary condition provide the necessary bond to select one solution out of the family of primitives.

Boundary conditions can be of *Dirichlet* [1] or of *Neumann*[2] type. The first ones are implemented by imposing the direct value of a prescribed physical quantity on the domain boundary, while Von Neumann ones are implemented by assigning the value of the first derivative for a chosen physical quantity.

1. **Dirichlet boundary conditions**

$$\begin{cases} \Phi \mid_0 = \Phi_L \\ \Phi \mid_N = \Phi_R \end{cases} \tag{A.1}$$

2. **Von Neumann boundary conditions**

$$\begin{cases} \left(\frac{\partial \Phi}{\partial x}\right) \mid_0 = k_L \\ \left(\frac{\partial \Phi}{\partial x}\right) \mid_N = k_R \end{cases} \tag{A.2}$$

Note that the boundary conditions of Neumann type cannot be imposed on both ends of the physic domain for the same physical quantity.

Along our study we have implemented Dirichlet type boundary conditions for what concerns the axial and the transverse velocity velocity u and v (no-slip condition) and

[1] *Peter Gustav Lejeune Dirichlet* (Düren, 13 February 1805 - Gottingen, 5 May 1859), was a German mathematician, whose major contribute to maths has been the formal definition of function.

[2] *Carl Gottfried Neumann* (Königsberg, 7 May 1832 - Leipzig, 27 March 1925) was a German mathematician, not to be confused with the more famous John von Neumann, Hungarian-American mathematician, physicist and computer scientist.

Neumann type boundary conditions for the pressure on the physical walls. Along the virtual boundaries periodical boundary conditions are imposed. [3]

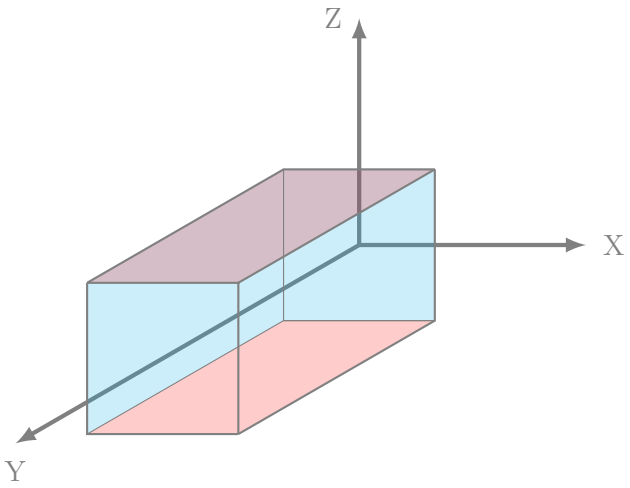

Figure A.1: Boundary conditions imposed on the domain of study. The red walls are the physical wall on which the no-slip and the no-penetration conditions are implemented, while the blue walls are the virtual boundaries of the computational domain on which periodical conditions are applied.

In our study case we have implemented boundary conditions on the following physical quantities: velocity components along the three directions, second phase percentage and pressure.

A.1 Velocity

To implement Dirichlet boundary condition on physical wall we adopted the following method. We implemented two concatenated loops that covered all the cells along the x and y directions for $z = -\frac{l}{2}$ and for $z = +\frac{l}{2}$, that is to say for the lower and upper physical walls, and for every cell the following condition is assigned:

$$\begin{aligned} &\cdot\, u(i,j,0) + u(i,j,1) = 2K_x \\ &\cdot\, v(i,j,0) + v(i,j,1) = 2K_y \\ &\cdot\, w(i,j,0) + w(i,j,1) = 2K_z \end{aligned} \tag{A.3}$$

[3] Along the course of the present appendix we will report the exact lines present in the code, respecting the notation used in Fortran. *kl* is the index of the cell under the upper wall, *kmax* is the index of the cell above the upper wall.

For what concerns the axial and transverse components of velocity u and v we have the *no-slip condition* hence the value of K_x and K_y is 0. For the wall-normal velocity component w we have the *no-penetration condition*. Thus it yields:

- **Lower wall**

$$\begin{aligned} &\cdot\, u(i,j,0) = -u(i,j,1) \\ &\cdot\, v(i,j,0) = -v(i,j,1) \\ &\cdot\, w(i,j,0) = 0 \\ &\cdot\, w(i,j,1) = 0 \end{aligned} \tag{A.4}$$

- **Upper wall**

$$\begin{aligned} &\cdot\, u(i,j,kl) = -u(i,j,kmax) \\ &\cdot\, v(i,j,kl) = -v(i,j,kmax) \\ &\cdot\, w(i,j,kl) = 0 \\ &\cdot\, w(i,j,kmax) = 0 \end{aligned} \tag{A.5}$$

- **Periodical conditions along y direction**

$$\begin{aligned} &\cdot\, u(i,0,k) = u(i,jmax,k) \\ &\cdot\, v(i,0,k) = v(i,jmax,k) \\ &\cdot\, w(i,0,k) = w(i,jmax,k) \\ &\cdot\, p(i,0,k) = p(i,jmax,k) \end{aligned} \tag{A.6}$$

- **Periodical conditions along x direction**

$$\begin{aligned} &\cdot\, u(0,j,k) = u(imax,j,k) \\ &\cdot\, v(0,j,k) = v(imax,j,k) \\ &\cdot\, w(0,j,k) = w(imax,j,k) \\ &\cdot\, p(0,j,k) = p(imax,j,k) \end{aligned} \tag{A.7}$$

A.2 Pressure

For the pressure we have implemented Neumann type boundary conditions: the first derivative of pressure along the wall-normal coordinate is assumed to be equal to 0. In addition to this we have implemented the same periodical boundary conditions on the virtual boundaries of the computational domain.

- **Lower wall**

$$\cdot\, p(i,j,0) = p(i,j,1) \tag{A.8}$$

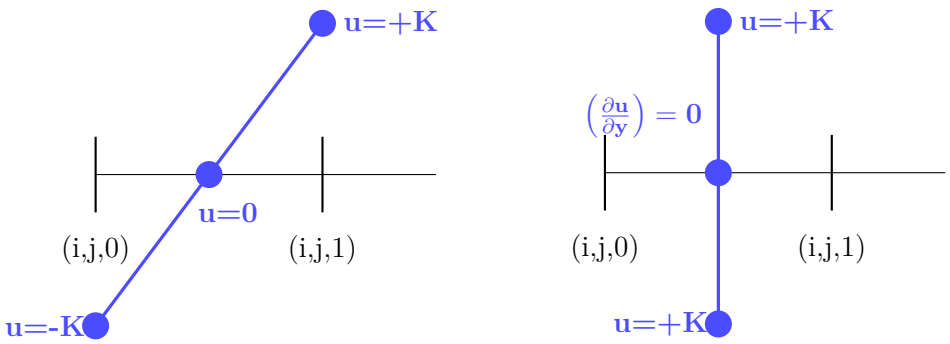

(a) *Dirichlet boundary conditions.* (b) *Neumann boundary conditions.*

Figure A.2: Comparison between Dirichlet and Neumann boundary conditions as implemented in the code.

- **Upper wall**

$$\cdot\, p(i,j,kl) = p(i,j,kmax) \tag{A.9}$$

- **Periodical conditions along y direction**

$$\cdot\, p(i,0,k) = p(i,jmax,k) \tag{A.10}$$

- **Periodical conditions along x direction**

$$\cdot\, p(0,j,k) = p(imax,j,k) \tag{A.11}$$

A.3 VOF

Another boundary condition is applied for what concerns the dispersed second phase, that is to say the bubbles in the mean flow. The physical behaviour of the bubbles that touch the physical walls can assume two different trends: the bubbles remain attached to the physical wall when they touch it, or the bubbles do not remain attached to it and bounce away from the physical wall.

Hence we have implemented the following boundary conditions, of the Dirichlet type, in the code for what concerns the variable *VOF*, which corresponds to a flag assuming value 1 in the cells where is momentarily present the second phase, and value 0 where the main phase is present. Again we used two concatenated iteration loops along x and y coordinates:

- **Lower wall**

$$\cdot\, VOF(i,j,0) = -VOF(i,j,1) \tag{A.12}$$

- **Upper wall**

$$\cdot\, VOF(i,j,kl) = -VOF(i,j,kmax) \tag{A.13}$$

- **Periodical conditions along y direction**

$$\cdot\, VOF(i,0,k) = VOF(i, jmax, k) \tag{A.14}$$

- **Periodical conditions along x direction**

$$\cdot\, VOF(0,j,k) = VOF(imax, j, k) \tag{A.15}$$

In the following collection of picture we can see that the bubbles do not adhere to the upper and lower walls.

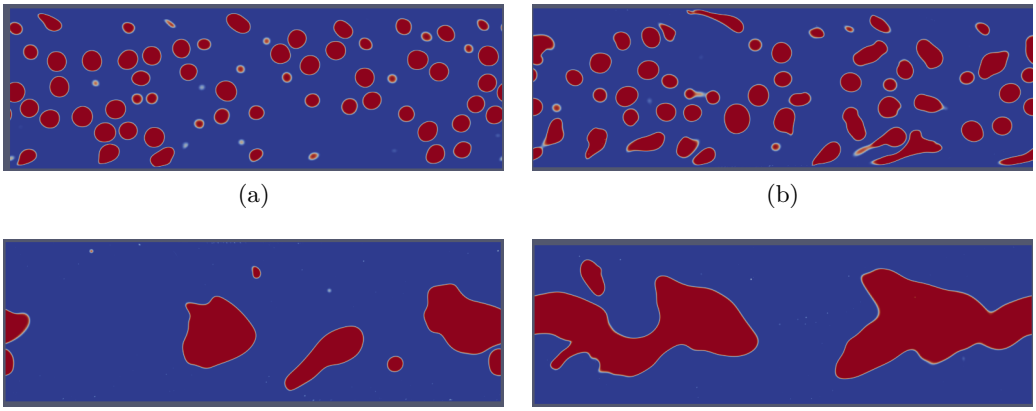

(a) (b)

(c) (d)

Figure A.3: Visualization of the flow with $Re = 2800$ and $Phi = 20\%$. From the top left going clockwise we have $t = 0$, $t = \frac{1}{3}t_{end}$, $t = \frac{2}{3}t_{end}$ and $t = t_{end}$. You can notice how the bubbles merge one to another while not adhering to the walls.

Note that despite the high value assumed by the Weber number the bubbles merge together and do not break up in smaller ones.

Appendix B

Heat advection equation

We consider the generic transport equation for a scalar quantity:

$$\frac{\partial A}{\partial t} + \mathbf{V} \cdot \nabla A - \nabla \cdot (\Gamma \nabla A) - q_A = 0 \tag{B.1}$$

where the first term accounts for the local variation of the scalar quantity A, which is caused by the transport due to the mean bulk flow (second term), by the diffusion (third term) and eventually by the production/dissipation component q_A.

In this case of study the contribute of the sources/sinks q_A is neglected. Moreover the diffusivity is considered constant. Under these specifications the equation B.1 yields in:

$$\frac{\partial A}{\partial t} + \mathbf{V} \cdot \nabla A - \Gamma \nabla^2 A = 0 \tag{B.2}$$

Now equation B.2 must be discretized across the computational domain in order to implement a numerical method for a solution.

We have implemented a 1^{st} order forward scheme for the advection term, 2^{nd} order centred scheme for the diffusion term. The advancement in time is provided by a two-steps Adam-Bashforth method. This class of numerical methods consider the current time-step and a number of past time-steps in order to evaluate the future time-step.

Hence the discretized formula will be composed of three parts: the variation of the scalar quantity in time, the variation due to the mean flow motion, that is to say the advection term, and the variation due to viscous transport, that is to say the diffusion.

In order to obtain a more stable scheme we have averaged the value of the advective term $\mathbf{V} \cdot \nabla A$ at the cell centre between the two values of the adjacent cells in the respective direction x, y, z. For the sake of clarity consider the direction x: the value of the advective term in the cell center $u^k(x_n, y_n, z_n) \left(\frac{\partial A}{\partial t}\right) |^k_{(x_n, y_n, z_n)}$ at the k^{th} time-step is given by the mean between the same term evaluated at the cell interface $x_{n-\frac{1}{2}}, y_n, z_n$ and the same term evaluated at the cell interface $x_{n+\frac{1}{2}}, y_n, z_n$, which in their turn are obtained through a 1^{st} order forward scheme between the cell $n+1$ and n and between cells n and $n-1$.

Hence we have implemented an *Essentially Non Oscillatory* method (ENO) for the first derivative present in the advective term, with Fromm limiter. ENO schemes represent a family of numerical methods in which the slope, hence the first derivative of the scalar

Number of step	**Numerical scheme**	**Note**
1	$y_{n+1} = y_n + hf(t_n, y_n)$	Euler method
2	$y_{n+2} = y_{n+1} + h\left(\frac{3}{2}f(t_{n+1}, y_{n+1}) - \frac{1}{2}f(t_n, y_n)\right)$	used in CODE-VOF
3	$y_{n+3} = y_{n+2} + h\left(\frac{23}{12}f(t_{n+2}, y_{n+2}) - \frac{16}{12}f(t_{n+1}, y_{n+1}) + \frac{5}{12}f(t_n, y_n)\right)$	-
4	$y_{n+4} = y_{n+3} + h\Big(\frac{55}{24}f(t_{n+3}, y_{n+3}) - \frac{59}{24}f(t_{n+2}, y_{n+2}) + \frac{37}{24}f(t_{n+1}, y_{n+1}) + - \frac{9}{24}f(t_n, y_n)\Big)$	-
5	$y_{n+5} = y_{n+4} + h\Big(\frac{1901}{720}f(t_{n+4}, y_{n+4}) - \frac{2774}{720}f(t_{n+3}, y_{n+3}) + + \frac{2616}{720}f(t_{n+2}, y_{n+2}) - \frac{1724}{720}f(t_{n+1}, y_{n+1}) + \frac{251}{720}f(t_n, y_n)\Big)$	-

Table B.1: Adam-Bashforth schemes with steps from 1 to 5.

Local variation of A	$\frac{A^{k+1} - A^k}{\Delta t}$	local variation of the scalar quantity in a defined point between the time-steps $k+1$ and k
Diffusion term	$\Delta t\Gamma\Big[\frac{A^k(x_{n+1},y_n,z_n)-2A^k(x_n,y_n,z_n)+A^k(x_{n-1},y_n,z_n)}{\Delta x^2} +$ $\frac{A^k(x_n,y_{n+1},z_n)-2A^k(x_n,y_n,z_n)+A^k(x_n,y_{n-1},z_n)}{\Delta x^2} +$ $\frac{A^k(x_n,y_n,z_{n+1})-2A^k(x_n,y_n,z_n)+A^k(x_n,y_n,z_{n-1})}{\Delta x^2}\Big]$	diffusion term discretized along the three direction x, y and z with 2^{nd} order centred scheme
Advection term	$-\frac{1}{2}\Delta t\Big[u^k(x_{n+\frac{1}{2}},y_n,z_n)\frac{A^k(x_{n+1},y_n,z_n)-A^k(x_n,y_n,z_n)}{\Delta x} +$ $u^k(x_{n-\frac{1}{2}},y_n,z_n)\frac{A^k(x_n,y_n,z_n)-A^k(x_{n-1},y_n,z_n)}{\Delta x}\Big] -$ $\frac{1}{2}\Delta t\Big[v^k(x_{n+\frac{1}{2}},y_n,z_n)\frac{A^k(x_{n+1},y_n,z_n)-A^k(x_n,y_n,z_n)}{\Delta x} +$ $v^k(x_{n-\frac{1}{2}},y_n,z_n)\frac{A^k(x_n,y_n,z_n)-A^k(x_{n-1},y_n,z_n)}{\Delta x}\Big] -$ $\frac{1}{2}\Delta t\Big[w^k(x_{n+\frac{1}{2}},y_n,z_n)\frac{A^k(x_{n+1},y_n,z_n)-A^k(x_n,y_n,z_n)}{\Delta x} +$ $w^k(x_{n-\frac{1}{2}},y_n,z_n)\frac{A^k(x_n,y_n,z_n)-A^k(x_{n-1},y_n,z_n)}{\Delta x}\Big]$	advection term discretized with 1^{st} order forward scheme along the three directions x, y, z and averaged between the two correspondent faces of the cell

Table B.2: Terms in the Adam-Bashforth method used for discretizing the heat transfer equation.

physical quantities, is chosen taking into account the slopes of the adjacent cells. The criteria for choosing the slopes, or the combination of slopes, is the limiter Λ, which receives as an input the ratio between right and left slope and produces as an output the

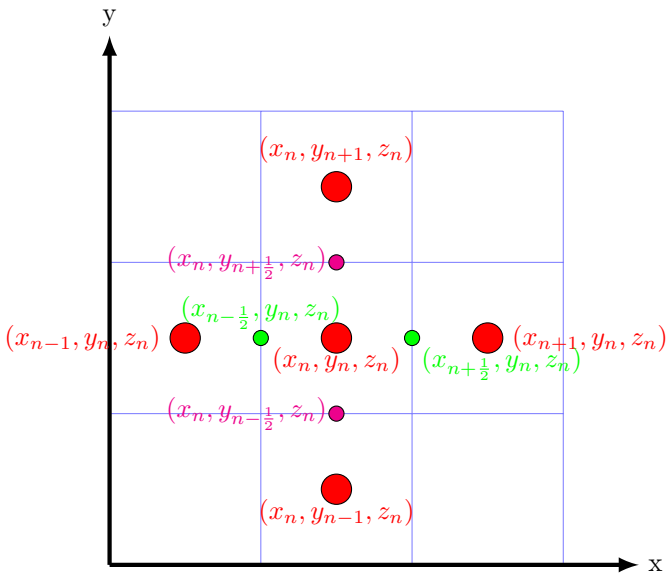

Figure B.1: Numerical grid

slope for the considered cell.

$$\theta_n = \frac{\sigma_n^R}{\sigma_n^L} \tag{B.3}$$

$$\sigma_n = \Lambda(\theta_n)\sigma_n^L \tag{B.4}$$

In the Fromm scheme the slope in the n^{th} cell is computed as an average between the slopes of the right, or forward, cell σ_n^L and the left, or backward, cell σ_n^L. Hence we obtain:

$$\Lambda(\theta_n) = \frac{1+\theta_n}{2} \tag{B.5}$$

$$\sigma_n = \Lambda(\theta_n)\sigma_n^L = \frac{\sigma_n^R + \sigma_n^L}{2} \tag{B.6}$$

The term enlightened in second and third rows in table B.2 are evaluated at time-step k and k+1 and the resulting quantities are used as a term for the Adam-Bashforth iteration (see the second row of table B.1), thus obtaining the final iteration algorithm:

$$A_{new} = A_{old} + \frac{3}{2}\Delta t \left(A_{diff}^k + A_{conv}^k\right) - \frac{1}{2}\Delta t \left(A_{diff}^{k-1} + A_{conv}^{k-1}\right) \tag{B.7}$$

The equation B.7 has been added to the main code to evaluate the transport of energy due to both diffusive and advective effects, along with the transport of mass, of both phases, and momentum.

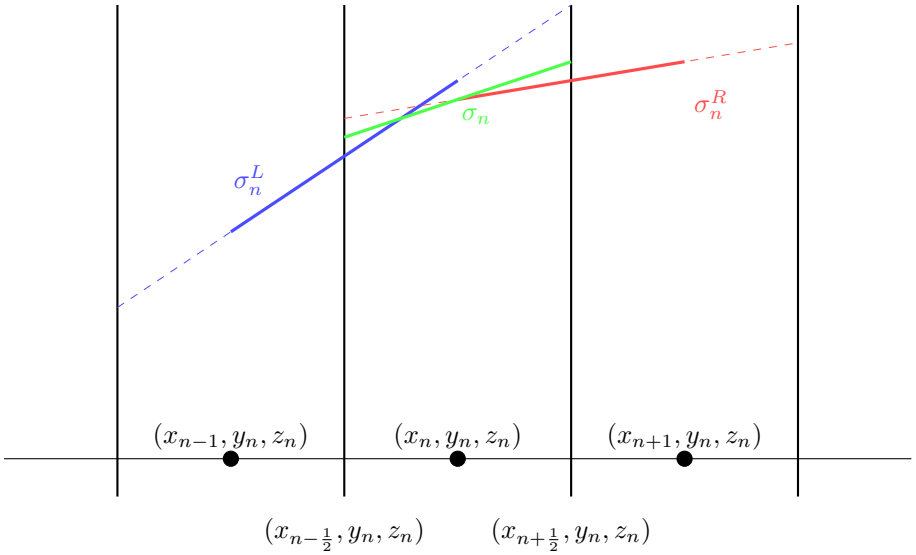

Figure B.2: Averaging of the first derivative in the advection term.

Appendix C

Heat advection code validation

We carried on several code validation tests in order to test the accuracy of the code in accounting for the energy transfer across the computational domain. The validation cases have been carried out using a smaller domain and a more coarse numerical grid for the sake of simplicity, only in 2D, in the plane $y - z$.

The parameters implemented in the validation test cases are the following:

- $Re = 400$
- $\mu = \frac{1}{400}$
- $\rho = 1.0$
- $V_{bulk} = 1.0$
- $l_y = 2.0,\ j = 40$
- $l_z = 2.0,\ k = 40$
- $\kappa = 1.0$
- $c_p = 1.0$
- $\alpha = \frac{k}{\rho c_p} = 1.0$

The largest difficulty to be overcome has been the implementation of the boundary conditions for the heat scalar. We have taken into consideration many cases.

C.1 Constant boundary conditions

In this case a constant value of the scalar temperature has been imposed on both walls. The value of the scalar is intended to be constant along the y coordinate.

- **Lower wall**

$$\cdot\, A(i,j,0) = 2.0 * 20.0 - A(i,j,1) \tag{C.1}$$

- **Upper wall**

$$\cdot A(i,j,kl) = 2.0 * 1.0 - A(i,j,kmax) \tag{C.2}$$

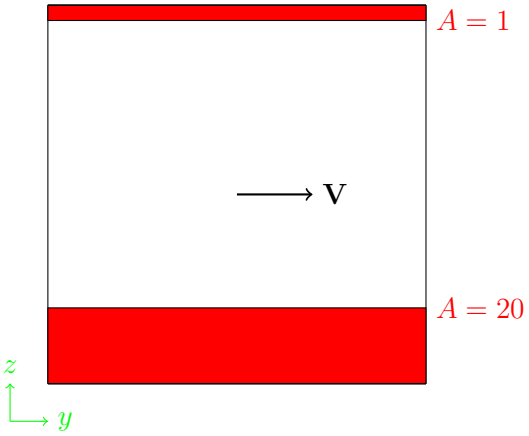

Figure C.1: Code validation with constant boundary conditions.

The presence of A across the height of the channel assumes a linear gradient across the height of the channel. This is due to the fact that there is no gradient of A along the direction of the velocity $\mathbf{V}$, that is to say along y. In fact the two value imposed on the walls are constant along y direction. Thus in steady-state regime the term of advection is suppressed in B.1 and only the term of diffusion remains:

$$\frac{\partial A}{\partial t} + \cancel{\mathbf{V} \cdot \nabla A} - \nabla \cdot (\Gamma \nabla A) = 0 \tag{C.3}$$

Hence the diffusion equations yields in the diffusion equation, with constant diffusivity Γ:

$$\frac{\partial A}{\partial t} = \Gamma \nabla^2 A \tag{C.4}$$

In steady-state regime there are no variation of the distribution of A in time, hence it results:

$$\Gamma \nabla^2 A = 0 \tag{C.5}$$

The solution to the diffusion equation can be found via integration in with respect to the spatial coordinate y:

$$\int_{y_0}^{y_{max}} \frac{\partial^2 A}{\partial y^2} dy = \int_{y_0}^{y_{max}} dy \Longrightarrow \int_{y_0}^{y_{max}} \frac{\partial A}{\partial y} dy = \int_{y_0}^{y_{max}} k dy \Longrightarrow \int_{y_0}^{y_{max}} \frac{\partial A}{\partial y} dy = ky + C \tag{C.6}$$

being k, C constants whose value depends upon boundary conditions.
The code implemented gives as an outcome the following results:

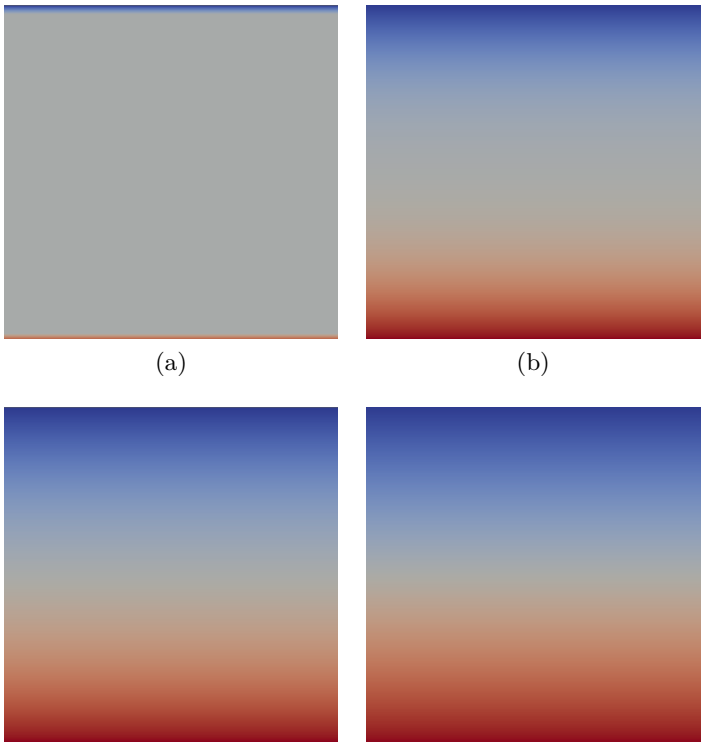

(a) (b)

(c) (d)

Figure C.2: Visualization of the transport of the scalar A with $Re = 400$ with constant B.C.. From the top left going clockwise we have $t = 0$, $t = \frac{1}{4}t_{end}$, $t = \frac{1}{2}t_{end}$ and $t = t_{end}$.

C.2 Sinusoidal boundary conditions

In this case a sinusoidal value of the scalar temperature has been imposed on both walls, with different mean values between upper and lower walls but with the same frequency and the same amplitude of oscillation.

- **Lower wall**

$$\cdot A(i,j,0) = 2.0 * \left(20.0 + 4.0 * \sin\left(\pi * \frac{j}{j_{tot}}\right)\right) - A(i,j,1) \tag{C.7}$$

- **Upper wall**

$$\cdot A(i,j,kl) = 2.0 * \left(10.0 + 4.0 * \sin\left(\pi * \frac{j}{j_{tot}}\right)\right) - A(i,j,kmax) \tag{C.8}$$

The code implemented gives as an outcome the following results:

Also in this case we observe a linear gradient of the scalar temperature A across the height of the channel. This is due to the fact that the two sinus waves on the upper and

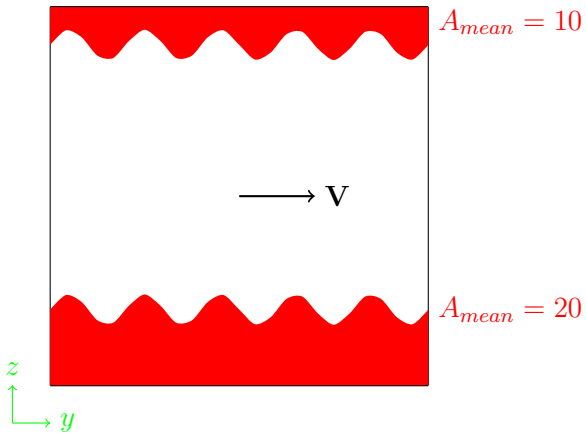

Figure C.3: Code validation with sinusoidal boundary conditions.

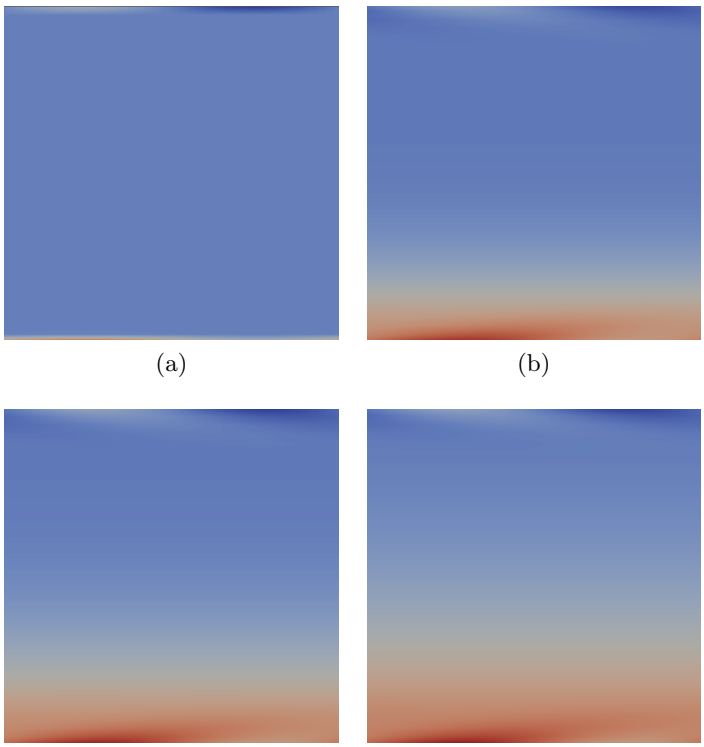

Figure C.4: Visualization of the transport of the scalar A with $Re = 400$ with sinusoidal B.C.. From the top left going clockwise we have $t = 0$, $t = \frac{1}{4}t_{end}$, $t = \frac{1}{2}t_{end}$ and $t = t_{end}$.

lower walls have the same period and the same starting value, hence there are no gradients of A along the y direction and the advection terms is suppressed again. One possible way

for accounting for the presence of this gradient is to impose a sinusoidal value for A on a wall and a constant value for A on the opposite one in the boundary conditions.

C.3 Constant and sinusoidal boundary conditions

In this case a sinusoidal value of the scalar temperature has been imposed on the lower wall, while a constant value of A has been imposed on the upper wall. This was done with the purpose of creating a gradient $\frac{\partial A}{\partial y}$ and hence take into account the effect of advection due to mean bulk flow.

- **Lower wall**

$$\cdot\, A(i,j,0) = 2.0 * \left(20.0 + 4.0 * \sin\left(\pi * \frac{j}{j_{tot}}\right)\right) - A(i,j,1) \tag{C.9}$$

- **Upper wall**

$$\cdot\, A(i,j,kl) = 2.0 * 1.0 - A(i,j,kmax) \tag{C.10}$$

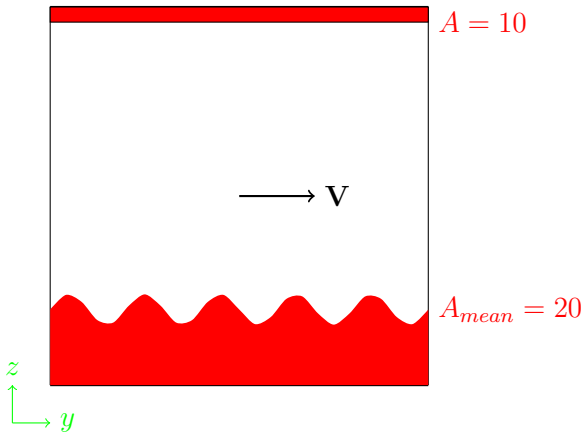

Figure C.5: Code validation with both constant and sinusoidal boundary conditions.

In this case the profile of distribution of A across the height of the channel is no longer linear given the fact that is present a gradient $\frac{\partial A}{\partial y}$ hence the component $\mathbf{V} \cdot \nabla A$ is no longer null since the scalar product gives a result different from 0 because the gradient and the velocity are no longer perpendicular.

In figures C.6c and C.6d in particular, we can observe how the scalar temperature, going from value *10* in areas highlighted in blue to value *24* in the areas highlighted in red, presents a smear in the area at the bottom right. This smear becomes ore evident as the time passes, and its presence is due to the bulk flow motion.

Manifestly this phenomena was not appreciable in the cases with constant boundary conditions since the effects of advection were not present.

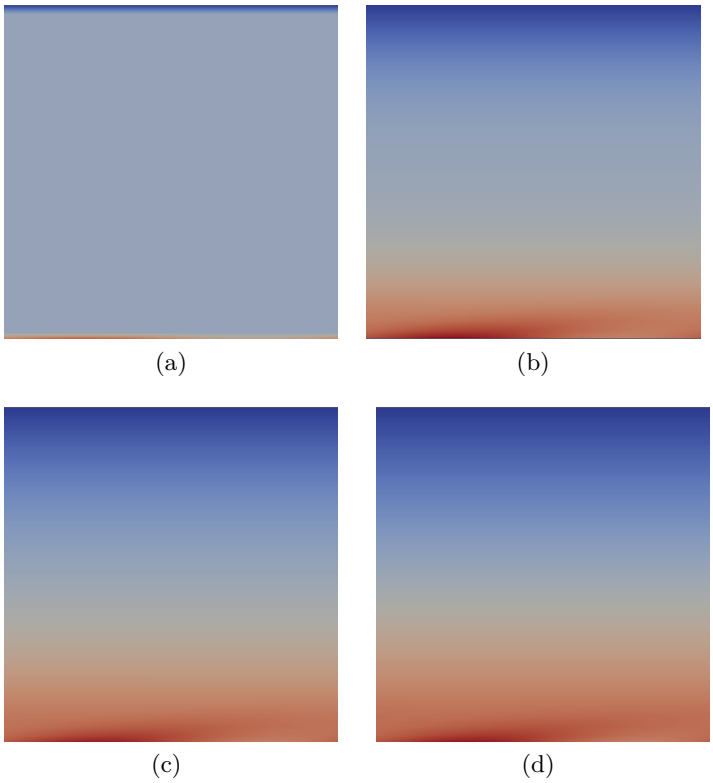

(a) (b)

(c) (d)

Figure C.6: Visualization of the transport of the scalar A with $Re = 400$ with sinusoidal and constant B.C.. From the top left going clockwise we have $t = 0$, $t = \frac{1}{4}t_{end}$, $t = \frac{1}{2}t_{end}$ and $t = t_{end}$.

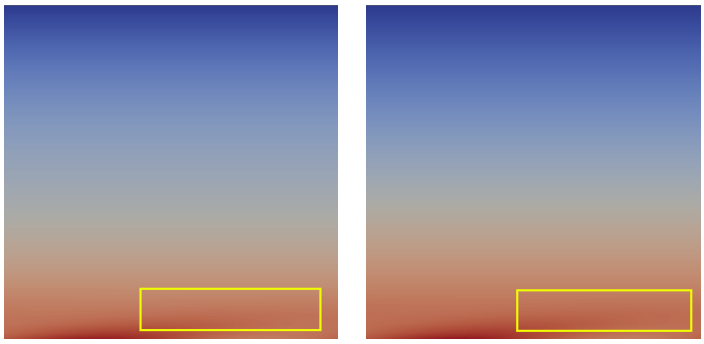

(a) (b)

Figure C.7: Visualization of a recirculation smear in the case with $Re = 400$ with sinusoidal and constant B.C., at $t = \frac{1}{2}t_{end}$ and $t = t_{end}$.

Bibliography

Bibliography

[BKZ92] Jeremiah U. Brackbill, Douglas B. Kothe, and Charles Zemach. "A continuum method for modeling surface tension". In: *Journal of computational physics* 100.2 (1992), pp. 335–354.

[CB05] SI Chernyshenko and MF Baig. "Streaks and vortices in near-wall turbulence". In: *Philosophical Transactions of the Royal Society A: Mathematical, Physical and Engineering Sciences* 363.1830 (2005), pp. 1097–1107.

[Chr05] E. Brennen Christopher. "Fundamentals of multiphase flows". In: *Cambridge University, Press UK* (2005).

[Cro93] C.T. Crowe. "Modeling turbulence in multiphase flows". In: *Engineering turbulence modelling and experiments*. Elsevier, 1993, pp. 899–913.

[ET93] S. Elghobashi and G.C. Truesdell. "On the two-way interaction between homogeneous turbulence and dispersed solid particles. I: Turbulence modification". In: *Physics of Fluids A: Fluid Dynamics* 5.7 (1993), pp. 1790–1801.

[EB69] Inc Encyclopaedia Britannica. *Encyclopædia britannica*. Encyclopaedia Britannica, Incorporated, 1969.

[Geo+18] Christopher J Geoga et al. "Frequency–wavenumber spectral analysis of spatio-temporal flows". In: *Journal of Fluid Mechanics* 848 (2018), pp. 545–559.

[GC89] R.A. Gore and Clayton T. Crowe. "Effect of particle size on modulating turbulent intensity". In: *International Journal of Multiphase Flow* 15.2 (1989), pp. 279–285.

[HS71] Gad Hetsroni and Mordechai Sokolov. "Distribution of mass, velocity, and intensity of turbulence in a two-phase turbulent jet". In: *Journal of Applied Mechanics* 38.2 (1971), pp. 315–327.

[Ii+12] Satoshi Ii et al. "An interface capturing method with a continuous function: The THINC method with multi-dimensional reconstruction". In: *Journal of Computational Physics* 231.5 (2012), pp. 2328–2358.

[JA95] D. John and J.R. Anderson. *Computational fluid dynamics: the basics with applications*. Mechanical Engineering Series. McGraw-HILL, 1995.

[KM85] J. Kim and P. Moin. "Application of a fractional-step method to incompressible Navier-Stokes equations". In: *Journal of Computational Physics* (1985), p. 16.

[Kul93] J.D. Kulick. "Turbulence modification by dispersed particles in fully-developed channel flow". In: *Proc. 9th Turbulent Shear Flow, 1993* 2 (1993).

[Las+16] Iman Lashgari et al. "Channel flow of rigid sphere suspensions: particle dynamics in the inertial regime". In: *International Journal of Multiphase Flow* 78 (2016), pp. 12–24.

[Las+14] Iman Lashgari et al. "Laminar, turbulent, and inertial shear-thickening regimes in channel flow of neutrally buoyant particle suspensions". In: *Physical review letters* 113.25 (2014), p. 254502.

[LF88] John H Lee and David L Frostf. "Steam explosions: major problems and current status". In: *Dynamics of explosions* (1988), p. 436.

[LPZ13] Harvard Lomax, Thomas H. Pulliam, and David W. Zingg. *Fundamentals of computational fluid dynamics*. Springer Science & Business Media, 2013.

[Pic+13] Francesco Picano et al. "Shear thickening in non-Brownian suspensions: an excluded volume effect". In: *Physical review letters* 111.9 (2013), p. 098302.

[Pop01] Stephen B. Pope. *Turbulent flows*. 2001.

[RHB90] Mr Rashidi, G. Hetsroni, and Sanjoy Banerjee. "Particle-turbulence interaction in a boundary layer". In: *International Journal of Multiphase Flow* 16.6 (1990), pp. 935–949.

[Rey95] Osborne Reynolds. "On the dynamical theory of incompressible viscous fluid and the determination of the criterion, Phys". In: *Trans of the Royal Soc* (1995).

[RB18] Marco E. Rosti and Luca Brandt. "Suspensions of deformable particles in a Couette flow". In: *Journal of Non-Newtonian Fluid Mechanics* 262 (2018), pp. 3–11.

[RDVB19] Marco E. Rosti, Francesco De Vita, and Luca Brandt. "Numerical simulations of emulsions in shear flows". In: *Acta Mechanica* (2019), pp. 1–16.

[Ros+19] Marco E. Rosti et al. "Droplets in homogeneous shear turbulence". In: *Journal of Fluid Mechanics* (2019).

[Ros+18] Marco Edoardo Rosti et al. "Emulsions in homogeneous shear turbulence". In: *Proceedings of the Summer Program 2018* (2018), p. 10.

[SS03] James A. Sethian and Peter Smereka. "Level set methods for fluid interfaces". In: *Annual review of fluid mechanics* 35.1 (2003), pp. 341–372.

[Sus+07] M. Sussman et al. "Direct numerical simulation of free-surface and interfacial flow". In: *J. Comp. Physics* 221 (2007), pp. 469–505.

[SSO94] Mark Sussman, Peter Smereka, and Stanley Osher. "A level set approach for computing solutions to incompressible two-phase flow". In: *Journal of Computational physics* 114.1 (1994), pp. 146–159.

[TSH07] G. Tryggvason, M. Sussman, and M.Y. Hussaini. "Immersed boundary methods for fluid interfaces". In: *Computational methods for multiphase flow* 3 (2007).

[Try+01] Grétar Tryggvason et al. "A front-tracking method for the computations of multiphase flow". In: *Journal of computational physics* 169.2 (2001), pp. 708–759.

[TM82] Yutaka Tsuji and Yoshinobu Morikawa. "LDV measurements of an air—solid two-phase flow in a horizontal pipe". In: *Journal of Fluid Mechanics* 120 (1982), pp. 385–409.

[TMS84] Yutaka Tsuji, Yoshinobu Morikawa, and Hiroshi Shiomi. "LDV measurements of an air-solid two-phase flow in a vertical pipe". In: *Journal of Fluid Mechanics* 139 (1984), pp. 417–434.

[UT92] Salih Ozen Unverdi and Grétar Tryggvason. "A front-tracking method for viscous, incompressible, multi-fluid flows". In: *Journal of computational physics* 100.1 (1992), pp. 25–37.

[YC91] E. Yokuda and C.T. Crowe. "Effect of Reynolds number and spacing on the dispersion of particles in self-induced turbulence". In: *Turbulence Modification in Multiphase Flows* 110 (1991), pp. 7–13.

[Zal78] Steven T. Zalesak. *Fully Multidimensional Flux-Corrected Transport.* Tech. rep. NAVAL RESEARCH LAB WASHINGTON DC, 1978.

[Zha17] Yongming Zhang. "Critical transition Reynolds number for plane channel flow". In: *Applied Mathematics and Mechanics* 38.10 (2017), pp. 1415–1424.

Sitography

[Enc] *Encyclopædia Britannica: Fluid definition.*

[Pip] *Pipe Flow Experiments.*

[Sin] *Single-phase flows visualization.*

[Sta] *Stanford University multi-phase flows visualization.*

Design Information

This document was typeset in LaTeX using the typographical look-and-feel `toptesi`*. Most of the graphics in this thesis are generated using* `pgfplots` *and* `tikz`*. The bibliography is typeset using* `biblatex`*.*